Signal Processing and Renewable Energy
September 2024, (pp. 1-20)
ISSN: 2588-7327
eISSN: 2588-7335

A New Non-isolated Buck-Boost DC/DC Converter Based on Cuk Topology with Single Switch for Renewable Energy Application

Mustafa Okati [1*], Mohammad Osmani-Bojd [2], Samira Samimi [3]

[1] Department of Electrical Engineering, Zabol Branch, Islamic Azad University, Zabol, Iran.
[2] Department of Electrical Engineering, Zahedan Branch, Islamic Azad University, Zahedan, Iran.
[3] Department of Mathematics Education, Farhangian University, Zahedan, Iran.

Received: 08-Apr-2024, Revised: 18-Aug-2024, Accepted: 20-Aug-2024.

Abstract

The present investigation aims to design an active switch non-isolated buck-boost DC/DC converter based on the CUK topology. In this converter, a simpler circuit topology is used to reach higher voltage gains at lower duty cycle levels. Furthermore, the mentioned converter presents a continuous input/output current with negative output polarity. Compared to the conventional method of obtaining a broader range of the voltage conversion ratio characterized by the same duty cycle, the suggested converter explains the fundamentals and prominent waveforms of the Continuous Conduction Mode (CCM). Also, the efficiency was analyzed through the substitution of the parasitic resistance effects for the steady-state circumstances. The power loss calculation, parameter design, and characteristics are completely investigated in the suggested converter, and a comparative analysis with other non-isolated converters is carried out. Eventually, by creating a working hardware prototype characterized by a 48-watt power output, the practicality of the suggested converter is confirmed by the empirical data gathered from testing.

Keywords: Cuk Converter, Buck-Boost Converter, Switching Device Power, Continuous Input/output Current, Single Switch.

1. INTRODUCTION

Numerous investigations have been conducted globally to investigate sustainable energy alternatives in response to the progressively diminishing availability of natural resources and their detrimental impact on the environment. Photovoltaic (PV) and wind power generation, among

*Corresponding Authors Email: Mu.okati@gmail.com

other renewable energy sources, have garnered considerable attention in recent years. Renewable energy sources have emerged as a highly desirable option owing to their favorable environmental and economic characteristics. Nevertheless, several challenges, including low output voltage, persist with their utilization. Distributed generation systems refer to localized, small-scale power generation systems that utilize renewable sources of energy to meet the growing electricity demand and also address environmental concerns. There are various sustainable energy technologies, including fuel cells and solar photovoltaic (PV) systems. Several renewable energy sources can be integrated within a Direct Current (DC)

microgrid, as illustrated in Fig.1. A direct current (DC) microgrid presents itself as the most feasible resolution for the assimilation of photovoltaic (PV) generation systems in combination with DC loads and alternating current (AC) power grid. The utilization of Solar Photovoltaic (PV) systems holds a significant position amongst alternative energy sources for Direct Current (DC) distributed generation systems [1], [2]. The microgrid system can operate in both grid-connected mode and islanding mode with a primary focus on maintaining system consistency and sustainability, as outlined in the source [3]. Highly significant DC-DC converters with high voltage gain are fundamental in the upward regulation and mitigation of low and variable DC voltages, ranging from 12 V to 128 V, which are derived from solar photovoltaic systems within DC microgrid contexts. The aforementioned DC microgrid systems have bus bar voltages of up to 400 V DC, as stated by various sources [4]-[7]. High voltage gain direct current/direct current (DC/DC) converters are primarily designed to offer a substantial conversion ratio and superior efficiency while occupying minimal physical space [8].

Numerous high step-up DC-DC converter topologies have been put forth in the existing literature to attain a substantial voltage gain with a reasonable duty ratio while ensuring high converter efficiency and minimal voltage stress across components [9]. By utilizing the traditional boost DC-DC converter, it is possible to attain a substantial increase in voltage. Nevertheless, the voltage stress applied to the switch corresponds to the output voltage, and the amplification in voltage is restricted by the stress in voltage/current that passes through the switch when operating at high-duty cycle levels. As per the literature [10], [32], opting for a switch with a high rating to fulfill the voltage

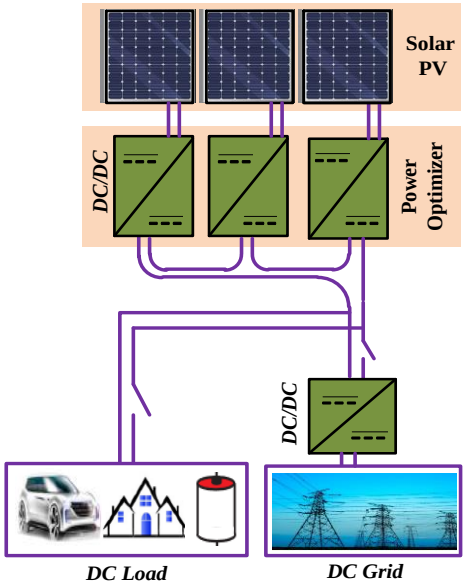

Fig.1. Structure of DC/DC converter application.

stress requirement eventually results in elevated conduction loss. To accomplish substantial voltage amplification, various converter structures, including the half/full-bridge, flyback, push/pull, and forward converters, have been proposed in the literature. Such improvement is achieved by modifying the turn ratio of the transformer or coupled inductor, as described in previous works [11]-[14]. Notwithstanding the advantages offered by converter structures, there exist certain limitations that must be acknowledged. These drawbacks include circuitry of significant size, high voltage spikes in switch operations, power dissipation, the risk of transformer core saturation, and an increased level of voltage stress for converter active switches due to the transformer leakage inductance. Moreover, the inclusion of a high-frequency transformer, non-dissipative snubber circuit, and supplementary active clamping circuit serve to amplify the monetary and dimensional expenditures of these converters [15], [16].

In situations where galvanic insulation is not deemed necessary, non-isolated DC-DC converters have been employed as a means of achieving a considerable voltage gain, thereby resulting in decreased overall dimensions, weight, and volume due to the absence of a high-frequency transformer, and consequently leading to an enhanced level of efficiency. The discussion of diverse non-isolated converter topologies in the extant literature can be classified into two categories: those equipped with broad conversion range converters and those without, as outlined in previous studies [17], in the quadratic converters, the switch voltage stress level is congruent with that of the output voltage, as established by prior studies [18]. Conversely, in the cascade boost converter, despite the possibility of amalgamating the two switches for the sake of diminishing circuit complexity, the switch remains subjected to formidable voltage and current stresses [19]. The main drawback of converter designs using switched capacitor cells and voltage lift cells is the increased stress on power switches and diode currents caused by the presence of capacitor networks. This can lead to decreased efficiency. However, incorporating the interleaved converter method along with fewer control switches and a smaller filter size can enhance efficiency and performance [20]. Nonetheless, the integration of multiple converters in a parallel configuration result in a significant surge in intricacy and the accompanying drive circuitry. Additionally, this methodology is characterized by a series of adverse implications that comprise intricate switching control reasoning, elevated voltage/current tension, and substantial energy dissipation [21]. Additionally, a new quadratic converter was unveiled [22]. To address the issue of power discontinuities in both the input and output, this converter was equipped with inductive filters at both the input and output. In addition, there were a number of components with the input and output polarities reversed. Additionally, ZETA DC-DC converters are available; they were recently proposed in [23]. Only twice as much voltage gain is present in the ZETA converter proposed here as there is in the traditional ZETA converter. Certain research suggested the use of a quadratic buck-boost converter, which

requires two gate drivers for each power switch. As a result, the converter's size and control system complexity have grown [24]. In [25], a quadratic DC/DC converter with positive output polarity was developed and examined. The converter's voltage gain ratio is modest, though, because continuous current flows through both the input and output terminals. The converter in [26] proposes a quadratic buck–boost converter with negative output. Since inductive filters are installed in the output and input ports, the structure's output and input currents are continuous. In addition to having a discontinuous input current, a lower voltage gain ratio, and less voltage stress on the components, a novel quadratic buck-boost converter was presented [27]. A mathematical analysis of various topologies has been conducted to thoroughly understand the dynamic behavior of the converter [28]. The voltage gain in the ZETA converter is twice the voltage gain provided by the typical ZETA converters. Here is a transformerless DC/DC converter design featuring dual operation modes buck/boost. The system functions as a common ground with a continuous input current between the output and input terminals due to its simple and common configuration [29]. Renewable energy (RE) systems require stable voltage and current for effective energy management. The quadratic output voltage gain of this converter allows it to handle a wider range of input voltages while ensuring optimal performance. Also, continuous input and output current ports make it particularly suitable for fluctuating power sources such as solar panels and wind turbines [30].

In addition, cascaded boost converters [31] featuring quadratic voltage gain specifications are suggested in which the voltage stress is decreased on passive devices, and the count of components is minimized. Nonetheless, compared to other models, in one such model, the voltage gain remains lower. In addition, separate control grounds are demanded by both models for the purpose of semiconductor switches that demand two control power supplies.

The present study proposes a new converter topology aimed at achieving a considerable voltage gain while reducing the current stress applied to the active switch; thereby continuous input/output current port with negative polarity is presented. The suggested configuration offers several benefits including a substantial amplification of voltage, minimal strain on the current, reduced conduction loss in the active switch, and enhanced efficiency.

The paper is structured in the following. In Section 2, the suggested converter is presented first, and then theoretical analysis and steady-state assessment are carried out. In Section 3, the benefits of the suggested converter are contrasted with those of similar converters. Section 4 discusses the results of the PLECS simulation and the experimental findings of the suggested converter's laboratory-made prototype. Lastly, Section 5 presents the key conclusions.

2. PROPOSED TOPOLOGY

The schematic diagram of the power circuit for the suggested converter is presented in Fig.2. The circuit comprises three inductors, L_1, L_2 and L_3 which possess

identical inductance values. Additionally, one switch S_1 is concurrently activated (ON) and deactivated (OFF). The circuit comprises two diodes (D_1-D_2) and four capacitors (C_1-C_3). The present discussion focuses on elucidating the operative mechanisms and conducting a comprehensive steady-state analysis of the proposed converter in Continuous Conduction Mode (CCM).

Time-domain characteristic waveforms from Fig. 3 provide a vivid representation of several of the charging and discharging stages.

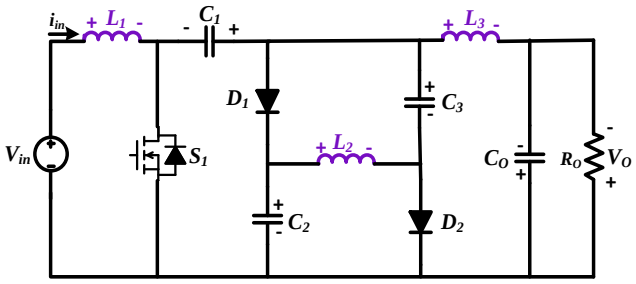

Fig.2. Proposed converter configuration.

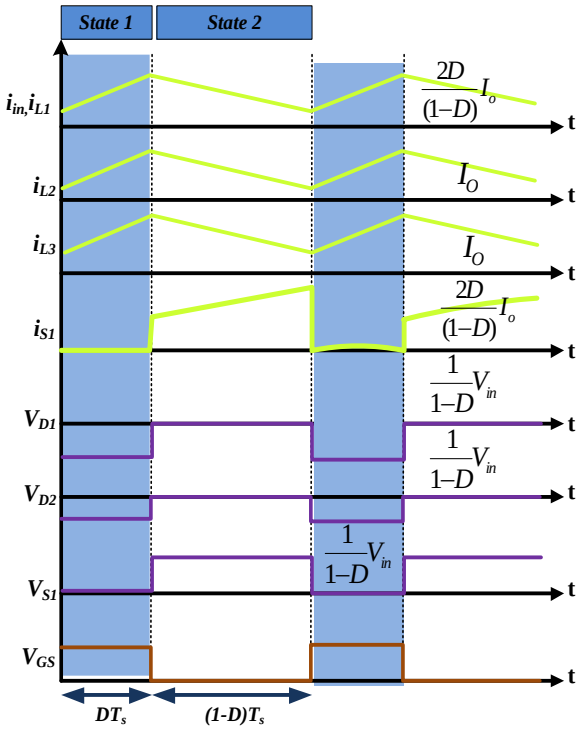

Fig.3. Charging and discharging states key waveforms in the proposed converter's CCM mode

A. Working Principle in CCM

The suggested converter comprises a switch that functions concurrently with duty cycles. Accordingly, the suggested converter functions in two distinct modes while operating in continuous conduction mode functions specifically referred to as a state1 and state 2. According to Fig. 4 and 5, there

are two major operating states assumed for the converter in the CCM.

***State* 1:** During mode, switch S_1 is maintained in the open (ON) position and both diode D_1 and D_2 are off. The schematic representation of the proposed converter for this mode is illustrated in Fig.4. The input voltage supply, denoted as V_{in}, facilitates the charging of inductor L_1 through switch S_1, while the stored energy within capacitor C_o is transferred towards the load R_o. Consequently, it is possible to formulate the voltages across the inductors L_1, L_2, and L_3, in a precise manner, as follows:

$$V_{L1} = V_{in} \quad (1)$$

$$V_{L2} = -V_{C1} + V_{C2} + V_{C3} \quad (2)$$

$$V_{L3} = V_{C1} - V_o \quad (3)$$

***State* 2**: In this mode of operation, it is noted that switch S_1 is switched to the OFF position and the Diodes are ON. The equivalent circuit of the proposed converter is illustrated in Fig.5. The input voltage supply V_{in} denoted as serves to charge several components including the inductors L_1 and capacitors C_1, and C_2 all through using of diode D_1. Simultaneously, capacitor C_3 undergoes charging through diode D_2 via the input supply voltage V_{in}, inductor L_1, capacitor C_1, hence, it is possible to determine the voltages across the inductors L_1, L_2, and L_3 through the utilization of equations (4), (5), and (6).

$$V_{L1} = V_{in} + V_{C1} - V_{C2} \quad (4)$$

$$V_{L2} = V_{C2} \quad (5)$$

$$V_{L3} = V_{C3} - V_o \quad (6)$$

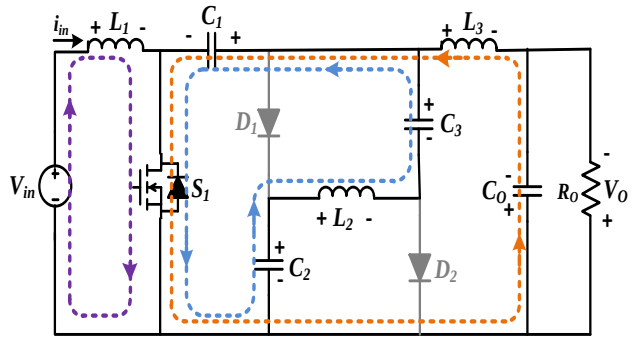

Fig. 4. Operating mode of State 1.

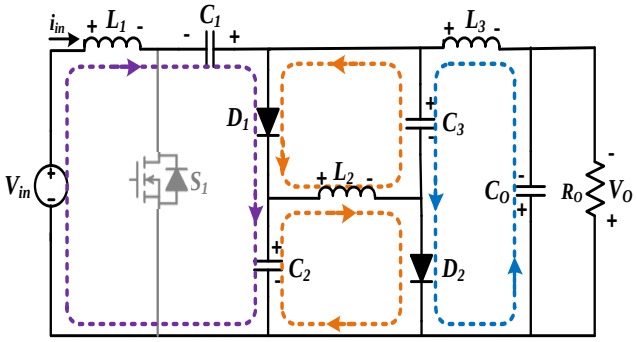

Fig. 5. Operating mode of State 2.

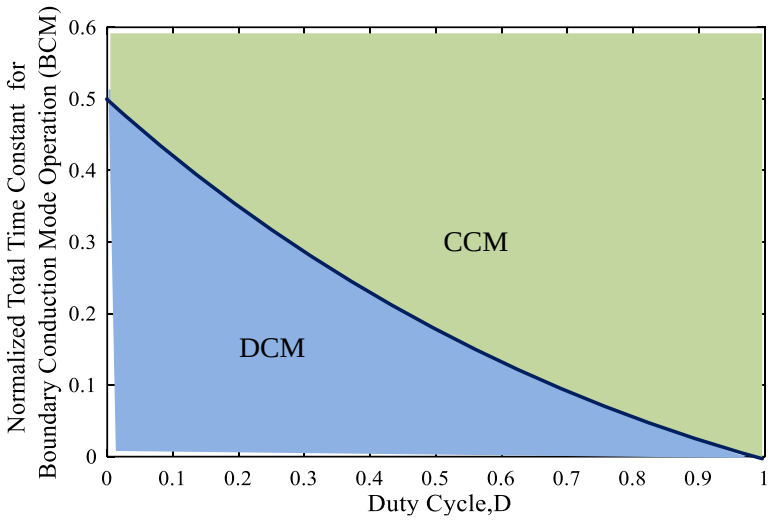

Fig. 6. Boundary condition (CCM and DCM).

The voltages of the capacitors C_3, C_2, and C_1, as well as the output voltage, are determined by using the volt-second balance on the inductors voltage as described in (1)–(6),

$$V_{C2} = V_{C3} = \frac{D}{1-D} V_{in} \tag{7}$$

$$V_{C1} = \frac{1}{D(1-D)} \tag{8}$$

It can be observed that the voltage across the output capacitor Co is equivalent to the output voltage Vo. it can be concluded that,

$$V_o = \frac{2D}{(1-D)} V_{in} \tag{9}$$

The symbol D denotes the duty cycle. The ampere-second balance principle of capacitors C_1, C_2, and C_3 is used to calculate the mean current value of all inductor currents. Therefore, I_{L1}, I_{L2} and I_{L3} currents can be calculated:

$$I_{L1} = \frac{2D}{(1-D)} \tag{10}$$

$$I_{L2} = I_{L3} = I_o \tag{11}$$

The output voltage and current can be obtained as follows,

$$V_o = \frac{2D}{(1-D)} V_{in} \tag{12}$$

$$I_o = \frac{1-D}{2D} I_{in} \tag{13}$$

In this manner, the voltage gain,

$$M_{CCM} = \frac{V_o}{V_{in}} = \frac{2D}{(1-D)} \tag{14}$$

B. Boundary Condition

The normalized time constant for the inductor, denoted as τ_L, can be defined as τ_L= L/ (RTs). Fig. 6 depicts the voltage gain deviation in the discontinuous conduction mode of the suggested converter in response to modifications in the duty cycle. One may obtain boundary conditions through the process of equating the M_{CCM} and M_{DCM}. Hence, the normalized boundary time

constant about the inductor denoted by τ_{LB}, can be derived as

$$\tau_{LB} = \frac{(1-D)^2}{2} \quad (15)$$

According to the findings obtained, it is evident that Fig. 6 illustrates the boundary condition of both Continuous Conduction Mode (CCM) and Discontinuous Conduction Mode (DCM) of the suggested converter with respect to it. Furthermore, it must be noted that in cases where $\tau_{\_L}$ exceeds τ_{LB}, the converter under consideration operates in continuous conduction mode (CCM).

C. Inductors Design

We can find the same amount of electrical energy across both L_1 and L_2 by measuring the voltage produced.

$$V_{L1,2} = L_{1,2}\frac{di_{1,2}}{dt} \quad (16)$$

The inductor size is picked depending on how much electricity needs to be charged, how much it moves up and down, how often it is turned on and off, and how fast it switches. We can find out how much electric current flows through each inductor when the batteries are being charged by doing the following:

$$\Delta i_{L1,2,3} = \frac{DV_{L1,2,3}}{L_{1,2,3}f_s} \quad (17)$$

The ripple currents for two inductors, L_3, L_2 and L_1 are labeled as $\Delta i_{L3}, \Delta i_{L2}$ and Δi_{L1}. So, amount of inductors,

$$L_{2,3} \geq \frac{(1-D)V_o}{4I_o f_s} \quad (18)$$

$$L_1 \geq \frac{(1-D)^2 V_o}{8DI_o f_s} \quad (19)$$

Therefore, three inductor values can be selected based on (18)-(19). Also, $\Delta i_{L3,2,1}$ is 10-30% of the nominal inductor current value.

D. Capacitors Design

Capacitor capacitance is controlled by charging current, voltage across, charging rate, and replacement frequency. Therefore, the capacitor voltage ripple is given by:

$$\Delta V_{C1,2,3} = \frac{Di_{C1,2,3}}{C_{1,2,3}f_s}, \Delta V_{Co} = \frac{Di_{Co}}{C_o f_s} \quad (20)$$

We can find out the right amount of capacitors C_1, C_2, C_3, and we need using equations (20),

$$C_1 \geq \frac{2DV_o}{\Delta V_{C1}R_o f_s} \quad (21)$$

$$C_{2,3} \geq \frac{DV_o}{\Delta V_{C2,3}R_o f_s} \quad (22)$$

$$C_o \geq \frac{(1-D)V_o}{16L_3\Delta V_{C1}R_o f_s^2} \quad (23)$$

E. Voltage and Current Stress on Semiconductor

The voltage and current stresses of the diodes and switch of a converter contribute to its power loss and the final cost of implementation. Therefore, theses stresses must be assessed,

$$V_{S1} = \frac{1}{1-D}V_{in} \quad (24)$$

$$I_{S1} = \frac{2D}{1-D} I_o \tag{25}$$

$$V_{D1,2} = \frac{1}{1-D} V_{in} \tag{26}$$

$$I_{D1,2} = I_o \tag{27}$$

F. Efficiency Analysis

Fig. 7 shows the suggested converter circuit, taking into account the nonidealities of various circuit components. The same placement resistance (ESR) of inductors L_1, L_2, and L_3 are shown separated by an R_{L1}, R_{L2} and R_{L3}. Additionally, $R_{FD1}$and R_{FD2} are internal resistors. The forward voltage drops of diodes D_1 and D_2 are V_{FD1} and V_{FD2} respectively. The forward ON resistances of control switch S_1 are shown by R_{DS1}.

The *RMS* value of the switch current, and the diodes current, inductors current, and capacitors current, of the circuit was first calculated by equations (25), (27), (10), and (11),

$$I_{S1-rms} \approx \frac{2\sqrt{D}}{(1-D)} |I_o| \tag{28}$$

$$I_{D1,2(rms)} \approx \frac{(1+D)^{1/2}}{(1-D)^{1/2}} I_o \tag{29}$$

$$I_{L1-rms} \approx \frac{2D}{(1-D)} |I_o| \tag{30}$$

$$I_{L2,3-rms} \approx |I_o| \tag{31}$$

$$I_{C1-rms} \approx \left(\frac{4D}{1-D}\right)^{\frac{1}{2}} |I_o| \tag{32}$$

$$I_{C2,3-rms} \approx \left(\frac{2D}{1-D}\right)^{\frac{1}{2}} |I_o| \tag{33}$$

The total power loss of the switch (P_{S1}) comprises the sum of switching losses ($P_{S\text{-}L}$) and conducting power dissipation ($P_{R\text{-}DS}$), as well as the conduction resistance R_{DS} of the power switch, which is calculated as:

$$P_{S_1} = P_{R-DS} + P_{S-L} \tag{34}$$

$$\begin{cases} P_{R-DS} = R_{DS} I^2_{S-rms} = R_{DS} \dfrac{D^3}{(1-D)^4} I_o^2 \\ P_{S-L} = f_S C_S V_S^2 = f_S C_S \dfrac{1}{(1-D)^2} V_{in}^2 \end{cases} \tag{35}$$

$$\begin{aligned} P_D &= P_{FD} + P_{FR} \\ &= \sum_{i=1}^{i=2} (R_{FD} I^2_{Di-rms}) \\ &\quad + \sum_{i=1}^{i=2} (V_{FDi} I_{Di}) \end{aligned} \tag{36}$$

To calculate the power losses of inductors and capacitors, it can use their equivalent series resistance (ESR), RL, and RC values:

$$P_L = \sum_{i=1}^{i=3} (P_{Li}) = \sum_{i=1}^{i=3} (R_{Li} I^2_{Li-rms}) \tag{37}$$

$$P_{C-Total} = P_{C1} + P_{C2} + P_{C3} + P_{Co} \tag{38}$$

The total loss of the power converter may be summed up as follows:

$$P_{loss-Total} = P_C + P_L + P_S + P_D \tag{39}$$

Lastly, the following equation can be used to determine the efficiency of the proposed converter:

$$\eta = \frac{P_o}{P_{loss-Total} + P_o} \tag{40}$$

Fig. 8 displays the pie charts of the losses in step-up/down modes so that the power losses of each element's fraction can be understood. In comparison to the step-up mode, the efficiency in the step-down mode is computed as being lower.

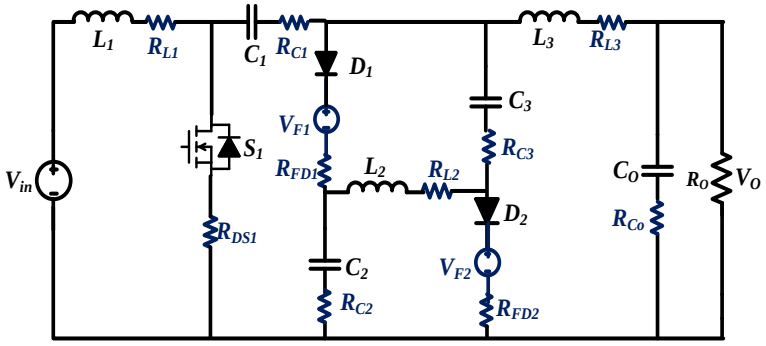

Fig. 7. Simplify the proposed converter by using parasitic parameters.

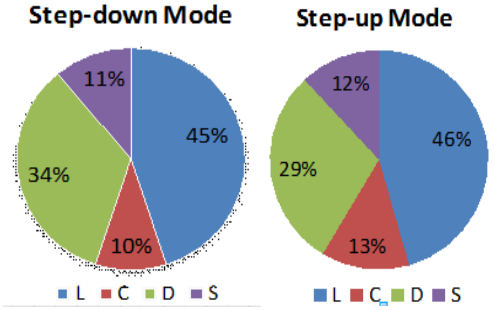

(a) ***(b)***

Fig. 8. Pie chart power loss. (a) Step-down mode, (b) Step-up mode.

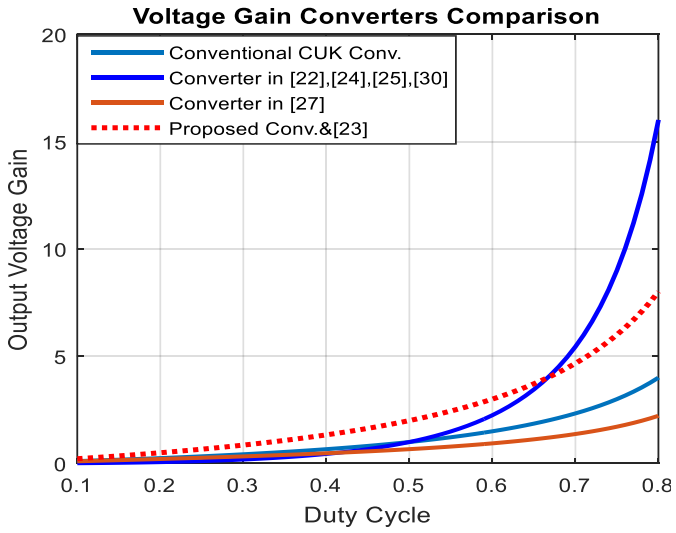

Fig. 9. Comparison of voltage gain with other similar converters.

Table 1. ***Comparative of the proposed converter with other similar converters.***

Ref.	Elements				Total Elements	V_D/V_{in}	V_S/V_{in}	M_{CCM}	Norm. SDP_{avg}/P_o	$\sum \frac{Vs}{Vin}$	Output Polarity	Continuous Input/output
	L	C	D	S								
CUK	2	2	1	1	6	$\frac{1}{1-D}$	$\frac{1}{1-D}$	$\frac{D}{1-D}$	----------	$\frac{1}{1-D}$	Negative	YES/YES
IN [30]	2	2	3	3	10	$\frac{1}{\frac{1-D}{D}}$ $\frac{D}{(1-D)^2}$	$\frac{1}{\frac{1-D}{D}}$ $\frac{D}{(1-D)^2}$	$\left(\frac{D}{1-D}\right)^2$	$\frac{D^2-D+2}{D(1-D)}$	$\frac{1}{(1-D)^2}$	Positive	YES/YES
IN [29]	2	2	2	2	8	$\frac{1}{1-D}$ $\frac{1}{(1-D)^2}$	$\frac{1}{1-D}$ $\frac{1}{(1-D)^2}$	$\frac{D}{(1-D)^2}$	$\frac{1+D}{D(1-D)}$	$\frac{2-D}{(1-D)^2}$	Positive	YES/NO
IN [22]	3	3	5	1	12	$\frac{1}{1-D}$ $\frac{D}{(1-D)^2}$ $\frac{1}{(1-D)^2}$ $\frac{1}{1-D}$ $\frac{D}{(1-D)^2}$	$\frac{1}{1-D}$ $\frac{1}{(1-D)^2}$	$\left(\frac{D}{1-D}\right)^2$	$\frac{6D^2-8D+4}{D(1-D)^2}$	$\frac{1}{(1-D)^2}$	Negative	YES/YES
IN [23]	3	4	2	1	10	$\frac{1}{1-D}$ $\frac{1}{1-D}$	$\frac{1}{1-D}$	$\frac{2D}{1-D}$	$\frac{1}{D(1-D)}$	$\frac{1}{1-D}$	Positive	NO/YES
IN [24]	3	3	2	2	10	$\frac{1}{1-D}$ $\frac{D}{(1-D)^2}$	$\frac{1}{1-D}$ $\frac{D}{(1-D)^2}$	$\left(\frac{D}{1-D}\right)^2$	$\frac{1+D}{D(1-D)}$	$\frac{1}{(1-D)^2}$	Positive	YES/YES
IN [25]	3	3	2	2	10	$\frac{1}{1-D}$ $\frac{D}{(1-D)^2}$	$\frac{1}{1-D}$ $\frac{D}{(1-D)^2}$	$\left(\frac{D}{1-D}\right)^2$	$\frac{1+D}{D(1-D)}$	$\frac{1}{(1-D)^2}$	Positive	YES/YES
IN [26]	3	3	2	2	10	$\frac{1}{1-D}$ $\frac{1}{(1-D)^2}$	$\frac{1}{1-D}$ $\frac{1}{(1-D)^2}$	$\frac{D}{(1-D)^2}$	$\frac{1+D}{D(1-D)}$	$\frac{1}{(1-D)^2}$	Negative	YES/YES
IN [27]	2	2	3	1	8	$\frac{1}{1-D^2}$ $\frac{D}{1-D^2}$ $\frac{D}{1-D^2}$	$\frac{1}{1-D}$	$\frac{D}{1-D^2}$	$\frac{1+3D^2-2D^3}{D-D^3}$	$\frac{1}{1-D}$	Negative	NO/NO
Proposed	3	3	2	1	10	$\frac{1}{1-D}$ $\frac{1}{1-D}$	$\frac{1}{1-D}$	$\frac{2D}{1-D}$	$\frac{1}{D(1-D)}$	$\frac{1}{1-D}$	Negative	YES/YES

3. COMPARATIVE ANALYSIS

The proposed buck-boost converter is compared to others in references [22]-[27] and [30], with a detailed analysis of factors like component count, normalized gain voltage, stress on switches and diodes, output polarity, continuous output/input current, and switching device power. The comparison demonstrates that the proposed converter exhibits superior voltage step-up across various duty cycles compared to those in [22]-[25], [27], and [30], as illustrated in Fig. 9.

The power loss and total implementation cost of a power converter are influenced by the current and voltage stress placed on its diodes and switches. Thus, it is necessary to assess these strains. As previously indicated in [33], the switching device power, or SDP, can be used as an illustrative metric to measure the converter cost and the power

loss. The formula for calculating the overall average switching device power (SDP_{avg}) is as follows:

$$SDP_{avg} = \sum_{i=1}^{n} V_{pk\_i} I_{avg\_i} \quad (41)$$

where I_{avg_i} and V_{pk_i} represent the average current and peak voltage during a switching period of the i^{th} semiconductor used in a power converter. The peak voltage and average current are computed for the diodes and the switch in the proposed converter. Overall average SDP is calculated,

$$SDP_{avg} = \left(\frac{1}{D(1-D)} \right) P_o \quad (42)$$

where P_o represents the output power.

The overall average SDPs of the several converters are presented in Fig. 10. It is noted that the recommended converter has a lower SDP than its rivals, which essentially means that there will be less power loss and semiconductor cost.

The voltage stress on the switch:

$$V_{S1} = \frac{1}{1-D} V_{in} \quad (43)$$

In Fig. 11, there is a comparison between the normalized sum of the voltage stress across power switches of the proposed converter and other similar converters. Additionally, Table 1 provides details on the voltage stress across power switches for other competing converters.

4. EXPERIMENTAL ANALYSIS

A 48W output power prototype of the proposed converter is constructed. A listing detailing the specific circuit components of the model is provided in Table 2. Fig. 12 illustrates simulation waveforms of the proposed converter operating in both step-down and step-up modes in Continuous Conduction Mode (CCM) using PLECS software. It is plotted gate-source voltage, switch voltage, inductor currents, diodes voltage, and output voltage.

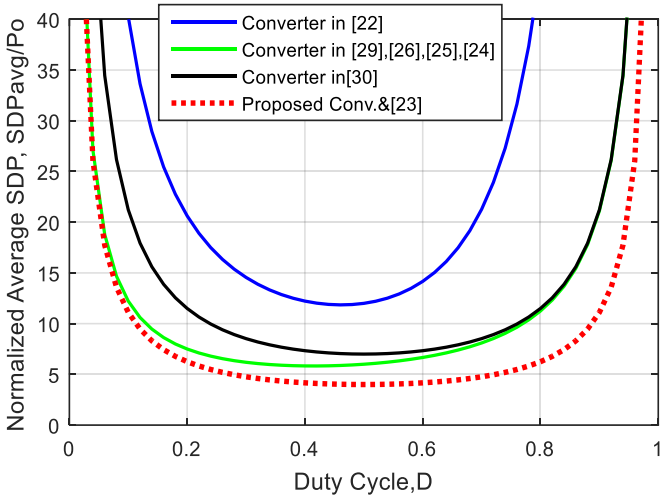

Fig. 10. Normalized total average switching device power (SDPavg/Po) of proposed converter vs other converter.

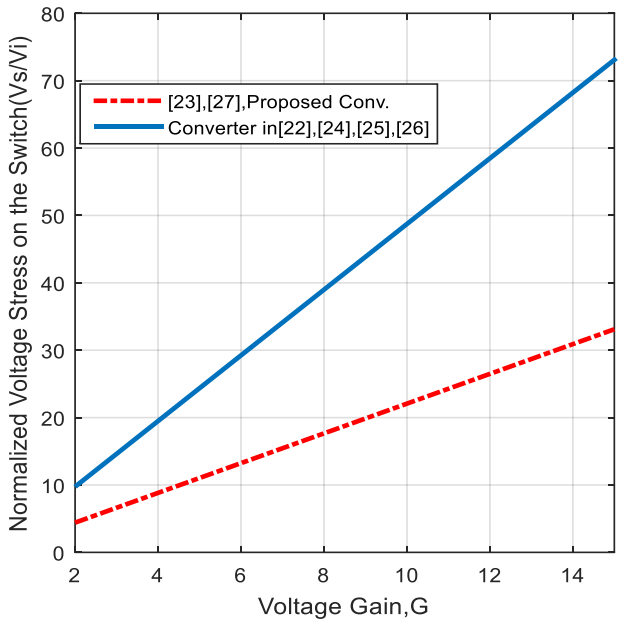

Fig. 11. Comparison of normalized switch voltage stress.

Table 2. ***Design considerations for the proposed converter***

Items	Prototype
fs	33KHZ
Duty Cycle	0.572 (step-up), 0.207 (step-down)
D_1/D_2	MBR10100 (V_F ~ 0.85V)
S_1	IRFP4668PBF (R_{DS} = 8mΩ)
C_1 / C_2 /C_o R_{C1} / R_{C2} / R_{Co}	33µF, 33µF, 160 µF 0.051Ω,0.078, 0.022Ω
L_1 / L_2 / L_3 R_{L1} / R_{L2} / R_{L3}	425µH, 860µH, 525 µH 0.035Ω, 0.157Ω,0.056 Ω
Vin	18V
V_o	48V (step-up),10V(step-down)

Fig. 13 shows a prototype created in the laboratory. The functioning of the converter and the numerical analysis have been validated using the lab prototype shown in Figs. 14 and 15. In these figures, the waveforms of the voltages and currents of the suggested converter are appeared in two modes that were measured in the laboratory. The efficiency of the proposed buck-boost converter with varying input voltages at different output powers is illustrated in Fig. 16. Since a high-duty cycle is necessary to achieve a high voltage gain by lowering the input voltage and so increasing conduction losses, the efficiency was reduced related to the input voltage drop. Since a high-duty

cycle is needed to achieve a high voltage gain by lowering the input voltage and thus increasing conduction losses, the efficiency was reduced concerning the input voltage drop. Fig. 17 shows the proposed converter's efficiency vs output power. Theoretical and experimental efficiencies are approximately the same, except for the step-up mode, which has a greater current ripple than the step-down mode.

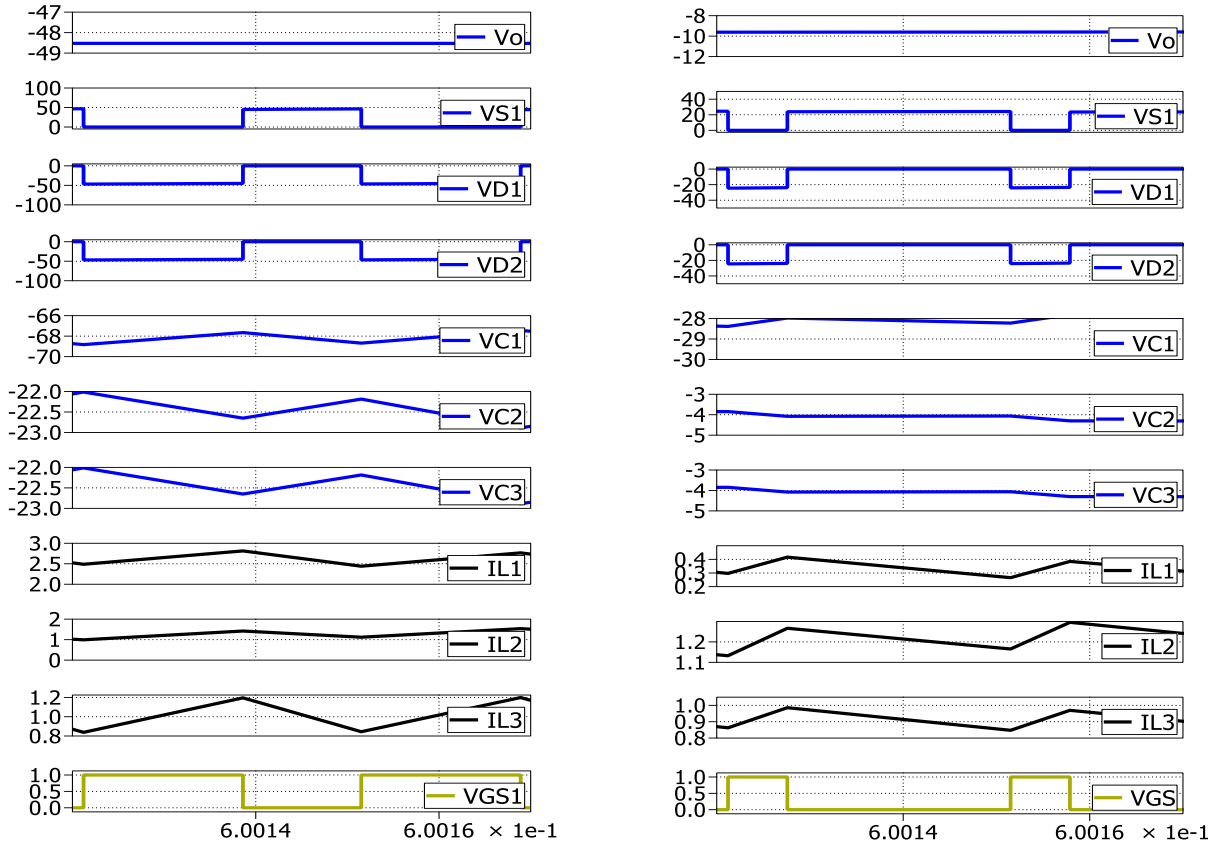

Fig.12. Simulation waveforms in PLECS of the proposed converter. (a) Step-up mode; (b) Step-down mode.

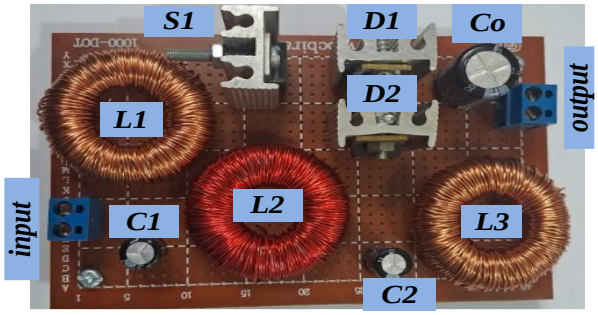

Fig. 13. Laboratory made prototype

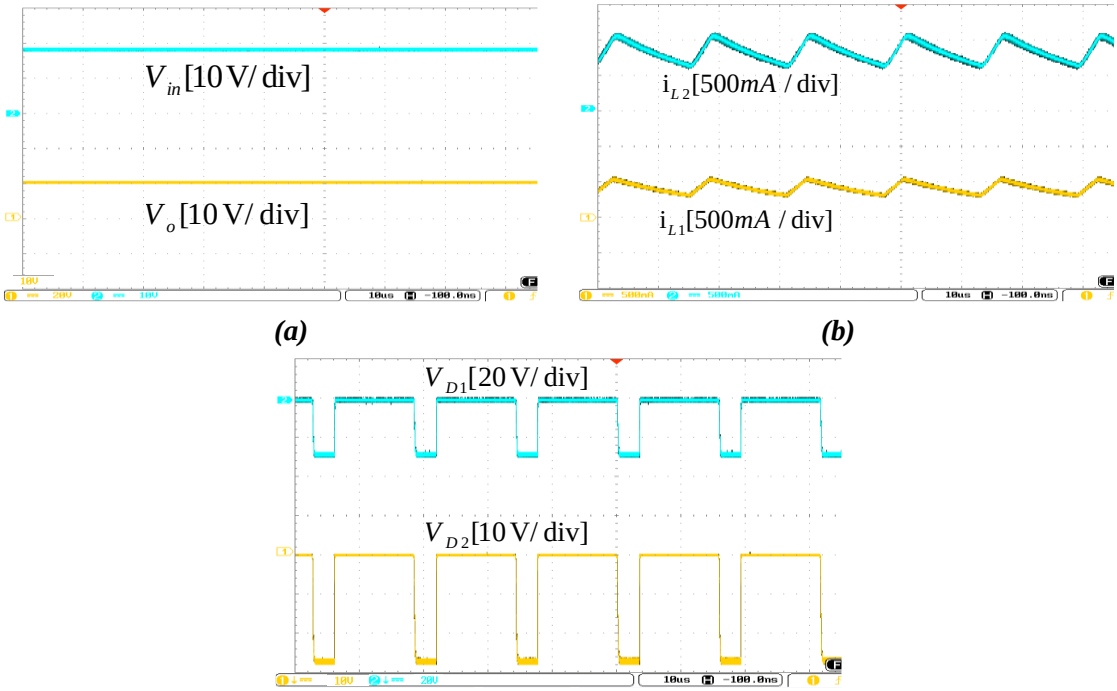

Fig. 14. Results of Laboratory in the step-down mode; (a) Vin, Vo; (b) iL1, iL2; (c) VD1, VD2.

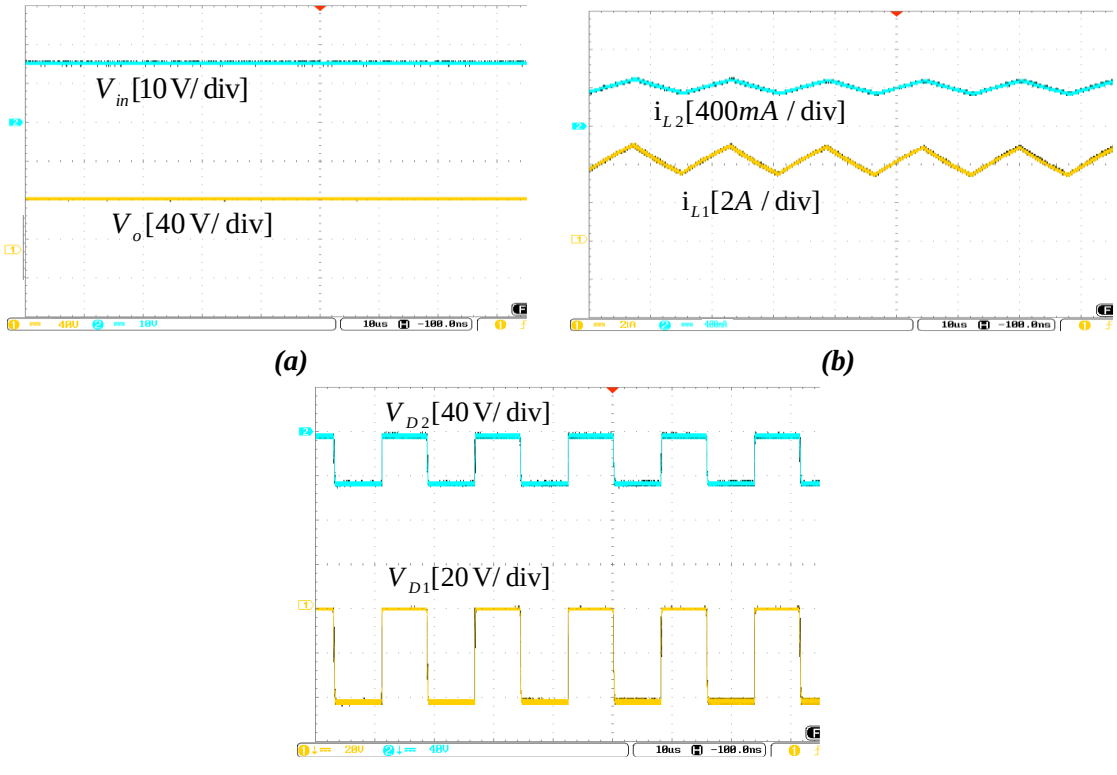

Fig.15. Results of Laboratory in the step-up mode; (a) Vin, Vo; (b) iL1, iL2; (c) VD1, VD2.

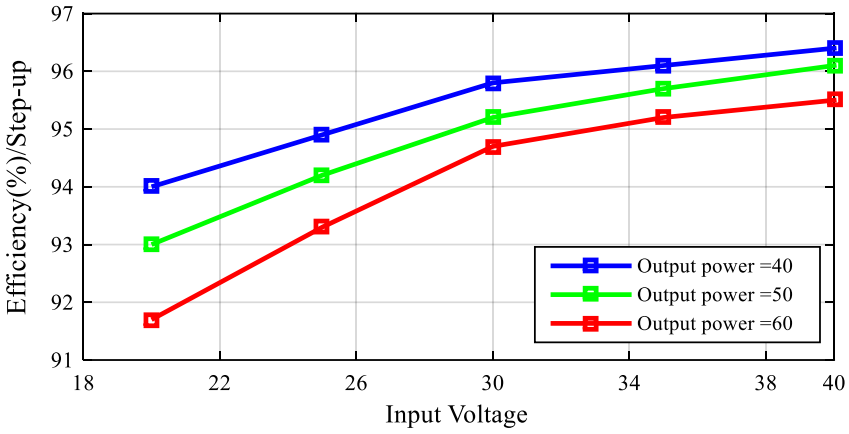

(a)

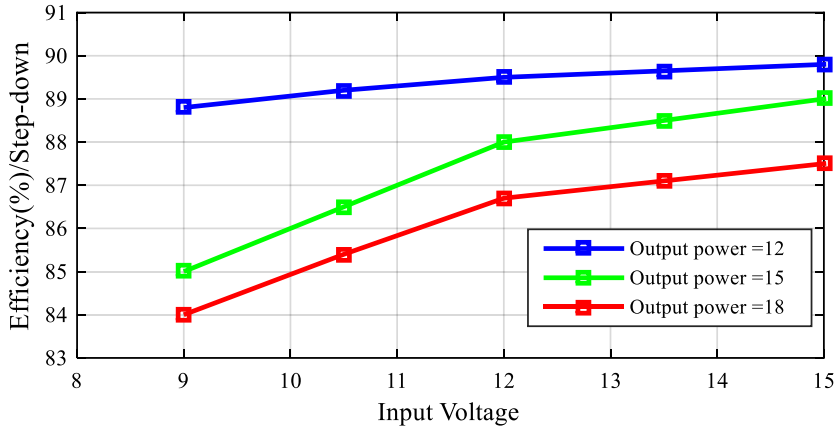

(b)

Fig. 16. Measured efficiency versus different input voltages and variable output powers (a) Step-up mode, (b) Step-down mode.

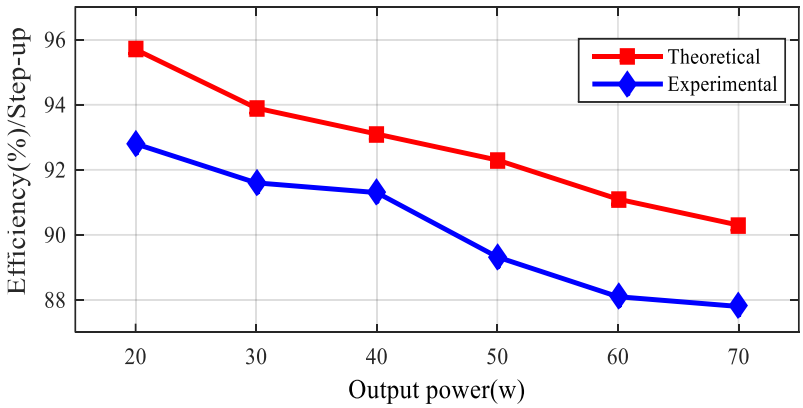

(a)

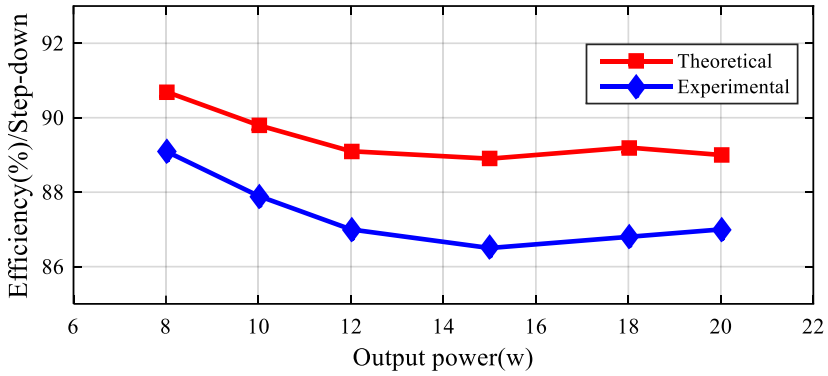

(b)

Fig. 17. Results of theoretical and experimental efficiency versus output power (a) Step-up mode (b) Step-down mode.

5. CONCLUSION

This investigation presents a DC-DC buck-boost converter characterized by negative output polarity for renewable energy purposes. In the suggested converter, a single switch is used in order to simplify the power MOSFET driving circuit and minimize the power loss. When employing the continuous input/output current port, less current ripple is observed in the output and input. A range of duty cycle values are employed for testing purposes in order to analyze and approve the functionality of the concerned converter. The efficiency of the suggested converter at an output power of 48W is 90.1%. In addition, the input/output current continuous characteristic of the suggested converter turns it into a suitable candidate for the purposes demanding a negative voltage source, e.g., multipurpose power supplies, photovoltaic systems, audio amplifiers, data transfer interfaces, and signal generators.

REFERENCES

[1] T. M. S. Bhaskar, M. Meraj, A. Iqbal, S. Padmanaban, P. K. Maroti, and R. Alammari, "High gain transformer-less double-duty-triplemode DC/DC converter for DC microgrid," IEEE Access, vol. 7, pp. 36353-36370, 2019.

[2] P. K. Maroti, S. Padmanaban, M. S. Bhaskar, M. Meraj, A. Iqbal, and R. Al-Ammari, "High gain three-state switching hybrid boost converter for DC microgrid applications," *IET Power Electron.*, vol. 12, no. 14, pp. 3656-3667, Nov. 2019.

[3] M. Forouzesh, Y. P. Siwakoti, S. A. Gorji, F. Blaabjerg, and B. Lehman, "Step-up DC_DC converters: A comprehensive review of voltage boosting techniques, topologies, and applications," IEEE Trans. Power Electron., vol. 32, no. 12, pp. 9143-9178, Dec. 2017.

[4] D. Kumar, F. Zare, and A. Ghosh, "DC micro grid technology: System architectures, AC grid interfaces, grounding schemes, power quality, communication networks, applications, and standardizations aspects," IEEE Access, vol. 5, pp. 12230-12256, 2017.

[5] N. Swaminathan and N.

Lakshminarasamma, "The steady-state DC gain loss model, efficiency model, and the design guidelines for high-power, high-gain, low-input voltage DC_DC converter," IEEE Trans. Ind. Appl., vol. 54, no. 2, pp. 1542-1554, Mar. 2018.

[6] R. Moradpour, H. Ardi, and A. Tavakoli, ``Design and implementation of a new SEPIC-based high step-up DC/DC converter for renewable energy applications," IEEE Trans. Ind. Electron., vol. 65, no. 2, pp. 1290-1297, Feb. 2018.

[7] P. K. Maroti, S. Esmaeili, A. Iqbal, and M. Meraj, "High step-up single switch quadratic modified SEPIC converter for DC microgrid applications," IET Power Electron., vol. 13, no. 16, pp. 3717-3726, Dec. 2020.

[8] I. Laird and D. D.-C. Lu, "High step-up DC/DC topology and MPPT algorithm for use with a thermoelectric generator," IEEE Trans. Power Electron., vol. 28, no. 7, pp. 3147-3157, Jul. 2013.

[9] E. Babaei, H. Mashinchi Maheri, M. Sabahi, and S. H. Hosseini, "Extendable nonisolated high gain DC_DC converter based on active passive inductor cells," IEEE Trans. Ind. Electron., vol. 65, no. 12, pp. 9478-9487, Dec. 2018.

[10] M. Lakshmi and S. Hemamalini, "Nonisolated high gain DC_DC converter for DC microgrids," IEEE Trans. Ind. Electron., vol. 65, no. 2, pp. 1205-1212, Feb. 2018.

[11] M. Forouzesh, K. Yari, A. Baghramian, and S. Hasanpour, "Single-switch high step-up converter based on coupled inductor and switched capacitor techniques with quasi-resonant operation," IET Power Electron., vol. 10, no. 2, pp. 240-250, Feb. 2017.

[12] H.-L. Jou, J.-J. Huang, J.-C.Wu, and K.-D.Wu, "Novel isolated multilevel DC_DC power converter," IEEE Trans. Power Electron., vol. 31, no. 4, pp. 2690-2694, Apr. 2016.

[13] G. Catona, E. Bianconi, R. Maceratini, G. Coppola, L. Fumagalli, G. Petrone, and G. Spagnuolo, "An isolated semi resonant DC/DC converter for high power applications," IEEE Trans. Ind. Appl., vol. 53, no. 3, pp. 2200-2209, May 2017.

[14] V. R. K. Kanamarlapudi, B.Wang, N. K. Kandasamy, and P. L. So, "A new ZVS full-bridge DC_DC converter for battery charging with reduced losses over full-load range," IEEE Trans. Ind. Appl., vol. 54, no. 1, pp. 571-579, Feb. 2018.

[15] S. Dwari and L. Parsa, "An efficient high-step-up interleaved DC_DC converter with a common active clamp," IEEE Trans. Power Electron., vol. 26, no. 1, pp. 66-78, Jan. 2011.

[16] G. Tibola, E. Lemmen, J. L. Duarte, and I. Barbi, "Passive regenerative and dissipative snubber cells for isolated SEPIC converters: Analysis, design, and comparison," IEEE Trans. Power Electron., vol. 32, no. 12, pp. 9210-9222, Dec. 2017.

[17] F. L. Tofoli, D. D. C. Pereira, W. J. de Paula, and D. D. S. O. Júnior, "Survey on non-isolated high- voltage step-up DC_DC topologies based on the boost

converter," IET Power Electron., vol. 8, no. 10, pp. 2044-2057, Oct. 2015.

[18] F. Mohammadzadeh Shahir, E. Babaei, and M. Farsadi, "Analysis and design of voltage-lift technique-based non-isolated boost DC-DC converter," IET Power Electron., vol. 11, no. 6, pp. 1083-1091, May 2018.

[19] Y. Tang, D. Fu, T.Wang, and Z. Xu, ``Hybrid switched-inductor converters for high step-up conversion," IEEE Trans. Ind. Electron., vol. 62, no. 3, pp. 1480-1490, Mar. 2015.

[20] N. Genc and I. Iskender, "DSP-based current sharing of average current controlled two-cell interleaved boost power factor correction converter," IET Power Electron., vol. 4, no. 9, pp. 1015-1022, Nov. 2011.

[21] B. Axelrod, Y. Berkovich, and A. Ioinovici, "Switched capacitor/ switched-inductor structures for getting transformerless hybrid DC_DC PWM converters," IEEE Trans. Circuits Syst. I, Reg. Papers, vol. 55, no. 2, pp. 687-696, Mar. 2008.

[22] N. Zhang, G. Zhang, K. W. See, and B. Zhang, "A Single-Switch Quadratic Buck–Boost Converter With Continuous Input Port Current and Continuous Output Port Current," *IEEE Transactions on Power Electronics*, vol. 33, pp. 4157-4166, 2018.

[23] M. R. Banaei, and H. A. F. Bonab, "A High Efficiency Non-Isolated Buck-Boost Converter Based on ZETA Converter," IEEE Transactions on Industrial Electronics, vol. 67, pp. 1991-1998, 2019.

[24] A. Sarikhani, B. Allahverdinejad, M. Hamzeh, and E. Afjei, "A continuous input and output current quadratic buck-boost converter with positive output voltage for photovoltaic applications," *Solar Energy*, vol. 188, pp. 19-27, 2019.

[25] M. Veerachary and M. R. Khuntia, "Design and Analysis of Two-Switch-Based Enhanced Gain Buck–Boost Converters," *IEEE Transactions on Industrial Electronics*, vol. 69, pp. 3577-3587, April 2022.

[26] M. Okati, M. Eslami, M. J. Shahbazzadeh, and H. Shareef, "A New Transformerless Quadratic Buck–Boost Converter with High Voltage Gain Ratio and Continuous Input/output Current Port," *IET Power Electronics*, vol. 15, pp.1280-1294, 2022.

[27] J. Li and J. Liu, "A Novel Buck–Boost Converter with Low Electric Stress on Components," *IEEE Transactions on Industrial Electronics*, vol. 66, pp. 2703-2713, 2019.

[28] J. Divya Navamani, A. Lavanya, D. Almakhles, and M. Jagabar Sathik, "A review on segregation of various high gain converter configurations for distributed energy sources, "Alexandria Engineering Journal, vol. 61, no. 1, pp. 675-700, Jan, 2022.

[29] M. Okati, M. Eslami, M. J. Shahbazzadeh, "A new transformerless DC/DC converter with dual operating modes and continuous input current port,". IET Generation, Transmission & Distribution. 2023.

[30] H. Gholizadeh, S. A. Gorji and D. Sera, "A Quadratic Buck-Boost Converter

with Continuous Input and Output Currents," in IEEE Access, vol. 11, pp. 22376-22393, 2023.

[31] N. Subhani, Z. May, M. K. Alam, I. Khan, M. A. Hossain and S. Mamun, "An Improved Non-Isolated Quadratic DC-DC Boost Converter With Ultra High Gain Ability," in IEEE Access, vol. 11, pp. 11350-11363, 2023.

[32] F. Mumtaz, N. Zaihar Yahaya, S. Tanzim Meraj, B. Singh, R. Kannan, and O. Ibrahim, "Review on non-isolated DC-DC converters and their control techniques for renewable energy applications," Ain Shams Engineering Journal, 2021.

[33] M. Shen, A. Joseph, J. Wang, F. Z. Peng, and D. J. Adams, "Comparison of Traditional Inverters and Z -Source Inverter for Fuel Cell Vehicles," IEEE Transactions on Power Electronics, vol. 22, pp. 1453-1463, 2007.

Signal Processing and Renewable Energy
September 2024, (pp. 21-34)
ISSN: 2588-7327
eISSN: 2588-7335

Design and Simulation of Two Low-Voltage, Low-Power Transresistance Instrumentation Amplifiers with Electronic Adjustment Capability

Yasin Safari[1,2], S. Mohammadali Zanjani[1,2*]

[1] Department of Electrical Engineering, Najafabad Branch, Islamic Azad University, Najafabad, Iran.
[2] Smart Microgrid Research Center, Najafabad Branch, Islamic Azad University, Najafabad, Iran.

Received: 20-May-2024, Revised: 19-Aug-2022, Accepted: 20-Aug-2024.

Abstract

This article introduces two designs for transresistance amplifiers. The first and second precision instrument amplifiers (IAs) utilize ten and eight MOS transistors. Both proposed IAs were simulated with 0.18 µm CMOS technology and a supply voltage of ±0.7 V using Hspice software. According to the results, the Common Mode Rejection Ratio (CMRR) of the first IA can vary from 72.6 dB to 75.7 dB with a change in control voltage. In contrast, the second IA can range from 71.7 dB to 74 dB. The -3dB cutoff frequency for the CMRR of the first IA is accessible between 0.969 MHz and 16.4 MHz, and for the second IA, it ranges from 4.34 MHz to 40.8 MHz. The power consumption of the first proposed design varies from 203.33 µW to 372.77 µW within the adjustment range, and for the second proposed design, it changes from 234.57 µW to 338.73 µW. Time-domain analysis indicates that for a 20 µA(p-p) input signal, the maximum Total Harmonic Distortion (THD) at various frequencies for the first design is 3.37%. For the second design, it is 2.13%. The output impedance of the first proposed amplifier can vary from 779 to 1190 Ω with a change in control voltage, and the second proposed IA can change from 860 Ω to 1640 Ω. Therefore, these two circuits are suitable for amplifier applications with electronic adjustability in medical instruments, biosensor reading circuits, electrocardiography, and signal processing.

Keywords: Instrumentation Amplifier, Current Mode, Transresistance Mode, Common Mode Rejection Ratio (CMRR).

***Corresponding Authors Email:** sma_zanjani@pel.iaun.ac.ir

1. INTRODUCTION

Instrumentation amplifiers, among the oldest and most utilized circuits, ensure the amplification of weak differential signals in the presence of noise and common-mode signals. Historically, instrumentation amplifiers were implemented using operational amplifiers and resistors [1]. Their main issue was the need for precise matching between resistors to achieve a high common-mode rejection ratio (CMRR). Another limitation associated with operational amplifier-based instrumentation amplifiers is their frequency-dependent gain. These weaknesses, coupled with the rapid scaling down of CMOS technology and lower allowable supply voltages, have made operational amplifier-based instrumentation amplifiers less attractive. In contrast to conventional voltage-mode signal processing, the new current-mode signal processing approach offers appealing features such as broad frequency performance, simpler circuitry, and low voltage operation. This new generation of instrumentation amplifiers is known as Current-Mode Instrumentation Amplifiers (CMIA) [2].

Numerous instrumentation amplifiers operate in voltage mode (VM) with voltage input and output or current mode (CM) with current input and output [3]. The rapid development of current-mode design and the emergence of many active elements have led to the introduction of amplifier structures based on Operational Transconductance Amplifier (OTA) [4], Differential Voltage Current Conveyor (DVCC) [5], Transconductance with Current Feedback or Current Feedback Operational Amplifier (CFOA) [6], Current-Controlled Current Conveyor Transconductance Amplifier (CCCCTA) [7], Current-Controlled Conveyor (CCCII) [8], and a resistorless current-mode instrumentation amplifier using 17 MOS transistors. On the other hand, low-voltage and low-power analog circuits are in high demand for easy integration and compatibility with digital systems [4,9].

In [10] the sensor uses a CNT as a movable electrode to sense gas pressure changes, and the proposed IA leverages the unique properties of CNTFETs to achieve high sensitivity, low noise, and low power consumption. This design eliminates the need for traditional resistors, providing a more efficient and compact solution for gas pressure sensing applications.

The article [11] examines various IA topologies with programmable gain capabilities (PG-IA). The study covers different implementation techniques, including Single Op-amp IA, Two and Three Op-amp IA, Switched Capacitor IA (SCIA), Current Feedback IA (CFIA), and Current Mirror IA (CMIA). The research highlights the advantages of using PG-IA in applications requiring high precision, high CMRR, low noise, and low power dissipation. The paper also discusses using V-to-I and I-to-V converters, Current Division Network (CDN), and Supply Current Sensing (SCS) approaches to enhance the performance of PG-IAs.

In [12], the amplifier is tailored for biomedical applications such as ECG, EEG, and EMG signal analysis. It features high CMRR, low power consumption, and the ability to operate at low voltages as shown in Table 2.

The device presented in [13], utilizes LM324/LM741 op-amps configured as an IA for precise signal amplification for portable ECG devices. It incorporates a 50 Hz notch filter and an active band-pass filter to eliminate noise and ensure signal integrity. The amplified signal is then digitized using an ESP-32 microcontroller, enabling the transmission of ECG data to an IoT platform for remote monitoring.

The article [14] presents a capacitively coupled chopper IA (CCIA) designed for biomedical applications. The amplifier operates with an ultra-low power consumption and utilizes a programmable bandwidth from 0.2 to 10 kHz. It incorporates a squeezed inverter amplifier (SQI) using a 0.2 V supply to efficiently address the primary noise source. The CCIA is implemented using 0.18 µm CMOS technology, achieving a high CMRR of 117.7 dB, and consuming only 0.47 µW of power. The design aims to provide flexible bandwidth without additional power consumption, making it suitable for wearable or implantable biomedical devices.

The development of a low-power, low-noise current-feedback IA for ECG acquisition is discussed in [15]. The design leverages a gm-boosted OTA to enhance performance while minimizing power consumption. Implemented in a 0.18 µm CMOS technology, the amplifier achieves a high CMRR and low power dissipation, making it suitable for portable and wearable biomedical devices.

The article [16] presents the design of a capacitively coupled IA using a novel hybrid feedback resistor. This IA is designed for physiological signal acquisition, addressing the need for high input impedance and precise amplification of low-frequency, low-amplitude signals. Implemented in a 130 nm CMOS process, the IA achieves a high-pass corner of 73.9 mHz and demonstrates robustness against process, voltage, and temperature (PVT) variations. Combining switched-capacitor (SC) low-pass filters, SC resistors, and continuous-time low-pass filters, allows the IA to achieve high resistance values with minimal sensitivity to PVT changes.

The current-mode approach has recently attracted attention in integrated circuit design due to its numerous advantages (such as high bandwidth, wide dynamic range, high linearity, low power consumption, and circuit simplicity) over the voltage-mode approach [3, 17-19]. Thus, this article will present an improved current-mode instrumentation amplifier with a differential input transconductance amplifier followed by a current follower. The second section elaborates on the principles and fundamentals of the proposed instrumentation amplifier. The third section presents the simulation results of the designed circuit to confirm the efficiency of the proposed structure. These results are compared with some of the recent works. Finally, the article concludes in the fourth section.

2. PROPOSED INSTRUMENTATION AMPLIFIERS

The first proposed instrumentation amplifier, which uses only ten MOS transistors, is shown in Fig. 1, and the second proposed amplifier, using only eight MOS transistors, is displayed in Fig. 2. These amplifiers are constructed from two current mirrors, a

unity-gain inverting amplifier, and two MOS transistors acting as a voltage-controlled resistor. Transistors M1 to M4 are utilized to invert the input current I1. The input current I2 is summed with the inverted current (I1) and converted to voltage through the equivalent resistance (R_{eq}).

The voltage difference across the gate inputs of M1 and M2 determines the current difference across their drains as Eq (1).

$$\Delta V_{GS} = V_{GS1} - V_{GS2} \quad (1)$$

The drain currents of M1 and M2 are related by the voltage difference across their gates.

$$ID_1 - ID_2 = f(\Delta v_{GS}) \quad (2)$$

Transistors M3 and M4, together with M5 and M6, form active loads on the drains of M1 and M2. These active loads improve the gain of the differential amplifier.

$$ID_1 \approx IM_3 + IM_4$$
$$ID_2 \approx IM_5 + IM_6 \quad (3)$$

The output of the amplifier is taken from the node between transistors M5 and M6. Then the output voltage is described as Eq (4).

$$V_{OUT} = VDD - R_{OUT} ID_2 \quad (4)$$

$$I_{SS} = ID_1 + ID_2 = I_b \quad (5)$$

M5 and M6 form a unity-gain inverting amplifier, transferring the generated voltage through Req to the output node. The *W/L* ratio of transistors M5 and M6 should be sufficiently large to ensure a low output impedance.

It is evident that the second proposed design requires fewer transistors in its variable resistance structure and also does not need a separate voltage source to bias the non-ideal current source. A simple node analysis of the circuit in Fig. 2 concludes:

$$V_{out} = (I_1 - I_2) R_{eq} \quad (6)$$

For a differential input $I_{id} = I_1 - I_2$, the differential mode gain (A_d) of the proposed amplifier is obtained as follows:

$$A_d = \frac{V_{out}}{I_{id}}\bigg|_{I_1 = -I_2} = R_{eq} \quad (7)$$

The R_{eq} can be adjusted by the parameters of four MOS transistors and the control voltages V_C and $-V_C$, which provides the highly desirable feature of electronic adjustability. Furthermore, the proposed amplifier is suitable for integration due to the

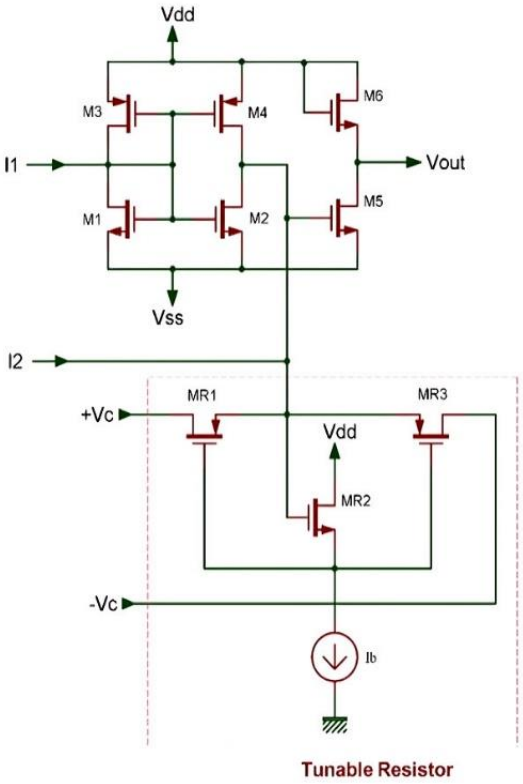

Fig. 1. First proposed IA.

ease of implementing the grounded resistance. Assuming that MR_1 and MR_2 have equal ratios, the equivalent resistance is expressed as follows [17]:

$$R_{eq} = \frac{L}{2\mu C_{ox} W (V_C - V_{TH})} \quad (8)$$

In this context, *W* and *L* represent the width and length of the transistor channel, respectively. The equivalent resistance R_{eq} can be adjusted by varying the control voltages $+V_C$ and $-V_C$, which modulate the resistance of the MOS transistors operating in the linear region. This electronic adjustability is a significant advantage as it allows fine-tuning the amplifier's performance without requiring physical changes to the circuit components.

As evident from Eq (1), for a common-mode input I_{icm} = 0.5 (I_1+I_2), the common-mode gain (A_C) of the proposed instrumentation amplifier in Fig. 2 is derived as shown in Eq (9).

$$A_c = \frac{V_{out}}{\frac{I_1+I_2}{2}}|_{I_1=I_2} = 0 \quad (9)$$

As can be inferred from Equ (4), the common-mode gain of the proposed amplifier in an ideal state is equal to zero. Consequently, Eq (5) indicates that the proposed amplifier has a very high intrinsic CMRR [18].

$$CMRR = \left|\frac{A_d}{A_c}\right| = \infty \quad (10)$$

However, if the non-ideal gains of current mirrors and inverting amplifiers are considered as unity, the output is assumed as Eq (11):

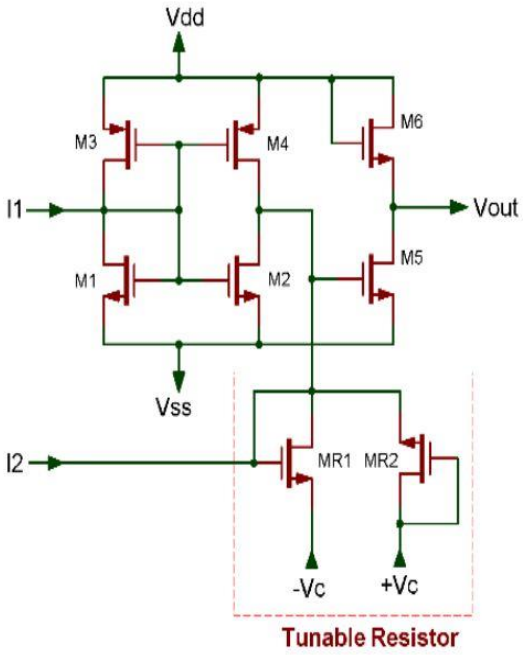

Fig. 2. Second proposed IA.

$$V_{out} = \beta(\alpha I_1 - I_2)R_1 \quad (11)$$

Here, α and β represent the non-ideal gains of current mirrors and the inverting voltage amplifier. Therefore, considering that $I_1 = I_{icm} + I_{id}/2$ and the differential gain (A_d), the common-mode gain (A_C), and the *CMRR* in the proposed amplifier, Eqs (12) to (14) can be calculated.

$$A_d = \frac{R_1}{2}\beta(\alpha + 1) \quad (12)$$

$$A_c = \beta R_1(\alpha - 1) \quad (13)$$

$$CMRR = \frac{1}{2}\left|\frac{\alpha + 1}{\alpha - 1}\right| \quad (14)$$

Eq (9) shows that the inverting voltage amplifier's non-ideal gain does not significantly affect the CMRR. On the other hand, if α is close to 1, a very high CMRR can be achieved [17,118].

3. SIMULATION RESULTS OF THE PROPOSED CIRCUITS

The first proposed design, utilizing 180 nm CMOS technology, was simulated under a supply voltage of ±0.7 V and at a default temperature of 25 °C. The threshold voltage (V_{TH}) for the NMOS transistors is approximately 0.4 V. All transistors operate in the saturation region, and a 10 kΩ load resistance is connected to the output. In the proposed circuit, the value of Vc was varied from zero to 0.7 V to achieve different differential mode gains. Fig. 3(a) shows that the differential mode gain of the proposed circuit varies from 75.9 dB to 77.9 dB with a -3dB bandwidth ranging from 76.2 MHz to 345 MHz. The proposed instrument amplifier's minimum and maximum power

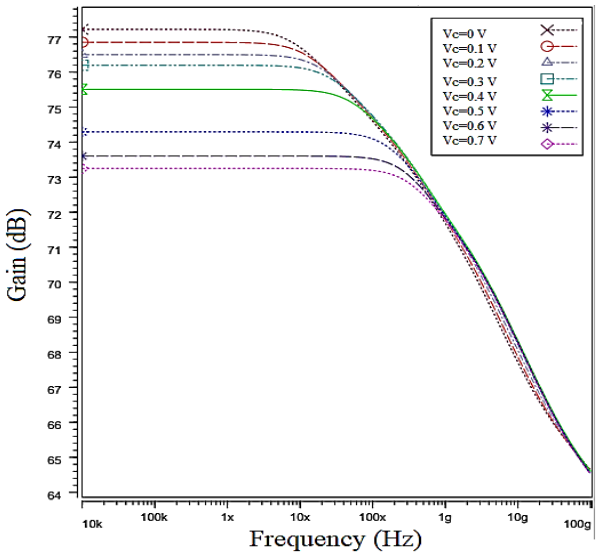

(a)

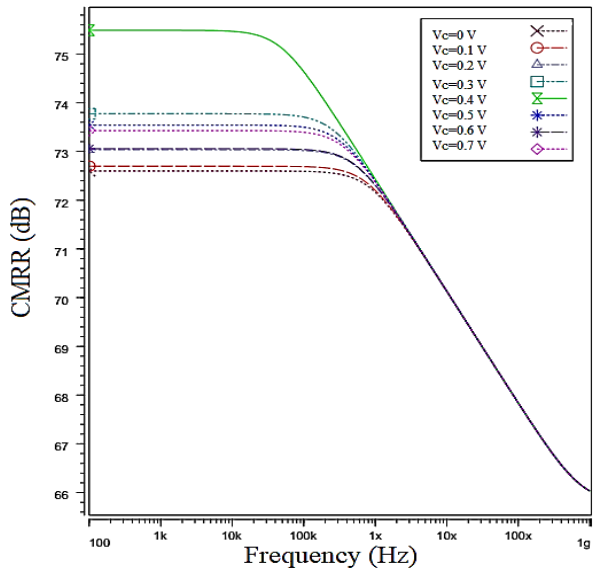

(b)

Fig. 3. (a) Frequency response (b) CMRR variations in the first proposed IA.

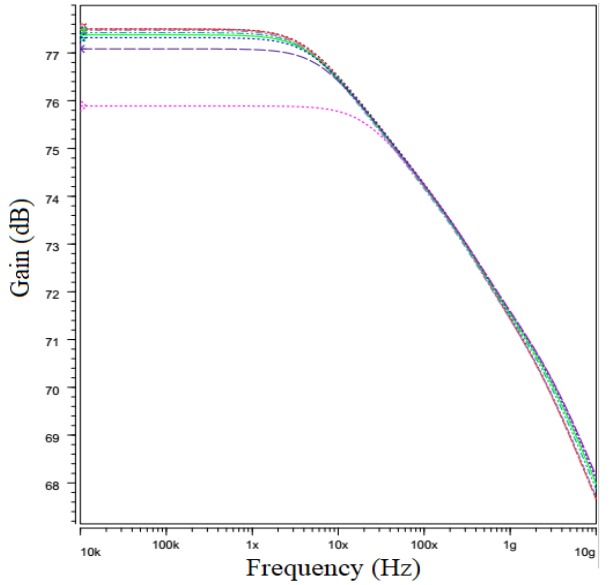

(a)

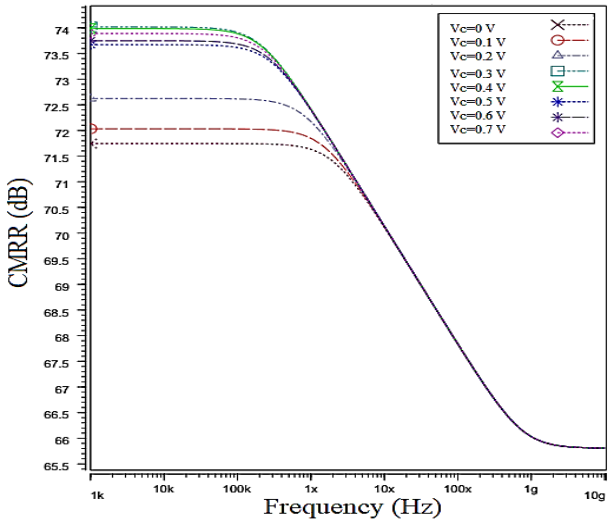

(b)

Fig. 4. (a) Frequency response (b) CMRR variations in the second proposed IA.

consumption in the adjustable range are 203.33 µW and 372.77 µW, respectively. The changes in CMRR in the proposed amplifier relative to frequency for different Vc values are shown in Fig. 3(b). As observed, the CMRR value of the proposed circuit varies from 72.6 dB to 75.7 dB, with a -3dB bandwidth ranging from 0.916 MHz to 16.4 MHz. It can be inferred that the proposed structure can effectively reduce unwanted common-mode signals while having a straightforward structure consisting of ten transistors.

In the proposed second circuit, the value of V_c was varied from 0 to 0.7 V to achieve different differential mode gains. Fig. 4(a) shows that the differential mode gain of the proposed circuit varies from 73.2 dB to 77.2 dB, with a -3dB bandwidth ranging from 148 MHz to 3.23 GHz. The proposed

instrumentation amplifier's minimum and maximum power consumption within the adjustable range are 157.15 µW and 338.73 µW, respectively. Changes in CMRR relative to frequency for different values of V_c are shown in Fig. 4(b). As observed, the CMRR value of the proposed circuit ranges from 71.7 dB to 74 dB, with a -3dB bandwidth ranging from 4.34 MHz to 40.8 MHz. It can be inferred that the proposed structure can effectively reduce unwanted common-mode signals while having a simple structure composed of eight transistors.

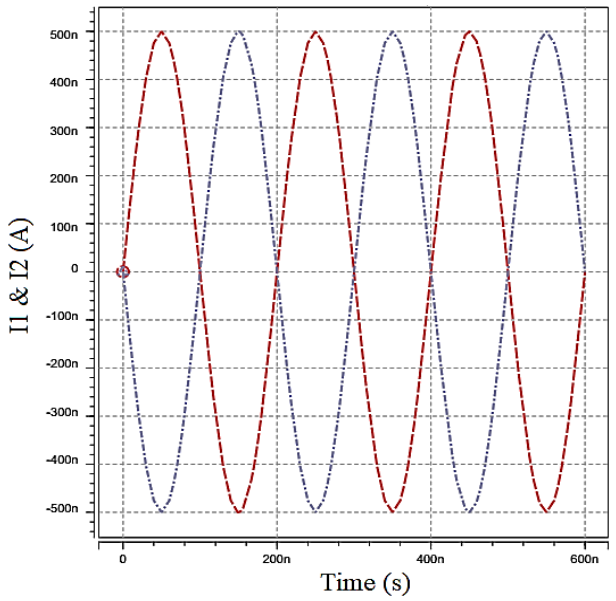

(a)

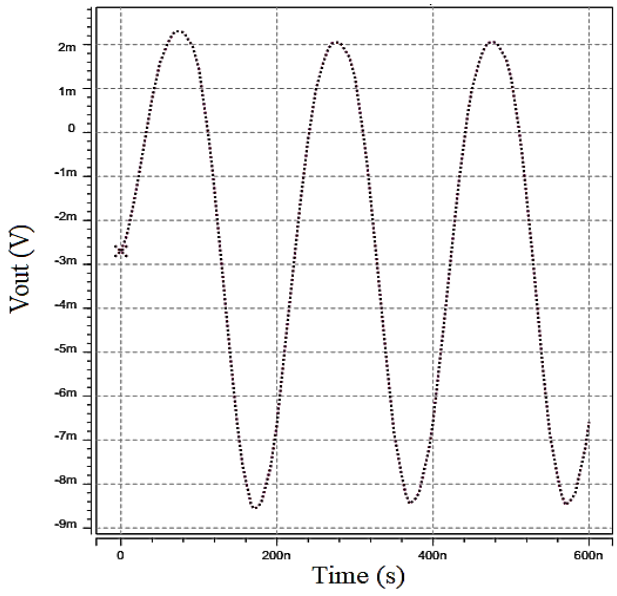

(b)

Fig. 5. Transient response of the 1st proposed IA. (a) differential input currents, (b) output voltage.

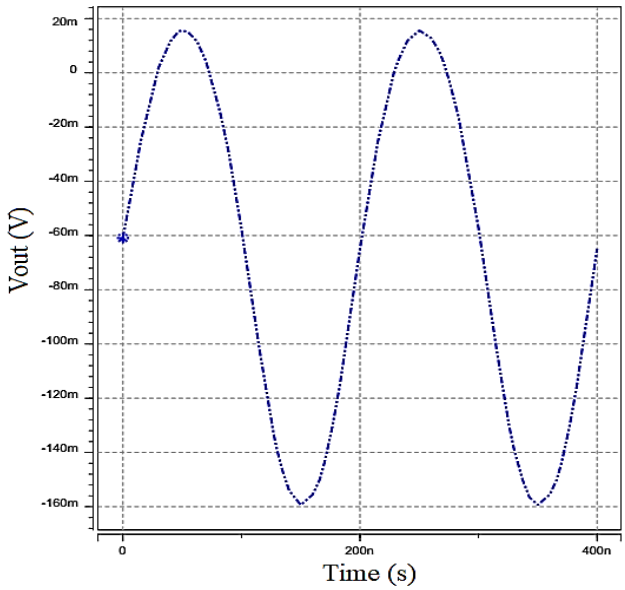

(a)

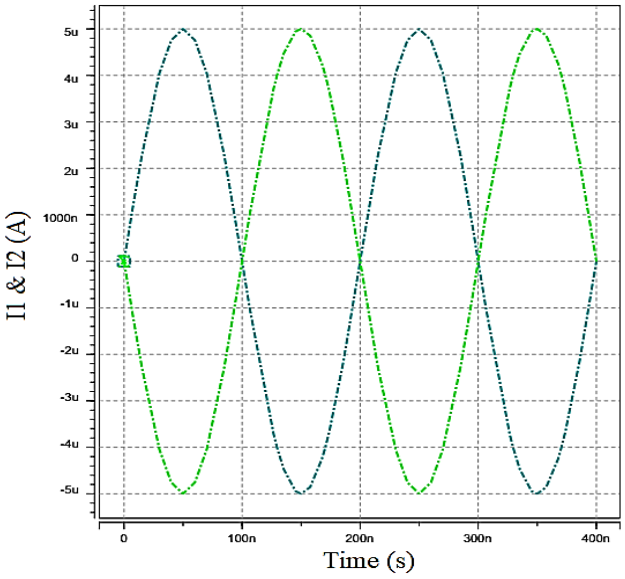

(b)

Fig. 6. Transient response of the 2nd proposed IA. (a) differential input currents, (b) output voltage.

To evaluate the time-domain response of the first proposed amplifier, a differential-mode sinusoidal input (I_1-I_2) with a peak-to-peak amplitude of 20 µA at a frequency of 5 MHz was applied to the inputs. The control voltage was set to 0.5 V. Fig. 5 shows that the amplified output voltage is approximately 11 Mv(p-p), with a differential-mode gain of 77.2 dB and a Total Harmonic Distortion (THD) of 3.37 percent. Additionally, the THD value remains below 3% for various frequencies.

To examine the proposed second amplifier's time-domain response, a differential-mode sinusoidal input with a peak-to-peak amplitude of 20 µA at a frequency of 5 MHz was applied to the inputs. The control voltage V_c was set to 0.5

V. Fig. 6 shows that the amplified output voltage is approximately 170 mV(p-p), with a differential mode gain of 77.2 dB and a Total Harmonic Distortion (THD) of 2.13%. Additionally, the THD value remains below 0.5% for different frequencies.

To investigate the changes in CMRR for the first proposed design under mismatch conditions, a Monte-Carlo simulation considering Process, Voltage, and Temperature (PVT) variations for the transistors was carried out across 100 runs with Vc = 0.5 V. The statistical distribution of CMRR in the presence of mismatch is shown in Fig. 7(a). As observed from the Monte Carlo simulation results, the first proposed structure displays a CMRR value of 69 dB with the highest probability.

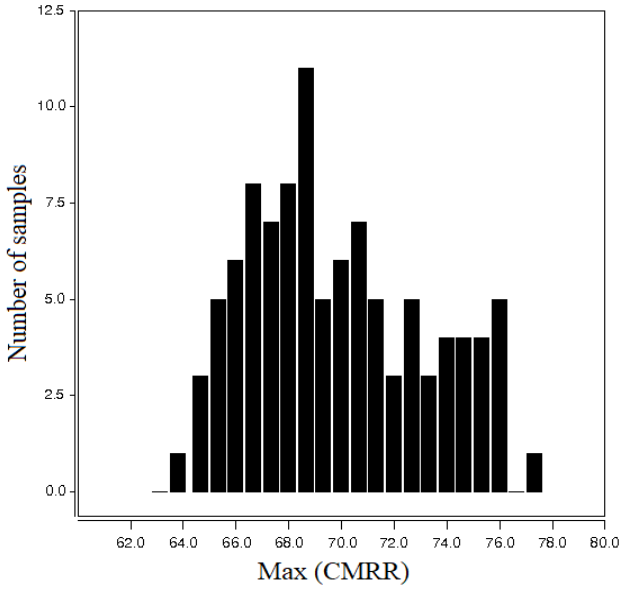

(a)

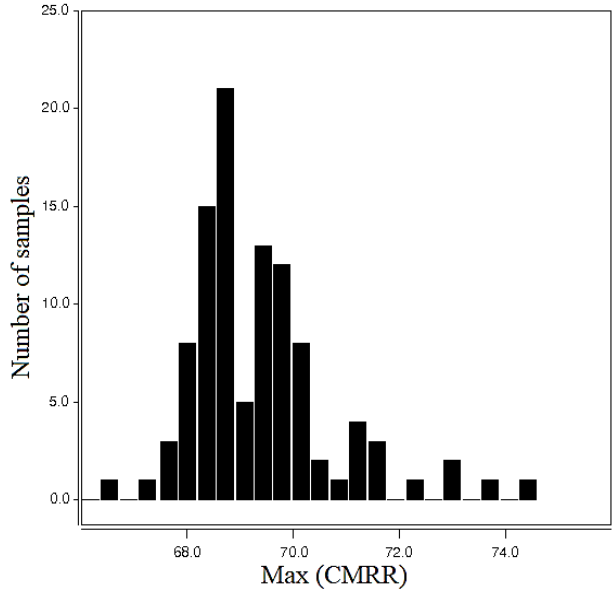

(b)

Fig. 7. Transient response of the 1st proposed IA. (a) differential input currents, (b) output voltage.

Table 1. ***Comparison between the simulation results of the first and second proposed IAs.***

parameter	First proposed circuit	Second proposed circuit
Technology (nm)	180	180
Supply voltage (V)	±0.7	±0.7
power consumption (µw)	203.33 ~ 372.77	157.15 ~ 338.73
Differential mode gain (dB)	75.9 ~ 77.5	73.2 ~77.2
f_{-3dB} (MHz)	76.2 ~ 345	148 ~ 323
CMRR (dB)	72.6 ~ 75.7	71.7 ~ 74
Output-referenced noise at 10 kHz (pA/$\sqrt{Hz}$)	64.6	77.8
Output Impedance (**Ω**)	779 ~ 1190	860 ~ 1640
Linearity percentage @ 5 MHz and 1 µA (p-p)	3.37	2.13
Chip area (µm^2)	1030.2	861

A similar Monte Carlo analysis was conducted to examine the changes in CMRR. Table 1 compares the results of the first and second proposed designs. Both proposed designs have similar differential mode gain and common-mode rejection ratio values. The disadvantages of the first proposed design include high power consumption, low -3dB cutoff frequency, large occupied area, and worse linearity. Therefore, for comparison with previous works, the second proposed design is considered.

The second proposed design is considered under mismatch conditions. The statistical distribution of CMRR in the presence of mismatch is illustrated in Fig. 7(b). According to the simulation results, the second proposed structure indicates a CMRR value of approximately 68.75 dB with the highest probability. Both outcomes demonstrate robust performance against PVT variations.

A comparison of the proposed instrumentation amplifier with some other reported works is presented in Table 2. The transistor characteristics, including the technology node, and applied power supply are specified to ensure a fair comparison with similar reported works. It is observed from Table 2 that the proposed instrumentation amplifier exhibits lower power consumption, fewer transistors, and electronic adjustability, demonstrating superior performance compared to previous works.

4. CONCLUSION

This article introduces two precision IAs with 10 and 8 transistors. The second IA is more suitable for integration due to its simple structure achieved by having only two transistors between the power supply lines, resulting in a very low supply voltage. The differential gain of the proposed precision

Table 2. ***Comparison between the proposed instrumentation amplifier and some reported works.***

	Year	●	Active Elements Used	■	◊	# R&C	CMRR (dB)	f_{-3dB} (MHz)	☼	Power diss. (mW)	Area (mm^2)
[2]	2013	180	--	✓	17	0	91	-	±0.8	0.219~0.446	-
[7]	2020	180	DDCC (#1)	×	40	0	146	1	±0.8	0.492	-
[11]	2023	130	IA, Op-Amps, OTAs	✓	4 Op-Amps & OTAs,	Multi.	120	83	3.3	0.77	-
[12]	2022	130	OTAs-	✓	3 OTAs	0	54	Varied	1.8	90	-
[13]	2023	-	LM324/741, Op-Amps, ESP-32	×	-	Multi.	96	0.5-250 Hz	±5	-	-
[14]	2023	180	SQI Amplifier and Transistors	✓	-	Multi.	117.7	0.2-10 kHz	0.2, 0.8	0.00047	0.083
[15]	2023	180	gm-boosted OTA	×	-	Multi.	110	-	0.8	0.55	-
[16]	2024	130	Switched-capacitor filter, SCR, PR	×	-	Multi.	-	0.0739	-	-	0.16
[17]	2017	180	COA (#2)	✓	29	2	36~54.2	0.359~0.383	±0.9	0.76	-
[18]	2018	180	COA (#2)	✓	30	1	51.2	0.068	±0.9	0.864	-
[19]	2018	180	CFDITA (#2)	✓	34	0	52.8~64.7	3.76~46.2	±0.9	1.15~1.3	-
[20]	2009	350	CCCCTA (#2)	✓	34	0	94	-	±1.5	4.43	-
[21]	2023	180	DVTA (#3)	✓	24	1	146.8	30	±0.9	0.368	0.0095
*	-	180	-	✓	8	0	71.7~74	4.34~40.8	±0.7	0.157~0.338	0.00086

● = Technology (nm) ; ■ = Adjustability ; ◊ = #Transistors & Active Comp. ; ☼ = Power Sup. (V) ; * = Proposed

instrumentation amplifier can be electronically adjusted by changing the control voltages. Furthermore, a high CMRR is achieved using only eight MOS transistors, eliminating the need for resistance matching. The proposed amplifier was simulated using 0.18 µm CMOS technology with a ±0.7 V supply voltage. Simulation results indicate that the CMRR of the proposed precision instrumentation amplifier can vary from 71.7 to 74 dB with control voltage adjustments. The f3dB for the CMRR varies between 4.34 ~ 40.8 MHz. The power consumption of the proposed design varies from 234.57 µW to 338.73 µW during adjustment. Time-domain analysis revealed that for an input signal with

a 10 µA peak, the maximum THD is 0.21%. Additionally, the Rout of the proposed precision IA can vary between 860 ~ 1640 Ω with control voltage adjustments.

REFERENCES

[1] T. A. Baghi-Rahin, V. Baghi-Rahin, "A 0.5 V operational transconductance amplifier based on dynamic threshold-voltage MOSFET and floating gate MOSFET inverters in 180 nm CMOS technology," Journal of Intelligent Procedures in Electrical Technology (JIPET), Vol. 15, no. 60, pp. 1-18, March 2025 (in Persian).

[2] Safari, L., & Minaei, S. (2013). A novel resistor-free electronically adjustable current-mode instrumentation amplifier. *Circuits, Systems, and Signal Processing*, *32*, 1025-1038.

[3] Yuce, E. (2010). Various current-mode and voltage-mode instrumentation amplifier topologies suitable for integration. *Journal of Circuits, Systems, and Computers*, *19*(03), 689-699.

[4] Baghi Rahin, A., & Baghi Rahin, V. (2019). A new 2-input CNTFET-based XOR cell with ultra-low leakage power for low-voltage and low-power full adders. *Journal of Intelligent Procedures in Electrical Technology*, *10*(37), 13-22.

[5] Zanjani, S. M. A., & Parvizi, M. (2021). Design and simulation of a bulk driven operational trans-conductance amplifier based on CNTFET technology. *Journal of Intelligent Procedures in Electrical Technology*, *12*(45), 65-76.

[6] Pertijs, M. A., & Kindt, W. J. (2010). A 140 dB-CMRR current-feedback instrumentation amplifier employing ping-pong auto-zeroing and chopping. *IEEE Journal of Solid-State Circuits*, *45*(10), 2044-2056.

[7] Ettaghzouti, T., Bchir, M., & Hassen, N. (2020). High CMRR voltage mode instrumentation amplifier using a new CMOS differential difference current conveyor realization. *International Journal of Electrical and Electronic Engineering & Telecommunications*, *9*(3), 132-141.

[8] Maheshwari, S. (2003). High CMRR wide bandwidth instrumentation amplifier using current controlled conveyors. *International Journal of Electronics*, *89*(12), 889-896.

[9] Rahin, A. B., & Kanani, Z. D. K. (2014). A Low-Voltage and Low-Power Programmable Gm-C Filter for Wireless Applications. *Journal of Intelligent Procedures in Electrical Technology (JIPET)*, *5*(19), 3-10.

[10] Zanjani, S. M. A., Dousti, M., & Dolatshahi, M. (2018). High-precision, resistor less gas pressure sensor and instrumentation amplifier in CNT technology. *AEU-International Journal of Electronics and Communications*, *93*, 325-336.

[11] Sharma, D., Shylashree, N., Prasad, R., & Nath, V. (2023). Analysis of Programmable Gain Instrumentation Amplifier. *Int. J. Microsyst. Iot*, *1*, 41-47.

[12] Gajare, M., & Shedge, D. K. (2022). CMOS trans conductance based

instrumentation amplifier for various biomedical signal analysis. *NeuroQuantology*, *20*(5), 53.

[13] Raptan, S., Bhattacharyya, A., Das, N., Pandey, I., & Bhattacharjee, S. (2023, March). "Cardioxy"–A Novel and Portable Instrumentation Amplifier based and IoT enabled ECG device. In *2023 2nd International Conference for Innovation in Technology (INOCON)* (pp. 1-5). IEEE.

[14] Pham, X. T., Kieu, X. T., & Hoang, M. K. (2023). Ultra-Low Power Programmable Bandwidth Capacitively-Coupled Chopper Instrumentation Amplifier Using 0.2 V Supply for Biomedical Applications. *Journal of Low Power Electronics and Applications*, *13*(2), 37.

[15] Gupta, S. K., Ahmad, R., Singh, P., Boolchandani, D., & Kar, S. K. (2023, March). A Low-Power Low-Noise Current-Feedback Instrumentation Amplifier based on g m boosted OTA for ECG Acquisition. In *2023 10th International Conference on Signal Processing and Integrated Networks (SPIN)* (pp. 733-738). IEEE.

[16] Xu, H., Liu, Y., Duan, Y., Li, T., Zhang, J., Li, Z., & Zhang, H. (2024). A PVT-Robust and 73.9 mHz High-Pass Corner Instrumentation Amplifier with an SCF-SCR-PR Hybrid Feedback Resistor. *Electronics*, *13*(2), 366.

[17] Safari, L., & Minaei, S. (2017). A novel COA-based electronically adjustable current-mode instrumentation amplifier topology. *AEU-International Journal of Electronics and Communications*, *82*, 285-293.

[18] Safari, L., Minaei, S., Ferri, G., & Stornelli, V. (2018). Analysis and design of a new COA-based current-mode instrumentation amplifier with robust performance against mismatches. *AEU-International Journal of Electronics and Communications*, *89*, 105-109.

[19] Chaturvedi, B., & Kumar, A. (2018). Electronically tunable current-mode instrumentation amplifier with high CMRR and wide bandwidth. *AEU-International Journal of Electronics and Communications*, *92*, 116-123.

[20] Chanapromma, C., Tanaphatsiri, C., & Siripruchyanun, M. (2009, February). An electronically controllable instrumentation amplifier based on CCCCTAs. In *2008 International Symposium on Intelligent Signal Processing and Communications Systems* (pp. 1-4). IEEE.

[21] Raj, N., Dutta, S., Ranjan, R. K., Singh, D. K., & Kuntman, H. (2023). VDTA Based Transadmittance Mode Instrumentation Amplifier with Experimental results.

Signal Processing and Renewable Energy
September 2024, (pp. 35-45)
ISSN: 2588-7327
eISSN: 2588-7335

Real Evaluation of the Economic Parameters of a Solar Power Plant in Chaharmahal and Bakhtiari Province

Abbas Jamshidi Gahrouei[1*], Mojtaba Falah[2]

[1] Master of Power Electricity Distribution Company of Chaharmahal and Bakhtiari Province, Shahrekord, Iran.

[2] Master of Accounting, Electricity Distribution Company of Chaharmahal and Bakhtiari Province, Shahrekord, Iran.

Received: 30-May-2024, Revised: 02-Sep-2024, Accepted: 07-Sep-2024.

Abstract

Solar energy is one of the most important types of renewable energy in Iran. Solar systems are more acceptable in Iran due to their availability. There are development models and software for the purpose of economic calculations, but one should choose a model that, in addition, does not have limitations in solar system models whose results are not related to accurate and large tens. Also, due to the complexity of the results of some software (such as Homer), the analysis of these results requires special knowledge and expertise. The selected model must be in accordance with the specific needs of the project and be customized with unique conditions. Therefore, the above items can be counted as the difference between the selected model for solar economy calculations in this article with previous studies and relevant software. In this article, the economic indicators of a 400 Kw power plant in Iran are discussed. Regarding the investments in this sector, we have examined all the costs of the construction of the power plant and we evaluate and make economic calculations using the main analysis and profit analysis techniques. Computer results have been evaluated with 25% and 30% discount and 40% inflation. The capital return rate of this power plant is 25.09% and the payback period of this power plant is 9 years. NPV with a 25% discount in the ninth year is 845.35 million Rials and with a 30% discount rate, it is 26809.88 million Rials. Also, the internal rate of return is calculated as IRR = 25.08%.

Keywords: Economic Evaluation, Net Present Value (NPV), Renewable Energy, Photovoltaic.

***Corresponding Authors Email:** Abbas.jamshidi133@gmail.com

1. INTRODUCTION

Traditional energy sources and fossil fuels with population increase and unprincipled exploitation of these resources have forced mankind to use renewable resources [1]. Although many alternative energy sources are available, due to easy access, free maintenance, and zero pollution, many investors and countries of the world have been attracted to use of solar energy in their project plans [2]. Developing countries are faced with the challenge of facing high energy demand [3,4]. These countries are required to achieve the goals in all UN policies by 2030 [5]. Investors are always looking for ways to maximize their investment since the energy economy is essential for the investor, so the analysis of economic parameters is very necessary. Economic analysis requires the calculation of all costs, benefits, and related cash flows. Therefore, investors evaluate sustainability and feasibility conditions for investing in photovoltaic systems by using various key economic performance indicators such as internal rate of return, VPV, investment return period (IRR), LCOE, leveled energy cost measure, etc. [6,7,8]. A lot of research has been done in the field of economic evaluation of solar power plants. Most of the results are based on Homer software. For example, in 2022, a study was conducted on the technical-economic analysis of the renewable energy system with Homer software, and the cost of energy (COE) decreased from 0.060 dollars per kilowatt hour to 0.0446 dollars per kilowatt hour [9].
In 2020, V. Motjoadi conducted an economic analysis of a Pv-based microgrid using Homer software, and the research result was NPC=1.48 and COE=$1330 [10]. In 2021, a study was conducted on the economic analysis of the Pv-based RE hybrid system. Researchers calculated COE using Homer software. the results indicate the cost-effectiveness of the proposed system and COE=0.214 dollars per kilowatt hour [11].

A study on comparative economic analysis of various types of hybrid systems in 2024 has been conducted. Using Homer software, the researchers calculated the net present cost of various hybrid systems. The net cost is 1.5368 and the cost of energy (COE) is 0.155 dollars per kilowatt hour [12].

As seen in the above studies, in order to evaluate the economic parameters of the solar power plant with different software and algorithms, they do not consider all aspects of the costs related to the power plant. Considering the importance of fixed and variable costs in the calculation and economic evaluation of the power plant, the aforementioned study has focused on all costs and calculating parameters based on the real inflation rate of Iran. This article is a complete reference for the design and economic evaluation of the solar power plant. The structure of the article is as follows: in the first part, the research method and important economic projects of the solar power plant will be discussed, and in the second part, the design of the 400KW solar power plant will be discussed, and in the third part, the calculation of the costs of the construction of power plants and sectors will be discussed. It will come to an end. We analyze data and draw conclusions.

2. RESEARCH METHODOLOGY

Engineering economics includes a set of

methods and techniques that are used to evaluate, analyze, and optimize engineering projects and decisions. The revenge of engineering economics methods is dependent on factors that can be different depending on the nature of the project, the goals of the organization, and the existing constraints. Criteria and criteria for choosing the appropriate methods of engineering economics can include the type and complexity of the project, the purpose and objectives of the project, the cost and time required, the financial and economic scale of the project, and the sustainability and long-term effects of the project. Some calculation methods of engineering economy are:

- Net Present Value (NPV)
- Internal rate of return (IRR)
- Benefit-cost ratio (B/C)
- Breakeven Point – BEP
- Inflation

2.1. Net Present Value (NPV) Measure

Net Present Value (NPV) is the difference between the present value of cash inflows and the present value of cash outflows over a specified period of time. This criterion tries to find a balance between investment payments and income from investment implementation by considering the time adjustment of money. The evaluation of this balance is compared to the standard interest rate that the plan management has determined in advance for investment and use of funds. This interest is called "minimum absorbable interest" or "cost of capital".

Considering that the main goal of this project is to increase profitability and also due to the uncertainty of the project that requires sensitivity analysis and risk management, this method has been used.

$$PV = \sum_{t=0}^{n} \frac{CF_t}{(1+i)^t} = CF_0 + \sum_{t=0}^{n} \frac{CF_1}{(1+i)^1} + \ldots + \sum_{t=0}^{n} \frac{CF_n}{(1+i)^n} \quad (1)$$

In the above relationship, CF0 is the initial investment, CFt is the cash received or paid at time t, and i is the discount rate.

IF: NPV=> Project selection

$IF: NPV = 0$=>Indifference to choosing or not choosing the project

$IF: NPV < 0$=> Failure to select a project [13].

2.2. Internal Rate of Return (IRR)

IRR is the rate that makes the project's net present value (NPV) equal to zero. In other words, the internal rate of return can be considered as the maximum interest rate that the plan can pay. It should not be financially harmful. According to the absorption rate (MARR), it is possible to decide on the economic viability of the project as follows.

IRR $> MARR \Rightarrow$ The project has economic justification.

IRR $< MARR \Rightarrow$ The project has no economic justification

IRR = MARR=> We are indifferent to the implementation of the project [14]

$$\sum_{t=0}^{n} \frac{CFt}{(1+\mathrm{IRR})^t} = 0 \text{ و } i = IRR \quad (2)$$

2.3. Benefit-Cost Ratio (B/C)

One of the economic indicators for project evaluation is the ratio of benefits to costs or benefits to costs (B/C). This ratio is equal to the result of dividing the present value of the project's benefits by the present value of its costs. If this ratio is greater than one, it means that the plan is economic, and if it is smaller than one, it means that the plan is uneconomical [15].

Due to the fact that the project includes social, environmental, and public sector goals and it is necessary to compare several different options in order to achieve the best answer, we use this method in the economic analysis of the project.

$$\text{Benefit} - \text{costratio} = \frac{\text{Pv of Expected Benefit}}{\text{Pv of Expected Costs}} \quad (3)$$

2.4. Breakeven Point – BEP

The break-even point is the point where total sales equal costs. That is, at that point, the net profit of the company becomes zero. In fact, it is a term that shows the relationship between the amount of production of an economic project, in which the amount of expenses is equal to the income, and the project at this level of production neither gains nor loses. If the production is more than the break-even point, the project will be profitable, otherwise it will be unprofitable.

$$\text{Breakeven Point} - \text{BEP} = \frac{F}{P-V} \quad (4)$$

In the above formula F is fixed costs, P is sales price and, V is variable costs.

The percentage of sales the Breakeven Point – BEP is calculated as follows:

$$\text{BEP} = \frac{Fixed\ cost}{Total\ sales - Variable\ cost} \quad (5)$$

Considering that the project has fixed and variable costs and the management of these costs leads to profitability, therefore this method is used in the economic analysis of the project.

2.5. Inflation

Inflation means a continuous increase in the general price level of goods and services in a society for a certain period of time. To measure the inflation rate, one year is considered as the base year. They measure the price increase according to it. The general formula for calculating inflation is as follows:

$$\text{T} = \frac{\text{CPI}_\text{p} - \text{CPI}_\text{b}}{\text{CPI}_\text{b}} \quad (6)$$

In the formula, CPIp is the index of goods and services at the current time and CPIb is the CPI index of the base period. To calculate the CPI index, Laspierre's formula is used as follows:

$$I_{t,0} = \frac{\sum_{i=1}^{n} p_{t,i} q_{0,i}}{\sum_{i=1}^{n} p_{0,i} q_{0,i}} \times 100 \quad (7)$$

Pt is the price of the desired product at time t and P0 and q0 are the price of the desired product at time zero or the base year [17].

Quantitative inflation has properties that help improve transparency, measurability, and economic comparability. These features help investors make their financial decisions and monetary policies in order to choose the right project for profitable investment. Therefore, in this project, we consider inflation quantitatively.

3. INVESTMENT COSTS

3.1. Fixed Cost

Fixed costs do not change as service increases or decreases. The independence of the fixed cost from the output of the production units is the main and fundamental condition of the fixed cost. The list of fixed investment costs is as follows:

- The cost of obtaining permits
- The cost of machinery and facilities
- Purchase of land
- Provision of office equipment
- Building construction and landscaping

-Wage cost [18].

3.2. Variable Cost

Unlike fixed costs, variable costs depend on output. That is, the higher the output of a project, the higher the variable costs.

The list of variable costs is as follows:

- The cost of purchasing raw materials and equipment
- Cost of energy consumption
- Maintenance cost

The formula for calculating fixed and variable costs is as follows:

$$C_T = (F_c)_T + (V_c)_T$$

where (Fc)T is the fixed cost, (Vc)T is the variable cost, and CT is the total cost [19].

Table 1. ***Power plant equipment under study.***

row	Type of machinery and equipment	Number	Unit price (Rial)	Price (million Rial)
1	30 kW polycrystalline solar pane	14	5500000000	77000
2	structure	1	8000000000	8000
3	DC, Ac electrical panel	1	6400000000	6400
4	Solar panel connector	14	280000000	3920
5	Inverter 1 MW	1	6500000000	6500
6	Surge protector	1	500000000	500
7	Meter with CT	1	850000000	850
8	DC high voltage ground power cable	100	9000000	900
9	Medium voltage ground power cable AC	100	7000000	700
10	lightning rod	1	30000000	30
11	copper earth wire	10	1900000	19
12	copper plate	14000	2970000	41580
13	Other equipment	1	900000000	900
14	Installation cost (10%)	1	13898000000	13898
	Total			161197

*https://www.satba.gov.ir (1403 price list)

Variable costs are of particular importance in the economic calculations of solar power plants. These costs have a decisive role in the economic analysis and decision to invest in these types of power plants. These costs have a direct effect on the calculation of Breakeven Point -BEP, Internal rate of return (IRR), impact on profitability and impact on the final price. Therefore, it is very important to consider these costs in the economic calculations of the solar power plant.

4. PHOTOVOLTAIC SYSTEM DESIGN

It will take 5000 square meters of land to build this photovoltaic system. The solar panels are connected in series and according to the calculations, 14 polycrystalline solar panels of 30 kW and one Iforty of 1 MW are needed. The equipment of the 400 kW photovoltaic system is as described in Table 1.

5. CALCULATION OF POWER PLANT CONSTRUCTION COSTS

5.1. Landscaping

Table 2. ***Cost of Landscaping.***

Description	Area (m^2)	unit price (Rial)	total cost Million Rial
Leveling	5000	1500000	7500
Fencing	400	4500000	1800
Create an access road	1000	4000000	4000
Total			13300

*https://www.mrud.ir/ (1403 price list)

5.2. Construction

Table 3. ***Cost of Construction.***

Description	building type	Area (m^2)	unit price (Rial)	total cost Million Rial
Facilities	To maintain the equipment	30	100000000	3000
Guarding	Guard building for protection	20	100000000	2000
Total			5000	

*https://www.mporg.ir , *https://www.mrud.ir/ (1403 price list)

5.3. Raw Material

Table 4. ***Cost Raw material.***

name of the raw materials	Annual consumption	unit	Unit price (Rial)	Total cost Million (Rial)
Consumables and spare parts	1	-	1000000000	1000
Other consumables	1	-	100000000	100
Total				1100

*https://www.satba.gov.ir, https://www.mporg.ir/(1403 price list)

Table 5. ***Cost of repairs and maintenance.***

Description	Asset value (million rials)	Percent	Annual maintenance cost (Million rial)
Landscaping	13300	2	266
Building	5000	2	100
Equipment	161197	5	8059.85
Facilities	500	10	50
Means of transportation	0	10	0
Total			8475.85

* https://www.mporg.ir/

Table 6. ***Cost of repairs and maintenance.***

Description	Amount (Million Rial)
Land	0
Landscaping	13300
Building	5000
Equipment	161197
Facilities	500
Means of transportation	0
office supplies	359.994
Unpredicted (1% of items above)	9017.8497
Million Rial in total	189374.84

Table 7. ***Cost before operation.***

Description	Amount (Million Rial)
Costs of preparing a plan, consulting for obtaining a license, the right to register bank contracts (2% of the capital cost)	3787.50
Total	3787.50

5.4. Estimating the cost of repairs and maintenance

Maintenance costs include: landscaping, building, machinery, and facilities. According to the lifespan and functionality of each of the mentioned items, we consider a percentage of the total costs of each for maintenance on an annual basis.

5.5. Cost Before Operation

The pre-operation cost includes 2% of the capital cost, which is calculated as follows:

Pre-operation costs + capital cost = fixed capital
3787.50+189374.84=193162.34

5.6. Working Capital Estimation

The cost of working capital includes the purchase of raw materials, which is expressed as follows:

million rials of capital in circulation in the first year of operation = 458.33 * %70 = 320.83

5.7. Partnership with the Bank

Considering that there is support for investors in the public and government sectors, therefore, we consider the percentage of investor and government sector participation similar to the instructions of the Renewable Energy and Electricity Utilization Organization (Satba) as follows:

Table 8. ***Working capital estimation.***

Title	Description	Amount (Million Rial)
raw materials	One month of raw materials	458.33
Total		458.33

Table 9. ***Partnership with the bank.***

Description	Applicant's share		Banking facilities		Total (Million Rial)
	Amount	Percent	Amount	Percent	
fixed capital	19316.23	10	173846.11	90	193162.34
capital in circulation	45.83	10	412.50	90	458.33
Total investment	19362.07		174258.61		193620.67

Table 10. ***Depreciation cost after implementation.***

Description	Asset value (million rial)	Percent	annual depreciation cost (Million Rial)
Landscaping	13300	5	665
Building	5000	5	250
Equipment	161197	10	16119.7
Facilities	500	10	50
Means of transportation	0	10	0
office supplies	359.994	20	71.9988
unexpected	9017.8497	0	0
Total			17156.70

5.9. Annual production cost

Table 11. ***Annual production cost.***

Description	Amount
Cost of raw materials	1100
Energy cost (water, electricity, fuel)	0
Cost of repairs and maintenance	8475.85
Cost of salaries and wages	0
Depreciation cost	17156.70
Unforeseen cost of production (1% of high items)	267.33
Administrative and sales fee (1% of above items)	270
Cost of financial facilities (5% of the fixed capital loan amount)	8692.31
Depreciation cost before operation (10% of the costs before operation)	378.75
Training and insurance fee (2% of sales)	408.80
Total	36749.73

5.8. Depreciation Cost After Implementation

Due to the fact that the cost is evenly and equally distributed during its useful life and a certain amount of the cost of the asset is calculated as depreciation every year, it can be said that we consider depreciation linearly.

6. CONCLUSION

The main goal of this article is the economic analysis of a 400 KW power plant in Chaharmahal and Bakhtiari province. According to the calculations, the NPV of the power plant has been positive since the ninth year and it can be said that it has an economic value. Also, according to the calculation of IRR (IRR = 25.08%), this value can be justified and indicates that the power plant has economic justification. According to the table of current costs of the power plant over 10 years and the amount of profit and loss, the investment return period is estimated to be nine years, and the amount of profit over 10 years is 348,812.341 Rials.

REFERENCES

[1] T. Hosseinzadeh, M. and Afshar, R., 2006, Renewable Energy, Geological Journal, Vol. 12, No. 2, PP. 53-45.

[2] Y. El Mghouchi, A. El Bouardi, Z. Choulli, T. Ajzoul, Models for obtaining the daily direct, diffuse and global solar radiations, Renewable and Sustainable Energy Reviews, Volume 56,2016, Pages 87-99.

[3] Mohd Zainal Abidin Ab Kadir,

Yaaseen Rafeeu, Nor Mariah Adam, Prospective scenarios for the full solar energy development in Malaysia, Renewable and Sustainable Energy Reviews, Volume 14, Issue 9, 2010, Pages 3023-3031.

[4] Roozbeh Kardooni, Sumiani Binti Yusoff, Fatimah Binti Kari, Renewable energy technology acceptance in Peninsular Malaysia, Energy Policy, Volume 88, 2016, Pages 1-10.

[5] Salsabila Ahmad, Mohd Zainal Abidin Ab Kadir, Suhaidi Shafie, perspective of the renewable energy development in Malaysia, Renewable and Sustainable Energy Reviews, Volume 15, Issue 2, 2011,Pages 897-904.

[6] Pedro M.S. Carvalho, Pedro F. Correia, Luis A.F.M. Ferreira Distributed reactive power generation control for voltage rise mitigation in distribution networks IEEE Trans. Power Syst., 23 (2) (2008), pp. 766-772.

[7] Wei Fu Su, Shyh Jier Huang, Chin E. Lin Economic analysis for demand-side hybrid photovoltaic and battery energy storage system IEEE Trans. Ind. Appl., 37 (1) (2001), pp. 171-177.

[8] E. A. Setiawan and F. Yuliani, “Analysis of Solar Photovoltaic Utilization in Industrial Sector for Improving Competitiveness in the Smartgrid.

[9] Halabi, 1L. M., Mekhilef, S., Olatomiwa, L., & Hazelton, J. (2017). Performance analysis of hybrid PV/diesel/battery system using HOMER: A case study Sabah, Malaysia. Energy Conversion and Management, 144(2), 322–339. https://doi.org/10.1016/j.enconman.2017.04.070.

[10] V. Motjoadi, K. E. Adetunji and P. Meera K. Joseph, "Planning of a sustainable microgrid system using HOMER software," *2020 Conference on Information Communications Technology and Society (ICTAS)*, Durban, South Africa, 2020, pp. 1-5, doi: 10.1109/ICTAS47918.2020.233986.

[11] Vendoti S, Muralidhar M, Kiranmayi R. Techno-economic analysis of off-grid solar/wind/biogas/biomass/fuel cell/battery system for electrification in a cluster of villages by HOMER software. Environment, Development and Sustainability. 2021 Jan;23(1):351-72.

[12] Mansoor Urf Manoo, Faheemullah Shaikh, Laveet Kumar, Müslüm Arıcı, Comparative techno-economic analysis of various stand-alone and grid connected (solar/wind/fuel cell) renewable energy systems, International Journal of Hydrogen Energy, Volume 52, Part A, 2024, Pages 397-414.

[13] Gu, Y., et al., Techno-economic analysis of a solar photovoltaic/thermal (PV/T) concentrator for building application in Sweden using Monte Carlo method, Energy Conversion and Management, 165, 2018, 8-24.

[14] CBI. Available from: https://cbi.ir/default_en.aspx.

[15] Ja'fari, H., Sattari, S., Mashayekhi, M., Energy efficiency in equipment and installation systems, 2011.

[16] Ramos, A., et al., Hybrid photovoltaic-thermal solar systems for combined heating, cooling and power provision in the urban environment, Energy Conversion and Management, 150, 2017, 838-850.

[17] Chandrasekar. B, Tara. C. Kandpal. (2010). "An Opinion Survey Based Assessment of Renewable Energy Technology Development in India".Renewable and Sustainable EnergyReviews (11): 688-701.

[18] McEachern, William (2012). Economics: A Contemporary Introduction. Mason, Ohio: South-Western Cengage Learning. p. 158. ISBN 0-538-45374-5.

[19] Schwartz, Robert (2010). Micro Markets: A Market Structure Approach to Microeconomic Analysis. Hoboken, New Jersey: John Wiley & Sons, 2010. p. 202. ISBN 0-470-44765-6.

Signal Processing and Renewable Energy
September 2024, (pp. 47-62)
ISSN: 2588-7327
eISSN: 2588-7335

A Review of Power Control Methods for Load Balancing for Microgrids with Uncontrollable Renewable Energy Sources

Hadi Ahmadi Nezhad [1], Mahdiyeh Eslami [*1], Mehdi Jafari Shahbazzadeh [1]

[1] Department of Electrical Engineering, Kerman branch, Islamic Azad University, Kerman, Iran.

Received: 06-Jun-2024, Revised: 26-Aug-2024, Accepted: 31-Aug-2024.

Abstract

This paper addresses the growing energy demand by exploring the realm of microgrids (MGs) and their crucial role in modernizing the conventional grid (CG). As energy needs continue to escalate, the CG has integrated advanced communication technologies, including sensors, demand response, energy storage systems, and electric vehicle integration. MGs have emerged as a viable solution to ensure local energy stability and reliability within low or medium voltage distribution systems. They achieve this by efficiently managing power exchanges between the primary grid, locally distributed generators (DGs), and consumers. This article provides an overview of microgrids, explaining their operational principles and examining various energy management methodologies. At the core of microgrid control strategies lies the energy management system (EMS), which orchestrates the interaction between different energy resources (CG, DG, ESS, and EVs) and loads, ultimately enhancing utility profitability. The paper systematically categorizes EMS design methodologies based on their structural attributes, control mechanisms, and underlying techniques.

Keywords: Microgrid, Excess Power, Frequency Control, Average Power.

1. INTRODUCTION

The rapid adoption of renewable energy technologies is transforming the global energy sector [1,2,3]. This trend is evident not only in large-scale utility and commercial applications but also in residential settings [4]. While the importance of incorporating renewable energy sources into commercial-scale operations is well-recognized, this article aims to shift its focus to a specific area—the integration of renewable energy sources within microgrid systems.

*Corresponding Authors Email: m.eslami@iauk.ac.ir

In the context of designing, upgrading, or expanding microgrid systems, a range of challenges emerge. One of the key challenges discussed in this article is the complex interaction of various brand components within microgrid configurations.

When designing a microgrid system that uses components from a single supplier [5], the inherent compatibility of these components typically allows for smooth operation, reducing the likelihood of complications [6,7,8]. However, the situation becomes significantly more complex when components from different brands are integrated into the same system [9,10,11]. The complexities of interoperability arise when these components may not inherently communicate with each other or experience communication issues, leading to a web of complications [12,13]. For example, battery inverters may communicate effectively with an off-grid photovoltaic inverter, but a different brand of grid-tied inverter may remain isolated and fail to establish communication. In this scenario, the microgrid system is controlled by a battery inverter as its master generating unit, which manages voltage, frequency, demand, and supply. The disconnection of the grid-tied inverter, along with its unique characteristics, leads to power balance issues within the system [14, 15, 16].

Addressing the power balance issue requires a strategic approach to utilizing surplus power, as it is crucial for resolving the existing power imbalance [17]. While several well-established solutions exist for managing excess power in microgrid systems—such as dump loads, vehicle-to-grid (V2G) and grid-to-vehicle (G2V) systems, hydrogen storage, batteries, scheduling, and pumped storage—many of these solutions have their limitations [18,19,20]. These limitations can include issues related to timing, complexity of implementation, and effects on stored energy levels. A detailed examination of these approaches for utilizing excess power is provided in Table 1.

Amid the evolving landscape of power utilization strategies, a significant innovation has emerged in the form of the Variable Average Power Load (VAPL) device

Table 1. ***Excess power utilization options.***

Excess Power Utilization Option	Reference	Drawback
Heat/thermal storage	[2,3,4,5]	Excess power is used in a fixed manner, which leads to the discharge of the microgrid system's batteries.
Pump storage	[6,7,8,9]	It is challenging to implement at both commercial and residential scales.
Scheduling	[10,11,12,13,14,15,16]	Using excess power comes at the expense of consumer comfort.
V2G/G2V; fuel cell	[17,18,19,20,21,22]	Using excess power in a fixed manner only temporarily addresses the issue, as it does not increase the accumulated energy level in the microgrid system.
Dump load	[23,24,25]	Excess power is used in a fixed manner, which leads to the discharge of the microgrid system's batteries.
Inverter/system control via communication	[26,27,28,29,30]	Complex to implement across various system designs, making it impractical to develop a plug-and-play solution.

[21,22,23,24]. This device effectively manages the dynamic use of excess power within microgrid configurations while preserving stored energy and ensuring consumer comfort [25,26,27,28]. Specifically designed for microgrid systems that incorporate non-controllable inverters and primarily rely on renewable energy, the main goal of this study is to examine power control methodologies for the VAPL device [29]. The study also aims to provide researchers with insights to select the most suitable control approach for managing excess power [30]. A unique aspect of this article is its thorough review of optimal average power control methods for the innovative VAPL device—a novel solution that currently lacks comparable alternatives in the existing market. The VAPL device operates based on a distinctive principle, adjusting its load rate in sync with the fluctuations of excess power within the microgrid [24,25].

In the subsequent sections, this article explores average power control methods in Section 2. It then conducts a comparative analysis of power control strategies in Section 3. Finally, Section 4 offers a thorough examination and discussion of the findings, presenting a comprehensive synthesis that encompasses the entire discourse.

2. AVERAGE POWER CONTROL METHODS IN MICROGRID SYSTEMS

Microgrid systems, representative of contemporary energy ecosystems, frequently integrate various energy storage technologies, including hydrogen storage [31,32,33], batteries [34,35,36,37], supercapacitors [38], and electrochemical systems [39,40]. These technologies are designed to maintain power balance. The primary goal of these storage solutions within microgrids is to capture surplus power during periods of excess supply and to utilize it during times of increased demand. Achieving effective energy flow management typically involves the use of bi-directional inverters, which convert alternating current (AC) to direct current (DC) and vice versa, thereby facilitating storage control.

In microgrid configurations where inverters serve as the primary generating units, the system's response to power fluctuations exhibits low inertia [42,43]. This characteristic arises from the role of inverters as the main energy sources, enabling quick and significant adjustments in power output. Excess power is often detected by monitoring the frequency, as surplus power increases the virtual rotational speed of a corresponding motor, resulting in a rise in system frequency. In this context, the Variable Average Power Load (VAPL) device stands out as an innovative solution. The VAPL device's primary function involves monitoring frequency and adjusting average power at a rate that synchronizes with the frequency change. A detailed understanding of the VAPL device, encompassing its structure, operational principles, control algorithms, placement within a microgrid configuration, power electronics, and control loop schemes, is provided in Reference [44]. Although the underlying scheme remains consistent, variations arise in the control of switching devices, leading to the identification of four

distinct switching control methodologies for analysis [45].

The adjustment of average power primarily depends on changing the duty cycle, which includes the duration of load activation (on-time) and deactivation (off-time) [46]. Higher duty cycles indicate longer on-time periods compared to off-time. The duty cycle progresses through predetermined incremental steps. For example, with a non-controllable excess power limit of 10 kW and 10 predefined steps, each step represents a 1 kW adjustment in average power. If the non-controllable excess power measures at 1.1 kW, the average power load must shift to 2 kW to alleviate the excess, resulting in a battery discharge rate of 0.9 kW. Increasing the granularity of average power control steps improves the accuracy of excess power management [47].

Choosing the most effective average power control method for microgrid systems that utilize an inverter as the primary generating unit depends on several factors. First and foremost, the VAPL device must demonstrate a cost advantage over an additional inverter to ensure economic feasibility [48,49,50]. Additionally, versatility and ease of implementation are crucial, highlighting the importance of a plug-and-play design that eliminates the need for complex custom programming across different scenarios. A device that can seamlessly adapt and integrate into various system configurations is essential [51]. Moreover, the chosen method must minimize the effects on ancillary devices, including the reduction of current and voltage harmonics as well as voltage fluctuations. Only through careful selection of the most effective average power control method can the VAPL device achieve market acceptance [52].

To this end, four distinct average power control methods have emerged, each deserving of careful examination: burst control, phase delay control, pulse width modulation (PWM) [53] on the AC side, and PWM on the DC side. Each method presents unique features and challenges, requiring a thorough analysis to assess their effectiveness in microgrid systems with inverter-dominated master generating units [54]. The following exploration aims to uncover the complexities of these methodologies and clarify their potential contributions to the evolving field of microgrid energy management and optimization [55].

A key feature of the Burst method is its minimal switching losses [44], which result from its zero-crossing switching mechanism. This characteristic reduces heat generation and, in turn, decreases the cooling requirements within the power electronics loop. The Burst control method is primarily used on the AC side and can be configured for either single-phase or three-phase systems, depending on the nature of the non-controllable excess power source. In the case of three-phase configurations, three separate average power electronic loops are created, all coordinated by a single control unit [59].

In the Phase Delay control method, the duty cycle period corresponds to half of an AC sine wave cycle. This technique primarily utilizes bidirectional three-electrode AC switches (TRIACs) [45]. By intentionally delaying the activation of the AC load, this method results in reduced power consumption. The delayed switching interval

lowers the average voltage applied to the load, facilitating effective power management. However, this approach is associated with higher switching losses, which can account for up to 85% of total losses [47], leading to increased heat generation and a greater need for enhanced cooling mechanisms. Although Phase Delay control can generate harmonics [48] and may lead to voltage and current spikes, it also provides a distinct advantage. By allowing the master generating unit—typically an inverter—to quickly respond to rapid changes in power balance, the Phase Delay method can help reduce sudden voltage and current fluctuations during switching. Like the Burst and PWM methods on the AC bus, Phase Delay control requires the development of separate VAPL devices for single-phase and three-phase non-controllable excess power sources [60].

The use of Pulse Width Modulation (PWM) on an AC-side bus as an average power control method builds on its established application in inverters. The duration of a PWM duty cycle typically occupies a very small fraction of time in the kHz range. This configuration helps avoid issues related to harmonic generation and beat phenomena, especially when the number of switches is limited [49]. Changes in the duty cycle, which control the on and off times of the load, directly affect the average power output. Longer on-times compared to off-times result in higher duty cycles, leading to increased average power levels.

However, implementing PWM on an AC-side bus requires careful consideration of power quality. Soft-switching techniques [50] or additional hardware like filters may be necessary to mitigate any adverse effects. Analogous to the previous methodologies, the PWM on AC Bus approach requires tailored VAPL devices for single-phase and three-phase non-controllable excess power sources.

At the end of the range of average power control methods is PWM on the DC side of microgrid systems. This approach utilizes PWM to regulate power dissipation on a DC bus, requiring a PWM-controlled device. While the operational principle is similar to that of PWM on the AC bus, only one PWM power electronics loop is needed for either a single-phase or three-phase configuration. However, higher DC bus voltages may necessitate increased current through the switches.

Like its AC counterpart, PWM on the DC bus adjusts the duty cycle to control average power. By increasing the duty cycle and, consequently, the on-time duration, the dissipation of excess power increases. It is important to note that while PWM on the DC side offers a promising solution, there are potential concerns regarding battery aging that depend on the PWM frequency [51]. To minimize negative impacts on battery health, techniques can be employed for estimating battery aging [52]. can be employed.

Considering these distinct methodologies, the search for an optimal average power control method continues. Each approach presents distinctive characteristics and challenges that require careful evaluation, propelling the advancement of microgrid energy management toward enhanced efficiency and sustainability.

Excess power in a microgrid system is identified by measuring and monitoring frequency. When excess power is present, the virtual rotating motor spins faster, resulting in an increase in frequency. The primary objective of the VAPL device is to track frequency changes and adjust the average power accordingly. A detailed description of the VAPL device's structure, operational function, control algorithm, placement within a microgrid framework, power electronics, and control loop schemes can be found in Reference [53]. Fig. 1 illustrates the main configuration of the VAPL device's power and control loops. While the overall scheme is similar across most average power control methods, the control of the switching devices varies, and the four different switching control methods are reviewed.

3. COMPARING AVERAGE POWER CONTROL METHODS IN MICROGRID SYSTEMS

A thorough evaluation of average power control methods is crucial for determining the suitability of the Variable Average Power Load (VAPL) device for various market demands. This assessment focuses on three key factors: versatility, impact on other devices, and cost-effectiveness. The VAPL device's effectiveness as a market solution depends on its ability to meet these criteria [61].

3.1. Versatility Comparison of Power Control Methods

In the context of this article, versatility refers to the adaptability of the final VAPL device prototype across different system designs. The aim is to develop a plug-and-play solution that reduces the need for complex programming for various applications or system configurations. As a result, power control methods are assessed based on their versatility [61].

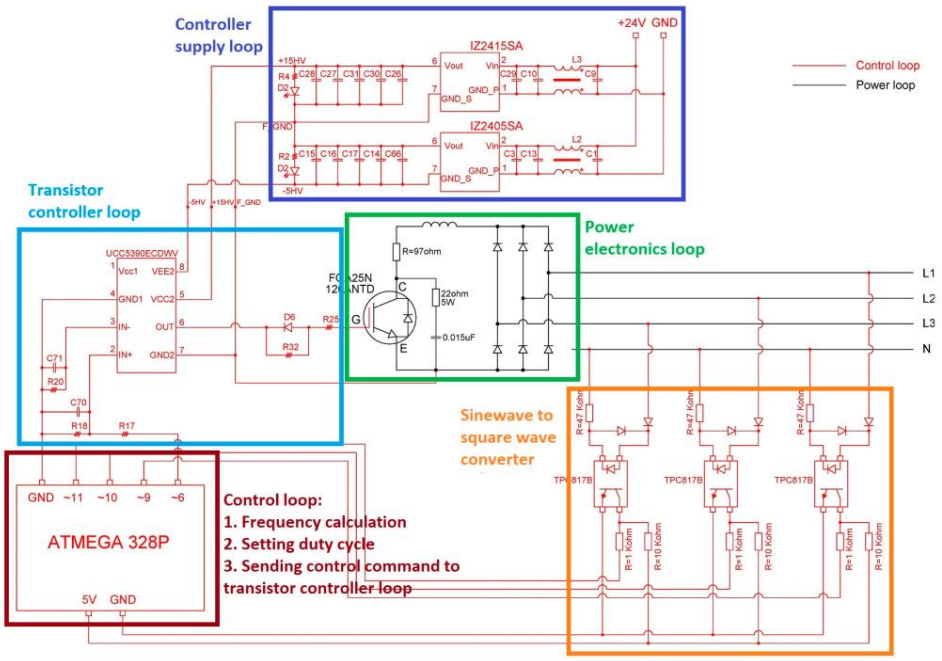

Fig. 1. The scheme of a VAPL device.

A duty cycle control loop is essential across all average power control methods. This loop determines the necessary average power and directs the average power control device accordingly. The evaluation of the required average power is based on frequency measurements within the AC bus, where excess power is detected. Therefore, each average power control method requires a connection to the AC bus to calculate the needed average power, ensuring the efficient use of excess power without jeopardizing the system's energy reserves [61].

Load activation and deactivation take place on the AC bus for the Burst control, Phase Delay, and PWM on AC Bus methods. As a result, the versatility of integrating these methods is largely comparable. Regardless of the selected approach, a VAPL device must be connected to the AC bus. Furthermore, the calculation of the duty cycle is closely tied to this connection. This relationship facilitates streamlined connections within the VAPL device itself, simplifying the integration process. The application of these methods on the AC side makes them versatile solutions suitable for various AC systems, regardless of the brand or type of inverter used [63].

In contrast, the versatility of a VAPL device controlled by the PWM on the DC Bus method is affected by several factors. Firstly, excess power detection relies on frequency measurement, necessitating an AC connection. This adds complexity to installations in various system designs. Secondly, the versatility of the PWM on the DC Bus method is limited by the varying voltage levels of battery systems. To ensure compatibility with battery systems ranging from 12 V DC to 48 V, and up to 400 V DC, separate devices may need to be developed for each voltage range. Thirdly, integration might require additional programming in cases where battery inverters and batteries communicate with each other. Finally, the transient conditions resulting from rapid load switching may affect the aging of DC bus batteries [53], necessitating the use of filters or careful selection of switching frequency. These factors collectively limit the method's versatility across different systems [64].

Given the direct influence of average power control methods on the design of the VAPL device, circuit board layout, and system integration, it is clear that the greatest versatility can be attained through the use of Burst control, Phase Delay, or PWM on AC Bus methods. These methods are inherently aligned with the AC side, offering simplified connections and broad applicability, making them ideal candidates for versatile implementation across various microgrid configurations. The duty cycle affects the on and off times of the load; specifically, longer on time than off time results in a higher duty cycle and, consequently, a greater average

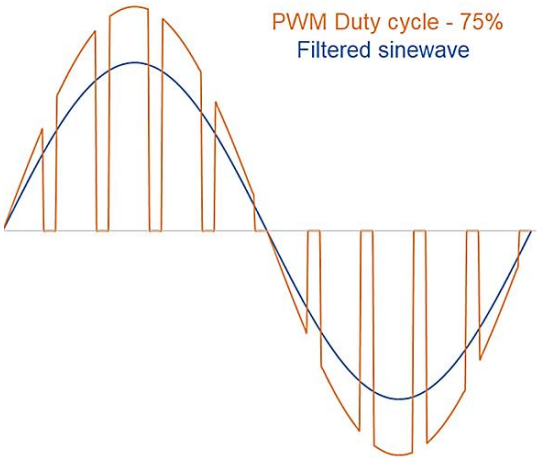

Fig. 2. PWM on AC-side bus control operation mode.

value, as illustrated in Fig. 2. To prevent the VAPL device using the PWM on the AC-side bus control method from affecting power quality, techniques like soft-switching [50] or additional hardware such as filters must be implemented. Similar to the burst and phase angle control methods, the PWM on the AC-side bus approach necessitates separate VAPL devices designed for single-phase and three-phase non-controllable excess power sources.

3.2. Not Harmful to Other Devices in a System

An experimental system was used to examine whether high-voltage switching at the peak of a sine wave leads to transient processes. The study involved assessing voltage spikes in an off-grid system caused by switching during the high-voltage phases of the sine wave.

The complete sine wave period is 20 ms; however, rapid switching at high-voltage points of the sine wave generates transient processes. These transient periods can last up to 1.2 μs and may cause voltage spikes exceeding 200 V, which in turn can lead to current spikes. As a result, methods such as phase delay and PWM on the AC bus could produce undesirable voltage and current spikes that compromise power quality and potentially damage off-grid AC appliances.

A similar, though less severe, effect occurs with direct PWM control on a DC bus, which may affect battery aging due to transient conditions during rapid switching. To address this issue, it becomes essential to implement filters to reduce aging or to select a switching frequency that minimizes harm.

The burst control method is preferred because it generates minimal or negligible transient processes, as switching occurs near 0 V. Similarly, PWM on a DC bus produces minimal transient processes on the AC side due to its operation on the DC side. Consequently, both the burst control and PWM on DC bus methods are considered to have little or no negative impact on other devices in the system.

3.3. Cost Evaluation of Power Control Methods

To keep a VAPL device competitive, its cost must be comparable to that of a new inverter. If the price of the VAPL device is similar to that of an inverter, consumers may prefer to buy a new inverter designed for their system instead of opting for a VAPL device to address excess power issues. In such cases, the attractiveness of the VAPL device could decrease. Therefore, it is crucial to evaluate the costs of power control methods, taking into account any necessary additional components.

The Burst control method offers a significant advantage in terms of its primary cost. Because it operates near 0 V, it incurs minimal switching losses, resulting in lower heat dissipation and reduced cooling system requirements. Furthermore, it does not generate voltage or current harmonics, eliminating the need for filters or additional cooling systems. As a result, the Burst method stands out as an optimal choice for minimizing the overall cost of a VAPL device.

In contrast, the Phase Delay and PWM on AC Bus methods incur higher switching losses, requiring more robust cooling systems. Filters are necessary to mitigate voltage and current spikes. These methods

involve additional components, increasing the primary cost of the VAPL device and potentially making it comparable to the price of a new inverter. This factor may limit their market appeal.

Although the even power dissipation of the PWM on the AC Bus method appears advantageous, it generates high current and voltage harmonics that lead to significant filter costs, making it less cost-effective. The Phase Delay method, while producing lower harmonics than PWM on AC Bus, may introduce inrush voltage and current spikes. This approach might require customized filters for different systems to maintain power quality.

Direct PWM control on a DC Bus is a cost-effective solution. It evenly distributes average power, eliminates voltage fluctuations on the AC side, and prevents inrush current or voltage in the sine wave, which benefits other AC devices in the system. Although the potential increase in primary costs due to varying battery system voltage levels presents a challenge, the overall advantages of this method are significant.

In conclusion, the Burst average power control method seems to be the most suitable option, effectively balancing its effects on other appliances while keeping the primary cost low. Additionally, PWM on a DC Bus shows potential, providing controlled average power with minimal impact on overall costs.

The final method for controlling average power is PWM on the DC side of a microgrid system. Excess power can be dissipated using a PWM-controlled device on a DC bus. While the operating principle of PWM is similar to that used for the AC bus, the configuration differs due to the three-phase system compared to the DC bus. In this case, there is only one PWM power electronics loop; however, depending on the DC bus voltage, it may need to handle a higher current through the switches.

Average power control is achieved through the duty cycle, which consists of phases where the system is switched on and off, similar to the PWM method used on the AC side. The greater the excess power that needs to be dissipated, the higher the duty cycle required for the PWM, resulting in a longer on-time compared to off-time, as illustrated in Fig. 6. While PWM on the DC side may initially seem like the preferred control method, it can also contribute to battery aging, depending on the PWM frequency [51]. Battery aging can be monitored by assessing the battery's state of

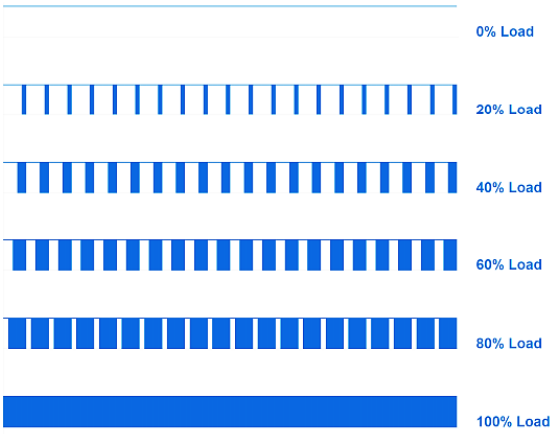

Fig. 3. PWM control on the DC-side bus operation mode. The more excess power that needs to be dissipated, the higher the duty cycle of the PWM is required to be, and the longer the switched-on time is compared to the switched-off time, as in the example given in the figure.

health [52] to mitigate the negative effects of VAPL devices on batteries. Consequently, it is essential to compare all proposed methods.

3.4. Summary of Comparison of Power Control Methods

The evaluation of average power control methods provided valuable insights, which are summarized in Table 2. While the PWM on AC Bus method offers uniform power dissipation, it produces significant current and voltage harmonics, leading to higher filter costs. The Phase Delay method may result in voltage fluctuations and generate current and voltage harmonics, requiring filters tailored to specific systems. In contrast, direct PWM control on a DC Bus stands out as a favorable solution, as it evenly distributes power without adversely affecting other AC devices.

The selection process took into account the versatility, cost-effectiveness, and impact of the VAPL device on other devices. After balancing these criteria, the Burst average power control method emerged as the optimal choice. It offers a versatile and straightforward solution that meets all requirements without the need for additional components.

4. CONCLUSIONS

In microgrid systems, excess power can cause frequency increases. The VAPL device activates when the frequency surpasses a predetermined threshold, using non-controllable excess power at the necessary rate. The VAPL algorithm adapts power utilization to align with fluctuations in excess power, ensuring the maintenance of energy reserves and electricity quality. For optimal performance, the VAPL device adjusts power incrementally, requiring different models for one-phase and three-phase sources, with the exception of PWM on a DC bus.

The comparison results suggest that the burst control method is the most suitable for VAPL. While it may cause voltage fluctuations in systems with a rotating master generator, it is less problematic in inverter-based systems. However, further validation through simulations and real-world testing is necessary.

Microgrid systems with non-controllable generators, particularly unpredictable renewable sources, face excess power issues that affect frequency and stability. The VAPL device, equipped with four control methods (burst, phase-angle, PWM on an AC bus, or PWM on a DC bus), offers a solution to this problem.

Table 2. Comparison of average power control methods.

Power Control Method	Versatile	Cost-Efficient	No Filtering Needed
Burst	Yes	Yes	Yes
Phase delay	Yes	No	No
PWM AC bus	Yes	No	No
PWM DC bus	No	Yes	Yes

Considering the requirements, context, and capabilities of the VAPL device, burst control emerges as the most appropriate method for regulating average power in microgrids with non-controllable excess power sources. It minimizes costs and the impact on the system while effectively utilizing excess power. Further research should involve simulations and real-world prototypes to confirm its effectiveness and viability in practical applications.

Integrating renewable energy sources into microgrid systems poses a complex challenge due to the intricate interactions among various components. The Variable Average Power Load (VAPL) device offers an innovative solution for managing the dynamic use of excess power in microgrid configurations while preserving the integrity of stored energy and ensuring consumer comfort. The primary function of the VAPL device is to monitor frequency and adjust average power in sync with frequency changes. Four distinct average power control methods have emerged, each with its own unique characteristics and challenges: Burst control, Phase Delay control, Pulse Width Modulation (PWM) on the AC side, and PWM on the DC side. A thorough evaluation of these methods is crucial for assessing their suitability for various market demands. This assessment concentrates on three key factors: versatility, impact on other devices, and cost-effectiveness. The Burst, Phase Delay, and PWM on AC Bus methods demonstrate greater versatility because they are compatible with the AC side and feature simplified connections, making them strong candidates for implementation across diverse system designs. In contrast, the PWM on the DC Bus method is limited by fluctuations in battery system voltage levels, necessitating separate devices for each voltage range and additional programming. The versatility and adaptability of the VAPL device are vital for its success in the market. Consequently, choosing the most suitable average power control method requires balancing these attributes with considerations of cost-effectiveness and ease of implementation.

REFERENCES

[1] Zelba, M.; Deveikis, T.; Barakauskas, J.; Baronas, A.; Gudzius, S.; Jonaitis, A.; Giannakis, A. A Grid-Tied Inverter with Renewable Energy Source Integration in an Off-Grid System with a Functional Experimental Prototype. Sustainability 2022, 14, 13110.

[2] E. Hernández-Mayoral et al., "A comprehensive review on power-quality issues, optimization techniques, and control strategies of microgrid based on renewable energy sources," Sustainability, vol. 15, no. 12, p. 9847, 2023.

[3] S. Ahmad, M. Shafiullah, C. B. Ahmed, and M. Alowaifeer, "A review of microgrid energy management and control strategies," IEEE Access, vol. 11, pp. 21729-21757, 2023.

[4] Tahir, M.F.; Haoyong, C.; Mehmood, K.; Ali, N.; Bhutto, J.A. Integrated Energy System Modeling of China for 2020 by Incorporating Demand Response, Heat Pump and Thermal Storage. IEEE Access 2019, 7, 40095–40108.

[5] D. Saha, N. Bazmohammadi, J. C. Vasquez, and J. M. Guerrero, "Multiple microgrids: A review of architectures and operation and control strategies," Energies, vol. 16, no. 2, p. 600, 2023.

[6] Nirmal, M.C.M.; Sruthi, M.; Jayaprakash, P. Control of a Pumped Hydro Storage Power Plant Supported Solar PV Generation System for Grid-Side Energy Management. In Proceedings of the 2021 IEEE 4th International Conference on Computing, Power and Communication Technologies (GUCON), Kuala Lumpur, Malaysia, 24–26 September 2021.

[7] Abdalla, S.M.; Saad, S.M.; El Naily, N.; Bukra, O.A. Seawater Pumped Hydro Energy Storage in Libya Part I: Location, Design and Calculations. In Proceedings of the 2021 IEEE 1st International Maghreb Meeting of the Conference on Sciences and Techniques of Automatic Control and Computer Engineering MI-STA, Tripoli, Libya, 25–27 May 2021.

[8] H. Shah, J. Chakravorty, and N. G. Chothani, "Protection challenges and mitigation techniques of power grid integrated to renewable energy sources: A review," Energy Sources, Part A: Recovery, Utilization, and Environmental Effects, vol. 45, no. 2, pp. 4195-4210, 2023.

[9] Tahir, M.F.; Haoyong, C.; Khan, A.; Javed, M.S.; Laraik, N.A.; Mehmood, K. Optimizing Size of Variable Renewable Energy Sources by Incorporating Energy Storage and Demand Response. IEEE Access 2019, 7, 103115–103126.

[10] Nayanatara, C.; Divya, S.; Mahalakshmi, E. Micro-Grid Management Strategy with the Integration of Renewable Energy Using IoT. In Proceedings of the 2018 International Conference on Computation of Power, Energy, Information and Communication (ICCPEIC), Chennai, India, 28–29 March 2018.

[11] Bao, Z.; Qiu, W.; Wu, L.; Zhai, F.; Xu, W.; Li, B.; Li, Z. Optimal Multi-Timescale Demand Side Scheduling Considering Dynamic Scenarios of Electricity Demand. IEEE Trans. Smart Grid 2018, 10, 2428–2439.

[12] Karapetyan, A.; Khonji, M.; Chau, S.C.-K.; Elbassioni, K.; Zeineldin, H.H.; El-Fouly, T.H.; Al-Durra, A. A Competitive Scheduling Algorithm for Online Demand Response in Islanded Microgrids. IEEE Trans. Power Syst. 2020, 36, 3430–3440.

[13] M. W. Khan, G. Li, K. Wang, M. Numan, L. Xiong, and M. A. Khan, "Optimal control and communication strategies in multi-energy generation grid," IEEE Communications Surveys & Tutorials, 2023.

[14] G. R. Goyal and S. Vadhera, "Smart home appliances' scheduling by two-stage optimization with real-time price model," Electric Power Components and Systems, vol. 51, no. 6, pp. 604-618, 2023.

[15] Z. Luo, J. Peng, X. Zhang, H. Jiang, R. Yin, Y. Tan, and M. Lv, "Optimal Scheduling of Smart Home Energy Systems: A User-Friendly and

Adaptive Home Intelligent Agent with Self-Learning Capability," Advances in Applied Energy, p. 100182, 2024.

[16] Latif, A.; Paul, M.; Das, D.C.; Hussain, S.M.S.; Ustun, T.S. Price Based Demand Response for Optimal Frequency Stabilization in ORC Solar Thermal Based Isolated Hybrid Microgrid under Salp Swarm Technique. Electronics 2020, 9, 2209.

[17] Sanjari, M.J.; Karami, H.; Gooi, H.B. Analytical Rule-Based Approach to Online Optimal Control of Smart Residential Energy System. IEEE Trans. Ind. Inform. 2017, 13, 1586–1597.

[18] Huang, Q.; Jia, Q.-S.; Guan, X. Robust Scheduling of EV Charging Load With Uncertain Wind Power Integration. IEEE Trans. Smart Grid 2016, 9, 1043–1054.

[19] Patterson, M.; Macia, N.F.; Kannan, A.M. Hybrid Microgrid Model Based on Solar Photovoltaic Battery Fuel Cell System for Intermittent Load Applications. IEEE Trans. Energy Convers. 2014, 30, 359–366.

[20] T. Banerjee, J. Bravo, N. Sarunac, M. D'Agostini, and C. Romero, "Sustainable energy storage solutions for coal-fired power plants: A comparative study on the integration of liquid air energy storage and hydrogen energy storage systems," Energy Conversion and Management, vol. 310, p. 118473, 2024.

[21] Tushar, M.H.K.; Assi, C.; Maier, M.; Uddin, M.F. Smart Microgrids: Optimal Joint Scheduling for Electric Vehicles and Home Appliances. IEEE Trans. Smart Grid 2014, 5, 239–250.

[22] Singh, M.; Kumar, P.; Kar, I.; Kumar, N. A real-time smart charging station for EVs designed for V2G scenario and its coordination with renewable energy sources. In Proceedings of the 2016 IEEE Power and Energy Society General Meeting (PESGM), Boston, MA, USA, 17–21 July 2016.

[23] Arun, S.L.; Selvan, M.P. Intelligent Residential Energy Management System for Dynamic Demand Response in Smart Buildings. IEEE Syst. J. 2017, 12, 1329–1340.

[24] Arriaga, M.; Cañizares, C.A.; Kazerani, M. Renewable Energy Alternatives for Remote Communities in Northern Ontario, Canada. IEEE Trans. Sustain. Energy 2013, 4, 661–670.

[25] J. Šimunović, G. Radica, and F. Barbir, "The effect of components capacity loss on the performance of a hybrid PV/wind/battery/hydrogen stand-alone energy system," Energy conversion and management, vol. 291, p. 117314, 2023.

[26] Ustun, T.S.; Hussain, S.M.S. Standardized Communication Model for Home Energy Management System. IEEE Access 2020, 8, 180067–180075.

[27] A. Chatterjee, "Wind Power Generation for Isolated Loads with IoT-based Smart Load Controller," Journal of Fuzzy Systems and Control, vol. 2, no. 2, pp. 92-96, 2024.

[28] J. L. Monroy-Morales, R. Peña-Alzola, R. Sebastián-Fernández, D. Campos-Gaona, J. Q. Castellano, and J. L. Guardado, "Frequency control in an isolated wind-diesel hybrid system with

energy storage and an irrigation water supply system," IET Renewable Power Generation, vol. 18, no. 6, pp. 1040-1054, 2024.

[29] M. A. Hartani, H. Rezk, A. Benhammou, M. Hamouda, O. Abdelkhalek, S. Mekhilef, and A. Olabi, "Proposed frequency decoupling-based fuzzy logic control for power allocation and state-of-charge recovery of hybrid energy storage systems adopting multi-level energy management for multi-DC-microgrids," Energy, vol. 278, p. 127703, 2023.

[30] Mahmood, H.; Michaelson, D.; Jiang, J. A Power Management Strategy for PV/Battery Hybrid Systems in Islanded Microgrids. IEEE J. Emerg. Sel. Top. Power Electron. 2014, 2, 870–882.

[31] Mori, M.; Gutiérrez, M.; Casero, P. Micro-grid design and life-cycle assessment of a mountain hut's stand-alone energy system with hydrogen used for seasonal storage. Int. J. Hydrogen Energy 2021, 46, 29706–29723.

[32] Esteban, L.J.; Andrea, M.; Enrico, P.; Harm, L.; Ettore, B. Modelling and Control of a Grid-Connected RES-Hydrogen Hybrid Microgrid. Energies 2021, 14, 1540.

[33] Jose, C.M.J.; Francisca, S.M.; Jose, M.A.; Francisco, J.V.; Antonio, J.C. An Optimized Balance of Plant for a Medium-Size PEM Electrolyzer: Design, Control and Physical Implementation. Electronics 2020, 9, 871.

[34] An, S.; Wang, H.; Yuan, X. Real-Time Optimal Operation Control of Micro Energy Grid Coupling with Electricity-Thermal-Gas Considering Prosumer Characteristics. IEEE Access 2020, 8, 216566–216579.

[35] Venkatraman, K.; Reddy, B.D.; Selvan, M.P.; Moorthi, S.; Kumaresan, N.; Gounden, N.A. Online condition monitoring and power management system for standalone micro-grid using FPGAs. IET Gener. Transm. Distrib. 2016, 10, 3875–3884.

[36] Jiang, W.; Yang, C.; Liu, Z.; Liang, M.; Li, P.; Zhou, G. A Hierarchical Control Structure for Distributed Energy Storage System in DC Micro-Grid. IEEE Access 2019, 7, 128787–128795.

[37] A. M. Jasim, B. H. Jasim, V. Bureš, and P. Mikulecký, "A novel cooperative control technique for hybrid AC/DC smart microgrid converters," IEEE Access, vol. 11, pp. 2164-2181, 2023.

[38] Song, M.; Shi, J.; Liu, Y.; Xu, Y.; Hu, N.; Tang, Y.; Ren, L.; Li, J. 100 kJ/50 kW HTS SMES for Micro-Grid. IEEE Trans. Appl. Supercond. 2014, 25, 5700506.

[39] Audrius, J.; Renata, M.; Tomas, D. Dynamic model of wind power balancing in hybrid power system. Turk. J. Electr. Eng. Comput. Sci. 2017, 25, 222–234.

[40] Salim, H.M.; Nacereddine, B.-T.; Faouzi, D. Analysis of the reliability of photovoltaic-micro-wind based hybrid power system with battery storage for optimized electricity generation at Tlemcen, north west Algeria. Arch. Thermodyn. 2019, 40, 161–185.

[41] Mayo-Maldonado, J.C.; Valdez-

Resendiz, J.E.; Rosas-Caro, J.C. Power Balancing Approach for Modeling and Stabilization of DC Networks. IEEE Trans. Smart Grid 2018, 10, 4188–4200.

[42] Al Kez, D.; Foley, A.M.; Muyeen, S.M.; Morrow, D.J. Manipulation of Static and Dynamic Data Center Power Responses to Support Grid Operations. IEEE Access 2020, 8, 182078–182091.

[43] Jis, B.; Wu, H.; Li, Y. Flexible On-grid and Microgrid Control Strategy of Photovoltaic Energy Storage System Based on VSG Technology. In Proceedings of the 2021 IEEE 5th Conference on Energy Internet and Energy System Integration (EI2), Taiyuan, China, 25 February 2022.

[44] I. Jitaru, A. Savu, and C. Radoi, "EMI suppression techniques for very high efficiency and very high-power density medium power AC-DC adapters," in PCIM Asia 2023; International Exhibition and Conference for Power Electronics, Intelligent Motion, Renewable Energy and Energy Management, 2023: VDE, pp. 377-381.

[45] M. Zelba, T. Deveikis, S. Gudžius, A. Jonaitis, and A. Bandza, "Review of Power Control Methods for a Variable Average Power Load Model Designed for a Microgrid with Non-Controllable Renewable Energy Sources," Sustainability, vol. 15, no. 11, p. 9100, 2023.

[46] M. Faizal, G. Kannayeram, and A. P. Mary, "A novel power quality improved AC voltage controller for soft starting of squirrel cage induction motors," Journal of Power Electronics, pp. 1-11, 2024.

[47] He, L.; Zeng, T.; Zhang, J. The Regulation Characteristics of Bridge Modular Switched-Capacitor Ac-Ac Converter. IEEE Access 2019, 7, 147683–147693.

[48] Zhang, Y.; Ruan, X. Three-Phase AC-AC Converter with Controllable Phase and Amplitude. IEEE Trans. Ind. Electron. 2015, 62, 5689–5699.

[49] Hyeon-gyu, C.; Jung-Ik, H. Dynamic current control using synchronous pulse-width modulation for permanent magnet machines. J. Power Electron. 2020, 20, 501–510.

[50] S. Singh and S. Samanta, "Modeling and Optimal Control of Modified Pulse Width Modulation on Series Resonant-based Dual Active Bridge," IEEE Journal of Emerging and Selected Topics in Industrial Electronics, 2023.

[51] Matthias, S.; Josef, G.; Jan, E.; Markus, L. Influence of pulse width modulated auxiliary consumers on battery aging in electric vehicles. J. Energy Storage 2022, 48, 104009.

[52] Zhang, M.; Liu, Y.; Li, D.; Cui, X.; Wang, L.; Li, L.; Wang, K. Electrochemical Impedance Spectroscopy: A New Chapter in the Fast and Accurate Estimation of the State of Health for Lithium-Ion Batteries. Energies 2023, 16, 1599.

[53] Li, W.; Niimi, Y.; Orino, Y.; Hirata, S.; Kurosawa, M.K. A Frequency Synchronization Method for a Self-Oscillating PWM Signal Generator. IEEE Trans. Circuits Syst. II Express Briefs 2014, 61, 244–248.

[54] Zhang, L.; Born, R.; Zhao, X.; Gu, B.;

Lai, J.-S.; Ma, H. A Parabolic Voltage Control Strategy for Burst-Mode Converters with Constant Burst Frequency and Eliminated Audible Noise. IEEE Trans. Power Electron. 2016, 31, 8572–8580.

[55] Y.-C. Jian, K.-H. Lai, J.-W. Huang, W.-T. Yeh, and C.-H. Tsai, "A Novel Cost Effective Variable On-Time Control of Digital Boost PFC Converter in Boundary Conduction Mode," in 2023 IEEE 12th Global Conference on Consumer Electronics (GCCE), 2023: IEEE, pp. 1176-1178.

[56] F. Yang, Y. Jia, Y. Xing, and H. Wu, "Second-order Ripple Power Suppression For Single-Phase AC-DC Power Systems With Reduced Power Conversion Stage," IEEE Transactions on Transportation Electrification, 2023.

[57] Yun, S.J.; Yun, Y.K.; Kim, Y.S. A Low Flicker TRIAC Dimmable Direct AC LED Driver for Always-on LED Arrays. IEEE Access 2020, 8, 198925–198934.

[58] Kadota, M.; Shoji, H.; Hirose, H.; Hatakeyama, A.; Wada, K. A Turn-off Delay Controlled Bleeder Circuit for Single-Stage TRIAC Dimmable LED Driver with Small-Scale Implementation and Low Output Current Ripple. IEEE Trans. Power Electron. 2019, 34, 10069–10081.

[59] M. Zelba, T. Deveikis, S. Gudžius, A. Jonaitis, and A. Bandza, "Review of Power Control Methods for a Variable Average Power Load Model Designed for a Microgrid with Non-Controllable Renewable Energy Sources," Sustainability, vol. 15, no. 11, p. 9100, 2023.

[60] T. Song, Y. Zhang, F. Gao, C. Xu, and X. Zhu, "Data-driven Adaptive Negative Sequence Current Control Method for PWM Rectifier under Unbalanced Grid," IEEE Transactions on Power Electronics, 2024.

[61] Martínez-Treviño, B.A.; El Aroudi, A.; Valderrama-Blavi, H.; Cid-Pastor, A.; Vidal-Idiarte, E.; Martinez-Salamero, L. PWM Nonlinear Control with Load Power Estimation for Output Voltage Regulation of a Boost Converter with Constant Power Load. IEEE Trans. Power Electron. 2021, 36, 2143–2153.

Signal Processing and Renewable Energy
September 2024, (pp. 63-71)
ISSN: 2588-7327
eISSN: 2588-7335

Emotion Classification Using EEG Signals and Machine Learning Methods

Mehrnoosh Rezayati[1], Mohammad Adeli*[1]

[1] Department of Biomedical Engineering, Dezful Branch, Islamic Azad University, Dezful, Iran.

Received: 20-Jun-2024, Revised: 26-Aug-2024, Accepted: 27-Aug-2024.

Abstract

This paper presents a method of emotion classification from EEG signals. This method comprises four steps of pre-processing by low-pass filtering, feature extraction using the discrete wavelet transform and the Wigner–Ville distribution, dimensionality reduction using linear discriminant analysis, and classification. The k-nearest neighbors, random forests, and support vector machines were used as classification models. The results of this study showed that the features extracted by the wavelet transform and Wigner–Ville distribution led to the improvement of classification accuracy compared to other studies. In addition, the highest accuracy of 94.1% for the classification of 4 emotions was obtained using the features of the TP9 electrode and the support vector machine classifier.

Keywords: EEG, Emotion Classification, Machine Learning, Feature Extraction, Wavelet.

1. INTRODUCTION

Emotion classification using electroencephalography (EEG) is a fascinating field that has the potential to revolutionize the understanding and interpretation of human emotions. EEG is a non-invasive technique for recording the electrical activity of the brain. By analyzing the patterns of this electrical activity, researchers are able to classify different emotions and gain valuable insights into the functions of the human brain [1]. Objective evaluation and classification of our emotions are fascinating and pave the way for studying and understanding the complexities of human emotions. The potential applications of emotion classification using EEG are truly exciting [2]. For instance, emotion detection using machine learning could contribute to the understanding of mental health disorders such as anxiety and depression [3]. By analyzing the EEG patterns associated with

*Corresponding Authors Email: mohammad.adeli@iau.ac.ir

different emotional states, researchers could identify specific biomarkers that could aid in the diagnosis and treatment of these disorders [4]. This could lead to more personalized and effective interventions, ultimately improving the lives of millions of people. Brain-computer interface is another field in which emotion classification using EEG can assist [5]. For example, a smart application could detect when a user is feeling stressed or frustrated and respond by providing calming music or suggesting relaxation techniques [6]. This could greatly enhance the user experience and make technology more intuitive and responsive to our emotional needs. Furthermore, emotion classification using EEG has the potential to play a key role in the market research and advertising industry [7]. Companies could gain important information about what appeals to their target audience through the measurement of consumer's emotions in relation to various advertisements and products [8]. This could help them find more effective marketing strategies to increase sales. Additionally, it could help to identify potential issues or concerns with previous products, allowing companies to make necessary adjustments before re-launching them into the market. Emotion classification using machine learning has gained a lot of popularity in recent years [9-11]. Liu et al. (2018) classified emotion for Arousal-Valence recognition using EEG signals. This study reported that a combination of supervised and unsupervised feature dimensionality reduction methods can improve the performance of the classification model [12]. Acharya et al. (2020) reported an accuracy of 88.6 % for emotion [13]. The method proposed by Ghosh et al. (2021) obtained accuracies of 82% and 72% in a binary and a three-class emotion classification problem, respectively [14].

The rest of this paper is organized as follows: Section 2 introduces the EEG dataset and describes the proposed method including preprocessing, feature extraction, and classification. Section 3 describes the results and findings of the study. Results are discussed and compared to other studies in Section 4 and final conclusions are presented in Section 5.

2. MATERIALS AND METHODS

2.1. EEG dataset for emotions

The EEG dataset that we used for emotion classification was collected by Suhaimi et al. (2022) [15]. First, they manually selected 39 primary video stimuli with a virtual reality device that elicited the most effective emotional responses. Second, these initial video stimuli were evaluated by structurally placing each of corresponding videos into a quadrant of arousal-valence space model. Fig. 1 shows arousal-valence space model

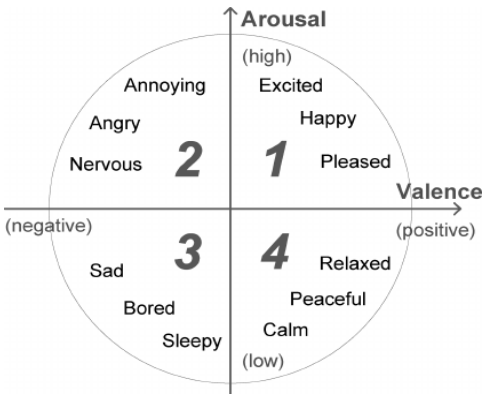

Fig. 1. Arousal-Valence model.

collected EEG signals were collected from four different channels (AF7, AF8, TP9, TP10) with the F_{pz} being the reference. The 50 Hz power line interference was removed using a notch filter. EEG signals were recorded at 0.5 s intervals by Muse Monitor at an initial sampling rate of 256 Hz with four-channel electrodes placed at AF7, AF8, TP9, and TP10.

2.2. Preprocessing

In [16], it was proposed to use frequencies from 0 to 45 Hz for emotion detection. Therefore, we used a low-pass Butterworth filter to remove frequencies above 45 Hz. The magnitude frequency response of this filter is given by Eq. (1):

$$|H(f)|^2 = \frac{1}{1 + (\frac{f}{f_c})^{2N}} \quad (1)$$

where f_c is cut-off frequency (45 Hz) and N, the order of the filter, is 8.

2.3. Feature Extraction

In this study, feature extraction was performed using the discrete wavelet transform and the Wigner-Ville distribution function.

2.3.1. Wavelet Transforms

Wavelet transform (WT) is a time-frequency domain analysis and wavelet functions are derived from a mother wavelet [17]. The continuous wavelet transform of a signal is defined as the inner product of the signal and translated and scaled versions of the mother wavelet according to Eq. (2) and Eq. (3).

$$C_x(a,b) = \int_{-\infty}^{+\infty} x(t)\psi^*_{a,b}(t)dt \quad (2)$$

$$\psi_{a,b}(t) = \frac{1}{\sqrt{|a|}}\psi\left(\frac{t-b}{a}\right), \quad a,b \in R \quad (3)$$

In Eq. (2) and (3), a and b are the scale and translation parameters, respectively, C_x denotes the wavelet coefficients, and $\psi(t)$ is the mother wavelet. In the discrete wavelet transform, signals are divided into two components using a low-pass and a high-pass filter. Then, the low-pass component is further split into two components. This could be repeated as long as needed. In this study, variance, signal wavelength, and entropy of wavelet coefficients were estimated and used as features. After 4 levels of decomposition, five signal components (1 approximation, and 4 details) are obtained. We estimated 3 features for each component, resulting in $5 \times 3 = 15$ features. Since these five components are zero-mean signals, their variances are equivalent to their powers, therefore providing a representation similar to the power spectrum, which is commonly used in EEG processing applications [18]. Since entropy is a measure of randomness, that is why we used it.. Unlike variance, entropy is considered a non-linear feature which has also been used in EEG processing applications [18].

2.3.2. Wigner-Ville distribution

Wigner-Ville distribution was first proposed by Wigner in 1932 [19]. It is a suitable transform for time-frequency analysis. This approach has more resolution compared to the short-time Fourier transform. Wigner-

Ville distribution $W_x(t,v)$ is given by Eq. (4):

$$W_x(t,v) = \int_{-\infty}^{+\infty} x\left(t+\frac{\tau}{2}\right)x^*(t-\frac{\tau}{2})e^{-j2\pi v\tau}d\tau \quad (4)$$

where t and v are time and frequency, respectively. In the end, 3 features including variance, mean, and signal wavelength are calculated from the Wigner-Ville distribution. If $\{|W_x(t,v_i)|, \quad i=1,2,3\}$ are the three frequency components of the absolute Wigner-Ville distribution $|W_x(t,v)|$ that have the highest power, the mean, variance and the wavelength of these three components are estimated. The respective features are then averaged, resulting in 3 features: an average mean, an average variance, and an average wavelength. The three averages were used as features.

2.4. Classification

Before classification, linear discriminant analysis (LDA) was used for dimensionality reduction. LDA finds linear combinations of features that best discriminate two or more classes of objects or individuals [20]. It is based on the assumption that the conditional probability density functions $p(X|Y=0)$ and $p(X|Y=1)$ both have normal distributions. The linear discriminator is found using the maximum likelihood discriminant rule from Eq. (5) [20].

$$P(Y=k|X) = \frac{P(X|Y=k)P(Y=k)}{\sum P(X|Y=j)P(Y=j)} \quad (5)$$

In Eq. (5), Y is the class index and X is the feature vector. Details of dimensionality reduction using LDA can be found in [21].

Using LDA, the features were reduced from 18 (15 extracted by discrete wavelet, and the other 3 by Wigner-Ville distribution) to 3.

In this study, three classification methods of *k*-nearest neighbor (kNN), support vector machine (SVM), and random forest (RF) were used to classify four emotions of happiness, scaredness, calmness, and boredom. The kNN was implemented by setting the parameter $k=3$ and RF was performed using 25 decision trees for calculations related to the algorithm.

The EEG signals were randomly divided into a training (80%) and a test (20%) set. The three classifiers (SVM, kNN, and RF) were trained on the training data and then evaluated on the test data.

2.4.1. Evaluation of the classifiers' performance

Three metrics were used for the evaluation of the classifiers: accuracy (A_c), precision (P_r), and recall (R_e). These metrics are defined as:

$$Ac = \frac{TP+TN}{TP+FP+TN+FN} \quad (6)$$

$$P_r = \frac{TP}{TP+FP} \quad (7)$$

$$R_e = \frac{TP}{TP+FN} \quad (8)$$

In Eqs. (6-8), TP is the number of patients correctly classified as patients, FN is the number of patients wrongly classified as healthy subjects, TN is the number of healthy

subjects correctly classified as healthy, and FP is the number of healthy subjects wrongly classified as patients. Multi-class versions of accuracy, precision, and recall are defined in [22].

3. RESULTS

Table 1 demonstrates the accuracy, precision, and recall of test data of each electrode using the SVM model. RF algorithm was also considered with 25 decision trees, which had the best performance (Table 2). The kNN algorithm was also considered with $k = 3$, which had the best performance (Table 3).

The accuracy of the three classification models, i.e. SVM, kNN, and RF, are briefly compared in Fig. 2. The SVM model and TP9 electrode had the best performance among all the three algorithms and recording electrodes.

Table 1. ***Accuracy, precision, and recall for the SVM classifier.***

Electrode	Accuracy	Precision	Recall
AF8	0.85	0.86	0.88
AF7	0.78	0.77	0.79
TP9	0.94	0.95	0.91
TP10	0.85	0.88	0.87

Table 2. ***Accuracy, precision, and recall for the RF classifier.***

Electrode	Accuracy	Precision	Recall
AF8	0.85	0.88	0.89
AF7	0.76	0.80	0.76
TP9	0.91	0.89	0.90
TP10	0.85	0.86	0.87

Table 3. ***Accuracy, precision, and recall for the kNN algorithm with $k = 3$.***

Electrode	Accuracy	Precision	Recall
AF8	0.83	0.85	0.84
AF7	0.71	0.72	0.73
TP9	0.85	0.88	0.85
TP10	0.81	0.85	0.82

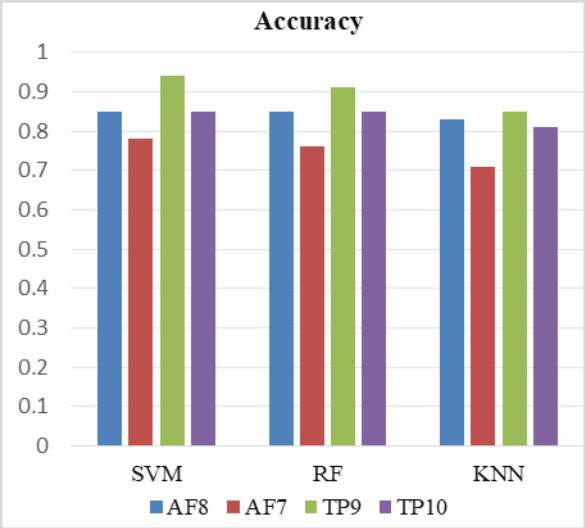

Fig. 2. Classification accuracy of the SVM, RF, and kNN algorithms for AF8, AF7, TP9 and TP10 electrodes.

Table 4. ***The obtained accuracies for three combinations of electrodes.***

Classifier	AF7-AF8	TP9-TP10	AF7-AF8-TP9-TP10
kNN	0.76	0.78	0.71
SVM	0.86	0.86	0.82
RF	0.84	0.85	0.81

The electrode combinations AF7-AF8, TP9-TP10, and AF7-AF8-TP9-TP10 (all electrodes) were also investigated. The results are summarized in Table 4.

4. DISCUSSION

This research investigated three non-linear classification methods (i.e. SVM, kNN, and RF) to recognize four emotions of scaredness, happiness, calmness, and boredom. The SVM ($Ac = 0.94$) outperformed both the RF ($Ac = 0.91$) and the kNN ($Ac = 0.85$). These results are consistent with the results reported in many other EEG processing applications [18], yet it might not be reasonable to generalize these results especially. In some studies on emotion recognition from EEG, kNN was reported to be the best classifier [18]. Therefore, more studies should be conducted to investigate the classification models using other feature types, feature selection or dimensionality reduction algorithms, and other datasets of emotion recognition.

Classification accuracy has been limited in many studies. For example, Gannouni et al. (2021) [23] obtained an accuracy of 89% for a four-class emotion recognition problem, which is lower than the accuracy we obtained (94%) using SVM. Sengur and Siuly (2020) [24] obtained a high accuracy of 94% which is comparable to the result we obtained. However, they had two classes of emotions while we used four classes of emotions. Our approach was also better than that of Subasi et al. (2021) [25] which gained an accuracy of 93% for a three-class classification problem. Housein et al. (2022) [26] conducted a review study on the classification of emotions based on the brain-computer interface and mentioned classification accuracy of machine learning methods varies from 61.17% to 93% in studies (Table 5). Therefore, this study seems to have a better performance compared to other studies. The machine learning models we used are not different from those used in other studies. Therefore, it seems that the combination of the time-frequency features extracted from the wavelet coefficients and the Wigner-Ville distribution provided an effective set of features for emotion classification.

It should be noted that the current study has a few limitations. First, the dataset that we used in this study included EEG data from only 4 recording channels. Therefore, it is necessary to evaluate the proposed method on other datasets with more recording channels. Another constraint of this study is the limited set of features we used. Features such as time-domain features could also be tested in future studies. Also, other feature

Table 5. ***Comparison of the results of this study with similar studies.***

References	Methods	Emotions	Accuracy
[27]	DT, kNN, RF	Positive, negative and neutral	74 %
[28]	LDA	Positive, negative and angry and harmony	82 %
[29]	SVM	Positive, negative and neutral	85.9 %
[30]	RF	Happy, sad, angry, calm	75.6 %
Present study	kNN, RF, SVM	Happy, scared, bored, calm	94.1 %

selection or dimensionality reduction techniques should be considered. In addition, linear and other non-linear machine learning models and deep learning-based models can be used to find the best classifier for emotion recognition.

5. CONCLUSION

In this study, classification of four emotions (i.e. happiness, calmness, boredom, and scaredness) was successfully performed using the SVM classifier and the features from the TP9 electrode. This achievement is due to the effective features that the discrete wavelet transform and the Wigner-Ville distribution provide. In future studies, other feature extraction and classification methods should be investigated for emotion classification.

REFERENCES

[1] Wang, J. and M. Wang, Review of the emotional feature extraction and classification using EEG signals. Cognitive robotics, 2021. 1: p. 29-40.

[2] Suhaimi, N.S., J. Mountstephens, and J. Teo, EEG-based emotion recognition: A state-of-the-art review of current trends and opportunities. Computational intelligence and neuroscience, 2020. 2020.

[3] Chang, H., Y. Zong, W. Zheng, C. Tang, J. Zhu, and X. Li, Depression assessment method: an eeg emotion recognition framework based on spatiotemporal neural network. Frontiers in Psychiatry, 2022. 12: p. 837149.

[4] Dev, A., N. Roy, M.K. Islam, C. Biswas, H.U. Ahmed, M.A. Amin, F. Sarker, R. Vaidyanathan, and K.A. Mamun, Exploration of EEG-based depression biomarkers identification techniques and their applications: a systematic review. IEEE Access, 2022. 10: p. 16756-16781.

[5] Kaur, B., D. Singh, and P.P. Roy, EEG based emotion classification mechanism in BCI. Procedia computer science, 2018. 132: p. 752-758.

[6] Al-Nafjan, A., M. Hosny, Y. Al-Ohali, and A. Al-Wabil, Review and classification of emotion recognition based on EEG brain-computer interface system research: a systematic review. Applied Sciences, 2017. 7(12): p. 1239.

[7] Pei, G. and T. Li, A literature review of EEG-based affective computing in marketing. Frontiers in Psychology, 2021. 12: p. 602843.

[8] Liu, Y., O. Sourina, and M.R. Hafiyyandi. EEG-based emotion-adaptive advertising. in 2013 Humaine Association Conference on Affective Computing and Intelligent Interaction. 2013. IEEE.

[9] Bălan, O., G. Moise, L. Petrescu, A. Moldoveanu, M. Leordeanu, and F. Moldoveanu, Emotion classification based on biophysical signals and machine learning techniques. Symmetry, 2019. 12(1): p. 21.

[10] Zhang, J., Z. Yin, P. Chen, and S. Nichele, Emotion recognition using multi-modal data and machine learning techniques: A tutorial and review. Information Fusion, 2020. 59: p. 103-126.

[11] Domínguez-Jiménez, J.A., K.C. Campo-Landines, J.C. Martínez-Santos, E.J. Delahoz, and S.H. Contreras-Ortiz, A machine learning model for emotion recognition from physiological signals. Biomedical signal processing and control, 2020. 55: p. 101646.

[12] Liu, J., H. Meng, M. Li, F. Zhang, R. Qin, and A. Nandi, Emotion detection from EEG recordings based on supervised and unsupervised dimension reduction. Concurrency and Computation: Practice and Experience, 2018. 30: p. e4446.

[13] Acharya, D., R. Jain, S.S. Panigrahi, R. Sahni, S. Jain, S.P. Deshmukh, and A. Bhardwaj. Multi-class emotion classification using EEG signals. in Advanced Computing: 10th International Conference, IACC 2020, Panaji, Goa, India, December 5–6, 2020, Revised Selected Papers, Part I 10. 2021. Springer.

[14] Ghosh, S.M., S. Bandyopadhyay, and D. Mitra, Nonlinear classification of emotion from EEG signal based on maximized mutual information. Expert Systems with Applications, 2021. 185: p. 115605.

[15] Suhaimi, N.S., J. Mountstephens, and J. Teo, A dataset for emotion recognition using virtual reality and EEG (DER-VREEG): emotional state classification using low-cost wearable VR-EEG headsets. Big Data and Cognitive Computing, 2022. 6(1): p. 16.

[16] Bhardwaj, A., A. Gupta, P. Jain, A. Rani, and J. Yadav. Classification of human emotions from EEG signals using SVM and LDA Classifiers. in 2015 2nd International Conference on Signal Processing and Integrated Networks (SPIN). 2015.

[17] Al-Qerem, A., F. Kharbat, S. Nashwan, S. Ashraf, and K. Blaou, General model for best feature extraction of EEG using discrete wavelet transform wavelet family and differential evolution. International Journal of Distributed Sensor Networks, 2020. 16(3): p. 1550147720911009.

[18] Saeidi, M., W. Karwowski, F.V. Farahani, K. Fiok, R. Taiar, P.A. Hancock, and A. Al-Juaid, Neural decoding of EEG signals with machine learning: a systematic review. Brain Sciences, 2021. 11(11): p. 1525.

[19] Alsalmi, H. and Y. Wang, Mask filtering to the Wigner-Ville distribution. Geophysics, 2021. 86(6): p. V489-V496.

[20] Xanthopoulos, P., P.M. Pardalos, T.B. Trafalis, P. Xanthopoulos, P.M. Pardalos, and T.B. Trafalis, Linear discriminant analysis. Robust data mining, 2013: p. 27-33.

[21] Gu, Q., Z. Li, and J. Han. Linear discriminant dimensionality reduction. in Machine Learning and Knowledge Discovery in Databases: European Conference, ECML PKDD 2011, Athens, Greece, September 5-9, 2011. Proceedings, Part I 11. 2011. Springer.

[22] Sokolova, M. and G. Lapalme, A systematic analysis of performance measures for classification tasks. Information processing & management, 2009. 45(4): p. 427-437.

[23] Gannouni, S., A. Aledaily, K. Belwafi,

and H. Aboalsamh, Emotion detection using electroencephalography signals and a zero-time windowing-based epoch estimation and relevant electrode identification. Scientific Reports, 2021. 11(1): p. 7071.

[24] Şengür, D. and S. Siuly, Efficient approach for EEG-based emotion recognition. Electronics Letters, 2020. 56(25): p. 1361-1364.

[25] Subasi, A., T. Tuncer, S. Dogan, D. Tanko, and U. Sakoglu, EEG-based emotion recognition using tunable Q wavelet transform and rotation forest ensemble classifier. Biomedical Signal Processing and Control, 2021. 68: p. 102648.

[26] Houssein, E.H., A. Hammad, and A.A. Ali, Human emotion recognition from EEG-based brain–computer interface using machine learning: a comprehensive review. Neural Computing and Applications, 2022. 34(15): p. 12527-12557.

[27] Qing, C., R. Qiao, X. Xu, and Y. Cheng, Interpretable emotion recognition using EEG signals. Ieee Access, 2019. 7: p. 94160-94170.

[28] Chakladar, D.D. and S. Chakraborty, EEG based emotion classification using "correlation based subset selection". Biologically inspired cognitive architectures, 2018. 24: p. 98-106.

[29] Huang, C., Recognition of psychological emotion by EEG features. Network Modeling Analysis in Health Informatics and Bioinformatics, 2021. 10: p. 1-11.

[30] Pane, E.S., A.D. Wibawa, and M.H. Purnomo, Improving the accuracy of EEG emotion recognition by combining valence lateralization and ensemble learning with tuning parameters. Cognitive processing, 2019. 20: p. 405-417.

Signal Processing and Renewable Energy
September 2024, (pp. 73-94)
ISSN: 2588-7327
eISSN: 2588-7335

Multi-objective Allocation of Distributed Generation Resources and Capacitor Banks Based on a Two-stage Fuzzy Method and Ɛ-constrained Optimization

Farzaneh Ostovat [1], Hassan Barati [*1], and Seyed Saeidallah Mortazavi [2]

[1] Department of Electrical Engineering, Dezful Branch, Islamic Azad University, Dezful, Iran.
[2] Department of Electrical Engineering, Shahid Chamran University of Ahvaz, Ahvaz, Iran.

Received: 06-Aug-2024, Revised: 21-Aug-2024, Accepted: 27-Aug-2024.

Abstract

Proper operation of distributed generation resources (DGs) in power systems has considerable advantages, including decreasing losses, reducing congestion in feeders, improving voltage profile, and enhancing stability, reliability, and security. On the other hand, using capacitor banks helps improve voltage profile and power quality in distribution systems. The optimal allocation of capacitor banks (CBs) and DGs has a significant impact on the efficiency of the distribution systems. This paper presents a method for distribution system planning based on the optimal allocation of DGs and CBs. The main objectives of the proposed method are to improve the voltage profile, reduce investment and operation costs, and reduce renewable energy curtailment. The planning problem is solved through multi-objective scheduling based on a two-stage fuzzy method and the ε-constrained optimization. The stochastic two-stage method is used to model uncertainty. The proposed method is implemented on an IEEE 33-bus test network in MATLAB and evaluated under three scenarios. It is proven that the voltage profile can be improved in the scenario of allocating capacitor banks based on lower investment costs compared to other scenarios. However, the voltage profile is improved more in the scenario of simultaneous allocation of capacitor banks and DGs by investing in more costs. In general, the proposed method properly improves the distribution system's performance in different aspects.

Keywords: Multi-Objective Optimization, Capacitor Bank Allocation, DG Allocation, Two-Stage Method.

***Corresponding Authors Email:** barati216@gmail.com

1. INTRODUCTION

Most distribution systems are passive radial networks with unidirectional power flow. Upon the introduction of DGs to distribution networks, these systems are converted to active systems with bidirectional power flow [1]. DGs bring benefits, such as reducing losses, decreasing congestion in feeders, improving stability, voltage profile, and power quality, peak-shaving, and reducing investment, operation, and reliability costs. In addition, the power systems become more secure [2]. Studies have shown that power losses in a distribution system comprise power system losses [3]. Operationally speaking, real power loss directly affects the power system's efficiency. However, to preserve voltage in the allowed range and free transmission capacity, the reactive power flow in the feeders should be limited to a certain value [4]. With optimal operation management of DG units, the reactive power flow can be controlled, and the losses can be reduced [5]. However, the main problem with using DG units is finding the optimal capacity and location, considering the operation constraints. The application of DG units in distribution systems leads to the inverse power flow direction, resulting in high losses and overloading [6]. In addition, the high penetration level of DG units in the system reduces the balance between consumption and generation, which increases losses [7]. In distribution systems, power loss is an essential factor for increasing system efficiency. To this end, optimal allocation of capacitor banks (CBs), network configuration, and DG allocation are well-known methods [8].

Proper planning of the penetration level of DGs affects reducing active and reactive losses [9]. DG resource owners tend to sell more energy. On the other hand, a distribution system operator (DSO) seeks to absorb more local power generation capacity to control the network and curb power losses, operation costs, and emission of destructive pollutants. However, improper determination and measurement of DG resources aggravate power losses, which is undesired for DSOs [10].

With the growth of demand and updates in distribution and power networks, investment in energy has increased significantly. On the other hand, requirements for higher power quality have motivated investors to consider improving power quality and reliability and reducing harmonic current and voltage distortions more accurately [11]. A common strategy to improve power quality is to install CBs to compensate for reactive power, correct the power factor, reduce energy loss, and preserve the bus voltage. CBs are costly components whose capacity, location, and switching influence stability and power quality significantly [12]. Therefore, their proper allocation is crucial for maximizing energy loss reduction and improving losses. Various parameters like voltage constraints, load changes, and other parameters have complicated the configuration of capacitances and their switching.

Numerous studies have addressed the optimal allocation of DG units and CBs. In [13], a method has been presented for distribution system planning, considering flexibility requirements and adjustment laws. In this study, mixed integer linear

programming has been used based on local resources and passive elements in the distribution network. In [14], a method has been presented to design active distribution systems, considering active network management and optimization for load curtailment. In this paper, the researchers have presented an optimal load curtailment model for distribution planning. The proposed method seeks to determine the optimal type, location, and capacity of the feeders, DGs, CBs, static compensators, and regulators. In [15], a robust two-stage optimization method has been presented for planning active distribution networks coupled with urban transportation networks. Load uncertainty, renewable energy resources, and traffic demand have been considered in this study. In [16], a method has been presented for planning distribution networks considering uncertainty, prolonging investment, hydrogen storage devices, and wind resources. The authors in [17] have focused on the effect of load changes on the planning of a distribution system and optimal allocation of DGs, considering the reduction of energy losses. In [18], distribution system planning based on MICP in a radial distribution network has been presented for optimal allocation. The proposed model is based on hybrid integer conical programming. In [19], the planning of distribution systems and the optimal allocation of DGs have been studied in a radial distribution network based on the stability index under load growth. In [20], a model has been presented for the optimization of distribution systems, the allocation of DG resources, and the configuration of distribution networks based on the BF-SD algorithm considering the phase imbalance. The authors in [21] have studied the multi-objective optimal power flow with DG resource allocation using TLBO and MIPSO algorithms. In [22], a method based on environmental, technical, and economic goals has been presented for the optimal allocation of DG resources in distribution networks.

Ref. [23] has contributed to designing, modeling, and scheduling DG resources, including wind and solar systems, using a particle swarm algorithm. DGs are used to supply the output load during peak hours of the day and night. Probability distribution functions are used, and outputs are expressed as probability density distribution functions instead of absolute numbers. In [24], microgrid optimal scheduling considering normal and emergency operations has been investigated. A chance-constrained model is developed to handle normal operation and emergency conditions of the microgrid, including DG outage and unwanted islanding. Storage purchase from the upstream network is also considered. In addition, the uncertainty of loads and renewable resources is included in the model. Ref. [25] has been dedicated to comparing network reliability indicators before and after the introduction of DGs and analyzing their impact on improving network reliability. The improvement of indicators based on customer satisfaction, including the reduction of SAIFI and SAIDI, is evaluated. More precisely, the improvement of the most important index based on load and energy, i.e., energy not supplied (ENS), is investigated. In order to reduce the distribution system loss, the simultaneous optimal placement of DG

resources and capacitors in radial distribution systems has been studied in [26] in which the crow search algorithm has been used for the optimization. Ref. [27], an optimization approach based on an arithmetic optimization algorithm (AOA) is proposed for specifying the optimal allocation of distribution generations/generators (DGs) and capacitor banks (CBs) in radial distribution systems. The AOA is a new population-based meta-heuristic algorithm that is essentially based on using basic arithmetic operators in mathematics. The proposed approach is employed to specify the optimum placement, capacity, and power factor of DGs and CBs to decrease the distribution systems' total power loss and voltage deviation. In Ref. [28] introduces the Energy Valley Optimizer, a novel tool designed for the strategic placement of distributed generation units and capacitor banks. This placement is crucial not only for optimizing energy loss and enhancing bus voltage stability but also for promoting sustainable energy use and reducing environmental impact over the long term. By minimizing energy loss and voltage fluctuations, the optimizer contributes to a more sustainable and resilient energy system. Ref. [29] proposes a two-stage procedure to enhance the distribution system performance by determining the optimal sizes and locations of distributed generations (DGs) and capacitors considering single and multi-objective functions. In stage-1, two voltage sensitivity factors (VSFs) based on voltage deviation (VD), and voltage stability index (VSI) are proposed to reduce the search space (SS) by selecting the candidate buses for DGs and capacitors placement. In stage-2, the chaotic bat algorithm (CBA) is applied to find the optimal sizes and locations of DGs and capacitors, according to different objective functions (OFs) and system constraints. The considered OFs are real power loss reduction, total VD minimization, and total VSI maximization. The multi-OF, which aims to optimize these objectives simultaneously, is also considered.

The present paper proposes a novel method to optimally allocate the DG resources and capacitor banks. Multiple objectives are considered, including reducing operation and investment costs, improving voltage profile and reliability, and reducing curtailment costs. Moreover, uncertainties are included in the proposed method using stochastic modeling. The multi-objective ε-constrained optimization method is used to solve the planning program. In addition, fuzzy decision-making is used to select the best solution among non-dominated solutions.

This paper is organized as follows. Section 2 describes the problem formulation, including objective functions and constraints. Section 3 describes the solution approach, including the optimization method, uncertainty modeling, and fuzzy decision-making. Section 4 describes the results and discussion. Finally, Section 5 is dedicated to conclusion.

2. PROBLEM FORMULATION

This section presents the cost function of optimal DG and CB allocation. In this modeling, the objectives are to minimize the operation and investment costs, improve reliability and voltage profile, and reduce power curtailment. In general, distribution network companies are responsible for

satisfying the consumers' requirements and managing CBs and DGs in the distribution system. The objectives of interest are described below.

A. Objective functions

The first objective function is to minimize CB and DG costs. Costs include the DG investment cost (C_{DG}), which is given in Eq. (1) [27]:

$$C_{DG} = \sum_{i=1}^{NDG} P_{DGi} Inv_{DG} \quad (1)$$

in which P_{dgi} is the capacity of the DG units in MW, INV_{dg} is the investment cost of the unit in \$/MW, and Ndg is the number of units installed on the system. The investment cost of the CB (C_{cap}) is calculated as follows [27]:

$$C_{cap} = \sum_{j=1}^{Ncap} Q_{Capj} Inv_{cap} \quad (2)$$

in which Q_{capj} is the capacity of the capacitor bank in MVar, INV_{cap} is the investment cost of the CBs in \$/MW, and Ncap is the number of banks installed in the system.

Along with investment costs, operation and maintenance costs are also considered. Here, the maintenance and operation costs include fuel cost and annual maintenance cost. The operation cost (C_{oDG}) for DG units is calculated by

$$C_{ODG} = \left[\sum_{i=1}^{Ndg} P_{DGi} * O_{DG} * Oh\right] * \sum_{y=1}^{T} \left(\frac{1+inf}{1+int}\right)^{y} \quad (3)$$

in which O_{DG} represents the operation and maintenance cost of the DG unit in \$/MWh, and Oh represents the total number of operation hours in a year, which is 8760. Also, T denotes the number of years of the planning period, y denotes the year of operation, Inf denotes the inflation rate, and Int denotes the interest rate used to convert these costs to the current value. For the CBs, the cost only includes the maintenance cost (C_{mcap}) that is considered with the parameter MC_{cap} [27].

$$C_{Mcap} = [\text{MCcap}] * \sum_{y=1}^{T} \left(\frac{1+inf}{1+int}\right)^{y} \quad (4)$$

The second objective function, which is considered in the allocation problem, is reliability improvement. The following steps are taken to calculate reliability. The majority of distribution systems are radial. The annual failure rate (AFR), average outage time (AOT), and annual outage time (UOT) are the main parameters of reliability [28].

$$AFR = \sum_{j=1}^{Nsec} \lambda_j \quad (5)$$

$$AOT = \sum_{j=1}^{Nsec} \lambda_j * g_j \quad (6)$$

$$UOT = \frac{AOT}{AFR} = \frac{\sum_{j=1}^{Nsec} \lambda_j * g_j}{\sum_{j=1}^{Nsec} \lambda_j} \quad (7)$$

in which λ_j and gj are the AFR and the AOT of the j^{th} feeder, respectively. The current passing through the feeder sections has two active (IA) and reactive (IR) components. Optimal installation of DG resources and CBs partially supports the power demand,

which reduces the magnitude of the current passing through the feeder sections. This reduction minimizes the costs. The allocation of CBs and DGs improves reliability. Before optimal allocation, each section of the feeder has an uncompensated failure rate of $\lambda^{uncomp}{}_j$. After allocation, if the feeder's current component is completely compensated, the failure rate reaches 75% of $\lambda_{uncompj}$ [28], which is represented by λ_{compj}. If the feeder's current is not completely compensated, its failure rate is defined linearly by compensation percentage. The new failure rate after allocation is defined as

$$\lambda_{jnew} = \beta_j * \left(\lambda_j^{uncomp} - \lambda_j^{comp}\right) + \lambda_j^{comp} \quad (8)$$

in which β is the compensation factor calculated by

$$\beta_j{}^{AR} = \left|\frac{I_j^{new}}{I_j^{old}}\right| = \left|\frac{\sqrt{(I_j^{Anew})^2+(I_j^{Rnew})^2}}{\sqrt{(I_j^{Aold})^2+(I_j^{Rold})^2}}\right| \quad (9)$$

in which A represents the active part, R represents the reactive part, and $\beta_j{}^{AR}$ represents the factor in which the active and reactive parts of the current are considered. Also, new indicates after allocation, and old indicates before allocation. The absolute value of the current is used in the calculations. ECOST is used for reliability calculations. Thus, C_{rel} is determined by

$$C_{rel} = \sum_{b=2}^{n} L_i^{avg} C_i^{int} \lambda_j^{new} * \sum_{y=1}^{T} \left(\frac{1+inf}{1+int}\right)^y \quad (10)$$

in which L_i^{avg} is the average load connected to bus i in KW and C_i^{int} is the load disconnection cost in $/kW. Here, the total outage time of L_i^{avg} is related to the outage of each section of the feeder with $\lambda_j = \lambda_j^{new}$. Therefore, the first objective function considered in the planning is calculated as follows:

$$Cost_{total} = C_{dg} + C_{cap} + C_{ODG} + C_{Mcap} + C_{rel} \quad (11)$$

$$F_1 = Ecost = \sum_{m=1}^{M} Cost_{Total}^{m} \quad (12)$$

in which M is the number of scenarios and $Cost^m{}_{total}$ is the corresponding cost for the m^{th} scenario.This objective function is formulated as follows:

$$f_{Volt} = \frac{1}{T}\sum_{y=1}^{T}\frac{1}{N_{Bus}}\sum_{j=1}^{N_{Bus}}\left|V_i - V_{Ref}\right| \quad (13)$$

in which N_{bus} is the number of network buses and Vi is the real per unit voltage of the bus. It should be noted that V_{ref} is also 1 pu. The average voltage of the buses should be close to 1 pu so that the voltage profile can be improved. Therefore, the second objective function based on stochastic modeling is calculated as follows:

$$F_2 = Ef_{Volt} = \sum_{m=1}^{M} f_{volt}^{m} \quad (14)$$

in which the third objective function, which is related to the power curtailment cost, is given as:

$$F_{3,i} = Pen_i(P_{DGi}^{rated} - P_{DGi}) \quad (15)$$

in which i is the index of the buses, n is the number of network buses, and j is the index of the buses. In addition, P_{DGi} and P_{DGi}^{rated} are the injected active power and the rated PV output at bus i, respectively. Also, Pen_i is the penalty factor of bus i for power curtailment.

The third objective function based on stochastic modeling is calculated as follows:

$$F_3 = F_{DGCurt} = \sum_{m=1}^{M} \sum_{i=1}^{I} F_{3.i} \quad (16)$$

B. Constraints

The constraints of the allocation problem for the DG units and the CBs are as follows [30]:

$$P_{DG}^{Min} \le \sum_{i=1}^{Ndg} P_{dgi} \le P_{DG}^{Max} \quad (17)$$

$$Q_{cap}^{Min} \le \sum_{j=1}^{Ncap} Q_{capj} \le Q_{cap}^{Max} \quad (18)$$

$$P_{DG}^{Min} = 0.1 * \sum_{b=2}^{Nbus} P_{loadb} \quad (19)$$

$$Q_{cap}^{Min} = 0.1 * \sum_{b=2}^{Nbus} Q_{loadb} \quad (20)$$

$$P_{DG}^{Max} = 0.6 * \sum_{b=2}^{Nbus} P_{lb} \quad (21)$$

$$Q_{cap}^{Max} = 0.6 * \sum_{b=2}^{Nbus} Q_{lb} \quad (22)$$

in which P^{min}_{DG} and P^{max}_{DG} are the minimum and maximum power generation of the DGs, respectively. Also, Q^{min}_{cap} and Q^{max}_{Cap} are the minimum and maximum reactive power of the CBs, respectively. Also, P_{lb} and Q_{lb} are the active and reactive load power in bus b, respectively.

Another constraint that should be considered is the power flow constraint as follows:

$$P_{Gb} - P_{Lb} - V_i \sum_{j \in Ni} V_j \left[G_{bj} \cos(\theta_{bj}) + B_{bj} \sin(\theta_{bj})\right] = 0 \quad (23)$$

$$Q_{Gb} - Q_{Lb} - V_b \sum_{j \in Ni} V_j [G_{bj} \sin(\theta_{bj}) - B_{bj} \cos(\theta_{bj})) = 0 \quad (24)$$

in which P_{Gb} is the active power generated on bus b, P_{Lb} is the active power on bus b, V_b is the voltage of bus b, V_j is the voltage of bus j, θ_{bj} is the angle between bus b and j, Q_{Gb} is the reactive power generation on bus b, and Q_{Lb} is the reactive power on bus b.

The line capacity constraint is as follows:

$$S_{ij}^{min} \le S_{ij} \le S_{ij}^{max} \quad (25)$$

in which Sij is the apparent power of line ij, and S_{ij}^{min} and S_{ij}^{max} are the minimum and maximum apparent power, respectively.

The multi-scenario balance should be satisfied. The stochastic model has a higher number of energy balance constraints than certain methods.

3. SOLUTION APPROACH

This paper considers demand uncertainty as stochastic scheduling. Then, the load is modeled. The power system operator should

predict the demand at each hour of the upcoming hours. Since the prediction process has errors, the demand prediction is not accurate. The demand prediction uncertainty is usually modeled with a normal distribution density function. To create a limited number of demands at each hour, a distribution curve is developed likeFig. 1.

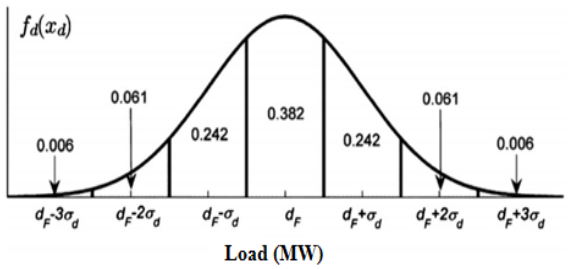

Fig. 1. 7-interval Gaussian distribution approximation.

In the proposed method, the demand error is assumed to be of normal distribution, and the weights P_d are determined using the area under the upper and lower constraint curves of each interval [31]:

$$P_d = 1/\sigma_d\sqrt{2\pi}\int_{l_j}^{u_j} e^{-(x-d_f)^2} /2{\sigma_d}^2 d_x \qquad (26)$$

in which u_j and I_j are the upper and lower demand constraints in each interval and d_f and σ_d are the predicted demand and std of the normal PDF, respectively. Stochastic modeling is carried out using the Markov process. Then, multi-objective modeling is carried out.

The ϵ-constrained method is a proper technique for solving multi-objective functions [32]. In the ϵ-constrained method, ranges of N-1 objective functions are required for N objective functions. The pay-off table is the most common technique to obtain these ranges. The pay-off concept, which shows the relationship between all possible events or acts and the values associated with the consequences, can help decision-making concerning competitive bid determinations. In this method, N-1 functions are used as additional constraints. A comprehensive description of the payment table and the ranges of the objective functions is given in [33]. Despite the advantages of the ϵ-constrained method, it has two major problems: first, the range of the objective functions in the efficient set might not be optimal; second, the optimal solutions that are generated by the ϵ-constrained method might not be dominant. The lexicographic method is suggested to overcome the first problem, and the ϵ-constrained technique is suggested to solve the second problem, according to [32]. The importance of the objective function for generating Pareto solutions is modeled using the hybrid aggregated-weighted ϵ-constrained method. In previous studies, efforts have been made to implement lexicographic optimization and the hybrid aggregated-weighted ϵ-constrained method for solving multi-objective optimal allocation problems. In this study, the lexicographic optimization and the hybrid aggregated-weighted ϵ-constrained method are used to solve the stochastic optimal multi-objective allocation problem. The modified ϵ-constrained method is given below.

The hybrid aggregated-weighted ϵ-constrained method can be modeled by:

$$Min\ /Max\ \ F_1(x) + \frac{dir_1 r_1}{W_1}\sum_{n=2}^{N}\frac{w_n S_n^{nk}}{r_n} \qquad (27)$$

This equation is constrained by

$$\begin{aligned} &F_n(x) - dir_n S_n^{nk} - e_n^{nk} = 0 \\ &\qquad S_n^{nk} \in R^+, \\ &nk = 0, \qquad a, \dots., q_n, n = 2,, N \end{aligned} \tag{28}$$

$$\begin{aligned} e_n^{nk} = &\frac{F_n^{min}(1 + dir_n)}{2} \\ &- F_n^{max}(-1 + dir_n) \\ &+ \frac{dir_n r_n nk}{q_n} \end{aligned} \tag{29}$$

$$nk = 0,1, \dots qn \ , \qquad n = 2, \dots, N$$

in which dir_n is the direction of objective function n, and dir_n is -1 when the objective function n is minimized and +1 when the objective function is maximized. The main relationship should be optimized to achieve non-dominated optimal Pareto solutions. These relationships and the optimization are based on the method presented in [34].

Fuzzy decision-making could be employed by the system operator to select one of the optimal Pareto solutions. The fuzzy decision-making can select the best solution among non-dominated solutions. In this technique, the linear membership function is calculated for each objective function in the optimal Pareto solution.

The linear membership for the n^{th} objective function that should be minimized or maximized is defined by the following equations:

$$\mu_n^r = \begin{cases} 0 & F_n^r \le F_n^{min} \\ \dfrac{F_n^{max} - F_n^r}{F_n^r - F_n^{min}} & F_n^{min} \le F_n^r \le F_n^{max} \\ 1 & F_n^{max} \le F_n^r \end{cases} \tag{30}$$

$$\mu_n^r = \begin{cases} 1 & F_n^r \le F_n^{min} \\ \dfrac{F_n^{max} - F_n^r}{F_n^r - F_n^{min}} & F_n^{min} \le F_n^r \le F_n^{max} \\ 0 & F_n^{max} \le F_n^r \end{cases} \tag{31}$$

The total membership of r^{th} optimal Pareto solution based on independent membership functions of μ^r_n is calculated as follows:

$$\mu^r = \frac{\sum_{n=1}^{N} W_n \mu_n^r}{\sum_{n=1}^{N} W_n} \tag{32}$$

The system operator can select the value of w_n to prioritize the objective functions depending on the system conditions. The best optimal Pareto solution is selected by the fuzzy decider by selecting the maximum value for μ^r. There are several solution methods to determine the Pareto function. The three goals of Pareto optimization can be defined and measured as follows: the distance from the set of non-dominant results to the Pareto front should be minimized, proper distribution of the obtained solutions should be established, and the size of the obtained non-dominant front should be maximized.

The problem of optimal stochastic planning multi-objective optimal allocation is solved using the stochastic planning method to consider the demand uncertainty. According to stochastic two-stage planning, the decision-making variables are divided into two groups, including fixed subsets, e.g., here-and-now sets, and the expectation and observation variables. The optimal values of the expectation and observation variables depend on different scenarios, and their optimal values are obtained after the scenarios are realized. The optimal values of

the here-and-now variables are fixed for all scenarios.

The here-and-now variables are obtained in the first stage, and the expectation and observation variables are obtained in the second stage. The first stage of the stochastic problem is implemented using load predictions to obtain the optimal values of the here-and-now variables. The Monte Carlo and the corresponding scenarios are obtained in parallel using the described method. Then, the second stochastic planning stage is implemented to obtain the optimal values of the expectation and observation variables. Since the stochastic planning method is used, three objective functions with expected values of the scenarios are used. The expected values of the expectation and observation variables depend on the scenarios and their weights, which are obtained by aggregating the corresponding values adopted from the scenarios. Finally, the Pareto fronts of the objective functions are obtained using the modified ϵ-constrained optimization method, and fuzzy decision-making is used to attain the best compromise solution.

The procedure for solving the problem is that first the input information including load, capacitor banks and DG products is received. Then, the input variables of the hybrid constrained ϵ optimization, i.e., its input settings, are obtained. After that, the objective functions are calculated. That is, the optimization method takes into account a starting point, for example, the positions and capacities for the capacitor bank and distributed generation, and based on them, the objective functions are calculated. It should be considered that by calculating the objective functions, all variables are calculated probabilistically and the functions are calculated for all scenarios. Once the calculation procedure is completed, the variable optimization procedure is changed again and more favorable points are sought for the location and capacity of distributed generation units and capacitor banks, and the objective functions are calculated again. These steps are repeated until the termination criterion of the hybrid-constrained ϵ optimization algorithm is met.

The flowchart of the proposed method is shown in Figure 2.

4. RESULTS AND DISCUSSION

In this study, an IEEE 33-bus test system was used to analyze the performance of the proposed method. The baseline kV of this network was 12.66kV. In this network, the main breaker was located in the main feeder. To calculate the reliability of the reference bus, it was considered 1. The feeder section with maximum impedance had a maximum failure rate of 0.5 failures per year, and the feeder section with minimum impedance had a minimum failure rate of 0.1 failures per year [33]. The failure rates for other sections were calculated using a linear relationship between these two rates.

After allocating the DG resources and CBs, if section j was compensated completely, its failure rate was reduced to 75% of λ^{uncomp}; otherwise, λ^{new} was calculated through descriptive relationships for partial compensation. The time required for fault detection and switching was half an hour, and the repair time was considered four hours [35].

Since allocating DG resources and CBs would affect the reliability of other components like transformers, all other components of the distribution network except feeder sections were considered to be reliable. Table 1 presents the economic factors of the DG resources. Table 2 presents the economic factors of the CBs. Table 3 reports the total economic parameters.

For all case studies, the modified ϵ-constrained optimization method was applied to the objective function.

Scenario 1: Optimal planning of optimal allocation of DG resources

Scenario 2: Optimal planning of optimal allocation of CBs

Scenario 3: Optimal planning of optimal allocation of DGs and CBs simultaneously

A. Scenario 1: Analyzing the Results of DG Allocation

In this section, only DG resource allocation and its impact on the system is evaluated. It is assumed that three DGs are installed. The purpose is to examine the problem with two and three objectives. In this case, the first objective function is to minimize the costs, which is considered the main objective function. Also, the side objectives include improving the voltage profile and reducing generation curtailment; the weight factors for F_1, F_2, and F_3 are selected as 1, 1, and 1. However, the decider (system operator) might require different weights to obtain the desired solutions. Fig. 3 and Fig. 4 show the two objective solutions of the optimization output. As it can be seen inFig. 3, by installing DG resources and increased investment costs, the power curtailment decreases. It can be inferred from Fig. 4 that by increasing the investment cost on the set of solutions, the voltage profile improves. As mentioned, the voltage profile improvement objective function is obtained by minimizing the difference between the voltage of each bus from 1 pu, which is a very small number. The figures show the average real voltage for $f_{voltage}$ to help understand the voltage profile improvement and closeness to 1 pu. Also, the voltage at the output of the objective function refers to average voltage profile of all buses.

Fig. 5 shows the output set of the Pareto solutions of the three-objective solution. The best solution among the solutions in Fig. 5 is selected by the fuzzy method based on the operator's decision about compromising among different objectives, which is given in Table 4.

Table 1. ***Economic parameters of DGs [27].***

Parameter	Value
Investment cost ($/MW)	3180000
Operation cost ($/MWh)	36

Table 2. ***Economic parameters of CBs [27].***

Parameter	Value
Investment cost ($/MVar)	4000
Operation cost ($/Year)	10% of investment cost

Table 3. ***Total economic parameters [27].***

Parameter	Value
Inflation rate (%)	9
Interest rate (%)	12.5
Ks ($/MWh)	49

According to Table 4, buses 4, 11, and 31 represent the locations of DG output with the given capacities. Table 4 also shows the reliability cost (5.0604×10^5), which has improved by 21% compared to the base scenario.

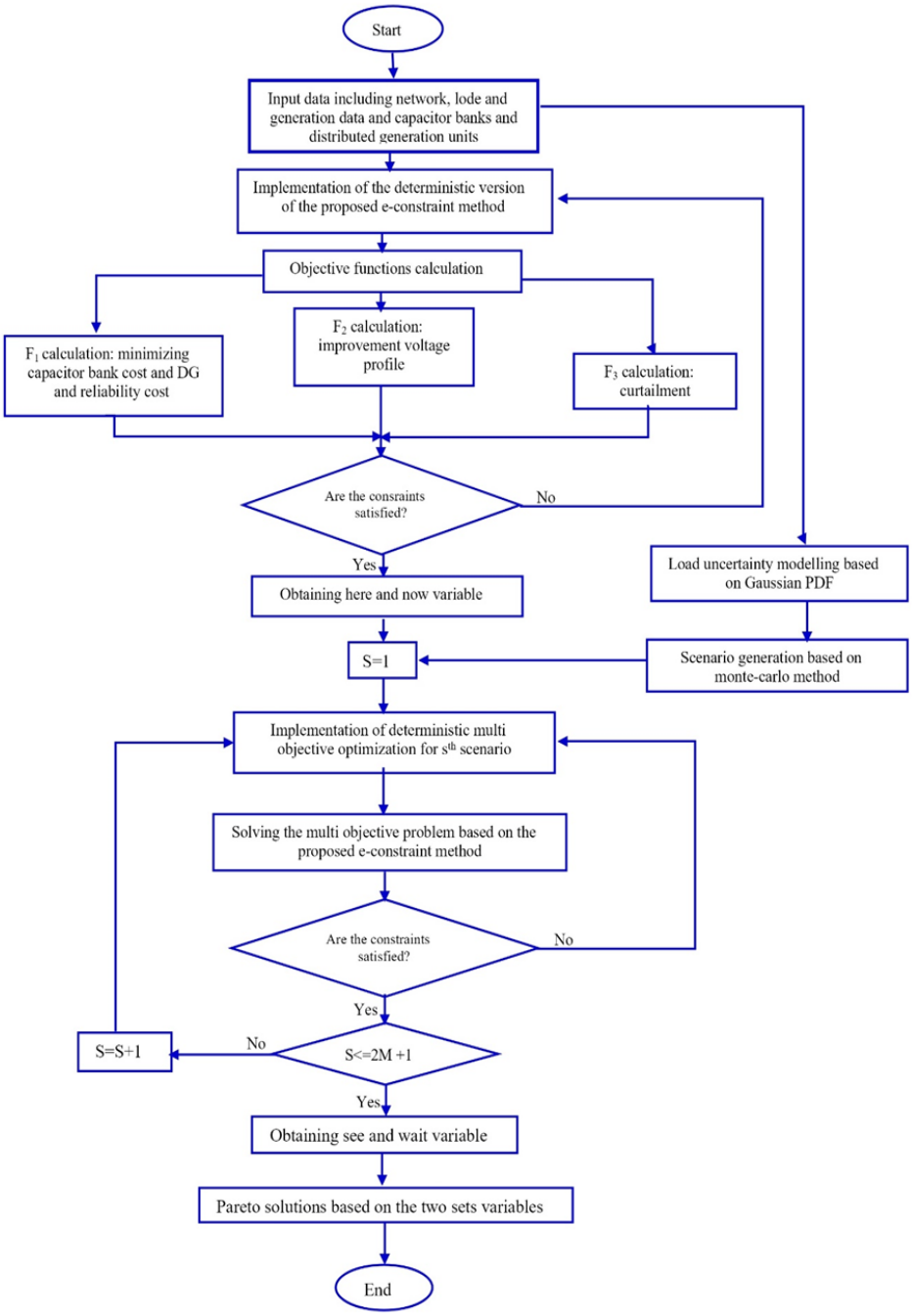

Fig. 2. The flowchart of the proposed method.

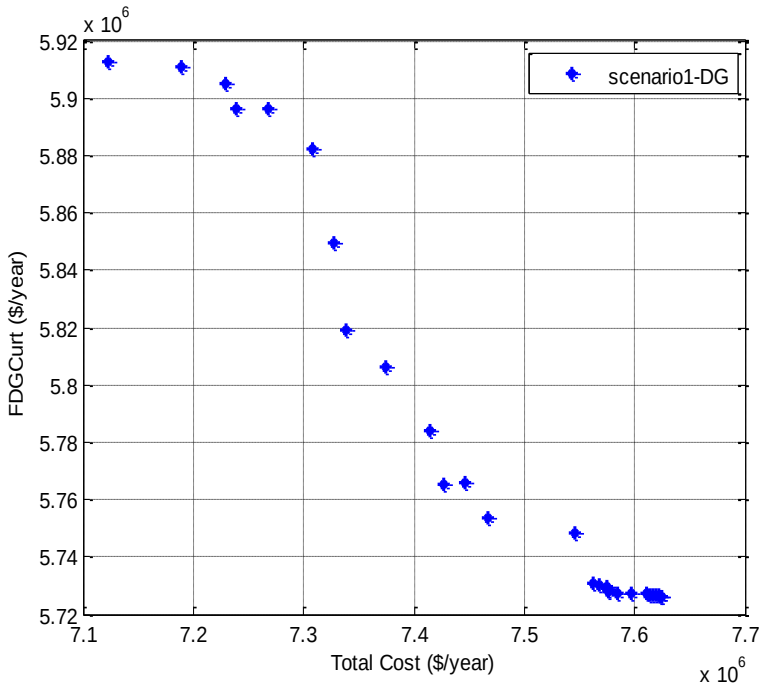

Fig. 3. The set of Pareto fronts of the two-objective solution of the first scenario (objectives: cost and power curtailment).

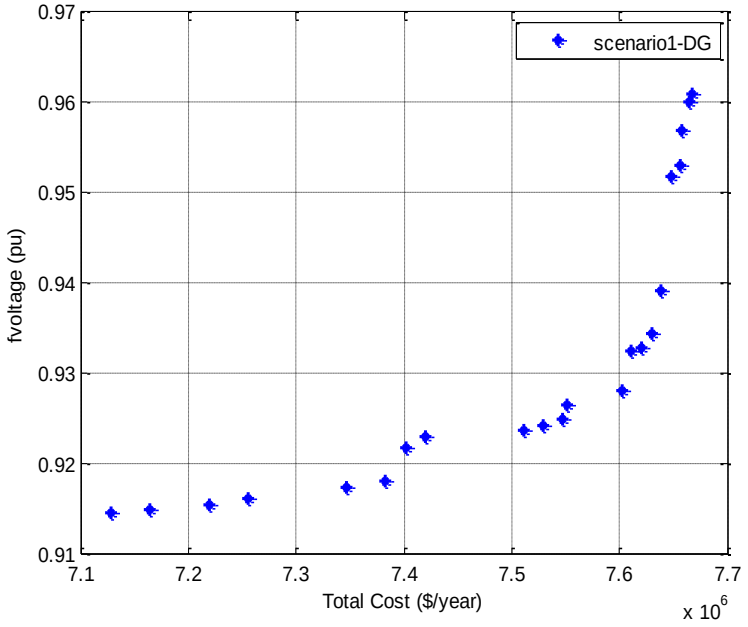

Fig. 4. The set of Pareto fronts of the two-objective solution of the first scenario (objectives: cost and voltage profile).

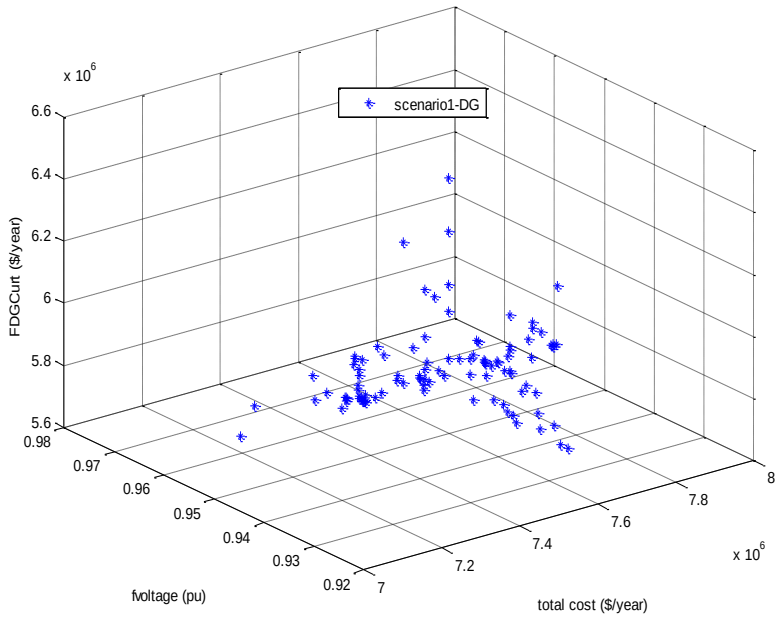

Fig. 5. The set of Pareto outputs of three-objective solution in the first scenario.

Table 4. ***The outputs of the fuzzy method for selecting the best solution of three objective solutions for the first scenario.***

Parameter	Value
Location of DG1	Bus 4
Capacity of DG1 (MW)	0.7526
Location of DG2	Bus 11
Capacity of DG2 (MW)	0.7397
Location of DG3	Bus 31
Capacity of DG3 (MW)	0.7413
Investment cost of DGs ($/year×$10^5$)	7.9702
Operation cost of DGs ($/year×$10^6$)	6.1079
Reliability cost ($/year×$10^5$)	5.0604
Total cost ($/year×$10^6$)	7.411
Power curtailment cost ($/year×$10^6$)	5.887

B. Scenario 2: Analyzing the results of CB Allocation

This section examines the allocation of CBs and its impact on the test system. It is assumed that three CBs are installed. The purpose is to examine the problem with two and three objectives. To this end, in the modified ϵ-constrained method, the first objective function, which is cost minimization, is considered the main objective function. The other objectives include improving the voltage profile and power curtailment, and the weighting factors for all objective functions are set to 1. Figs. 6 and 7 show the two objective solutions of the optimization output for CB allocation. Also, it can be inferred that the desired voltage profile can be achieved by less investment cost in CB allocation.

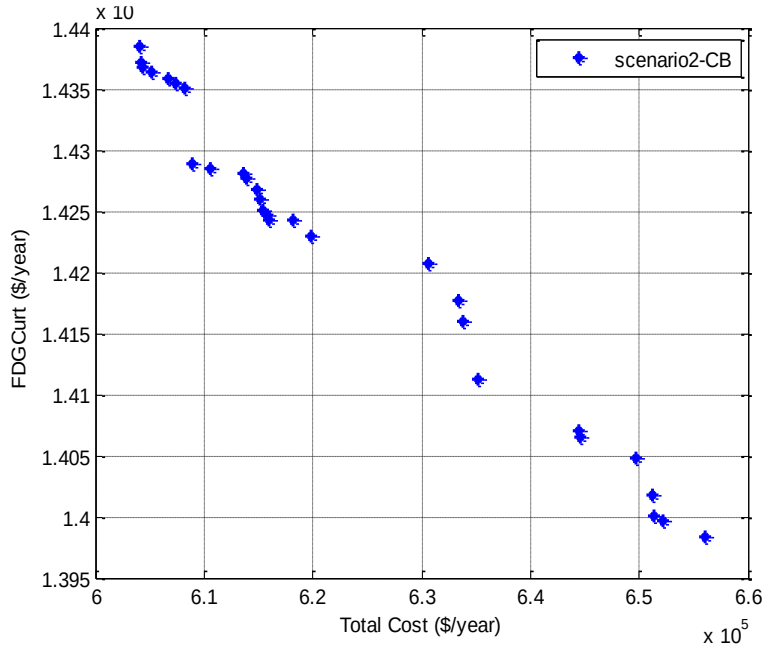

Fig. 6. The set of Pareto fronts of the two-objective solution of the second scenario (objectives: cost and power curtailment).

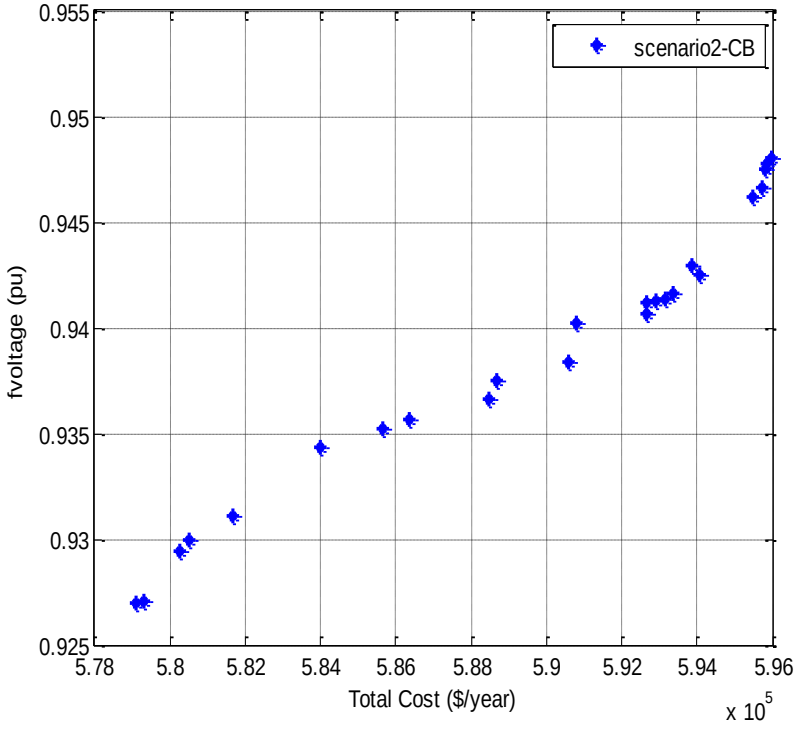

Fig. 7. The set of Pareto fronts of two objective solutions of the second Scenario (objectives: cost and voltage profile).

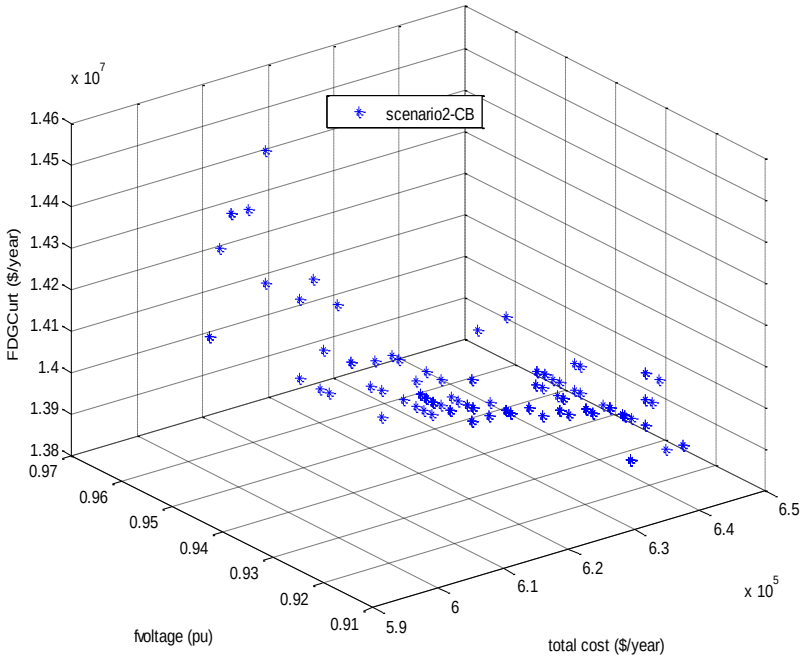

Fig. 8. The set of Pareto fronts of the three-objective solution in the second scenario.

Fig. 8 shows the output set of the Pareto solutions of the three-objective solution. The output of the fuzzy method for operator decision is given in Table 5. This solution is selected among the solutions given in Fig. 8. According to Table 5, buses 12, 26, and 29 are the output locations of the CBs with given capacities. The reliability cost (5.998×10^5) is also shown in this table, which has improved by 6% compared to the base case. This improvement arises from voltage profile enhancement and the reduction of its impacts on the power supply. It should be mentioned that CB allocation does not result in much difference compared to the base case, which is due to the dependency of CBs on voltage, and the impact of these CBs is more obvious in the voltage profile. Considering the lower costs, the CBs help the voltage profile; by installing them with DGs, simultaneously, more objectives are realized, which are discussed in the next section.

Table 5. ***The results of the fuzzy method for selecting the best solution of the three-objective solutions for the second scenario.***

Parameter	Value
Location of CB1	Bus 12
Capacity of CB1 (MVar)	0.4472
Location of CB2	Bus 26
Capacity of CB2 (MVar)	0.4490
Location of CB3	Bus 29
Capacity of CB3 (MVar)	0.4674
Investment cost of CBs ($/year×$10^3$)	5.418
Operation cost of CBs ($/year×$10^3$)	4.572
Reliability cost($/year×$10^5$)	5.998
Total cost($/year×$10^5$)	6.098
Power curtailment cost ($/year×$10^7$)	1.401

C. Scenario 3: Analyzing results of Allocating DGs and CBs

This section reports the results of the simultaneous allocation of CBs and DGs. It is assumed that three DGs and three CBs can be installed. In this scenario, like the two previous scenarios, the problem is examined with two and three objectives. To this end, in the modified ϵ-constrained method, the first objective function, which is cost minimization, is considered the main one. Also, side objectives include improving voltage profile and power curtailment. The weighting factors for all objective functions are 1. Figs. 9 and 10 depict the set of two objective solutions for the simultaneous allocation of CBs and DGs. According to these figures, more desired solutions are obtained compared to the first and second scenarios, and the voltage profile is improved properly.

Fig. 11 shows the set of the three-objective Pareto fronts for the third scenario. The output of the fuzzy method for operator decision is given in Table 6. This solution is selected among the solutions presented inFig. 1, based on which the best solution for operating among the set of solutions is obtained using the fuzzy method.

According to Table 6, buses 12, 25, and 30 are the output locations of the CBs, and buses 12, 24, and 30 are the optimal locations of the DGs. The reliability cost (4.53×10^5) is also shown in this table, which has improved by 30% compared to the base case, and it is better than the first and second scenarios. Also, considering all figures, it can be inferred that the best voltage profile occurred in the third scenario, which is due to the optimal simultaneous allocation of CBs and DGs. Also, the power curtailment cost of the network in this scenario is better than that in the two other Scenarios.

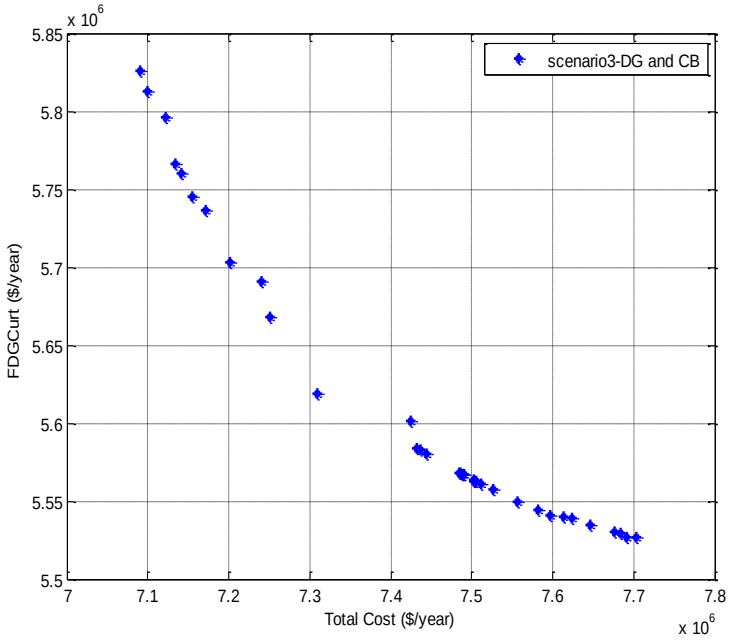

Fig. 9. The set of Pareto fronts of two objective solutions in the third scenario (objectives: cost and power curtailment).

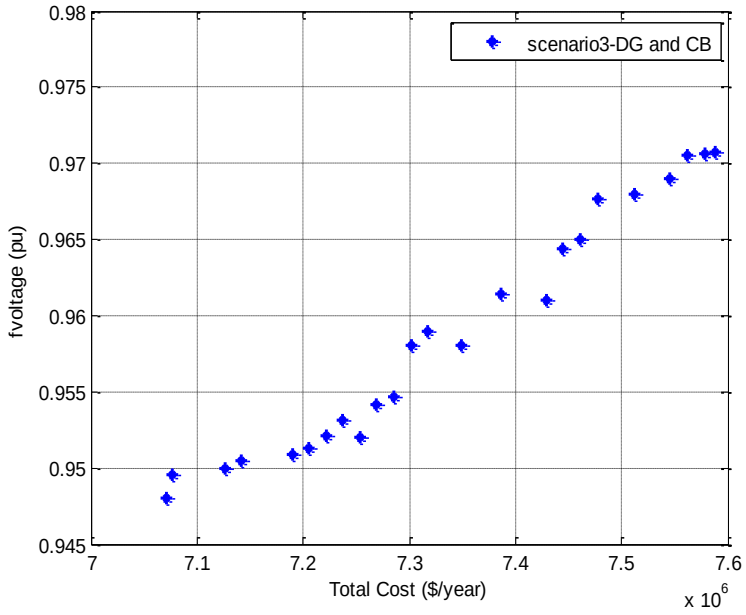

Fig. 10. The set of Pareto fronts of two objective solutions in the third scenario (objectives: cost and voltage profile).

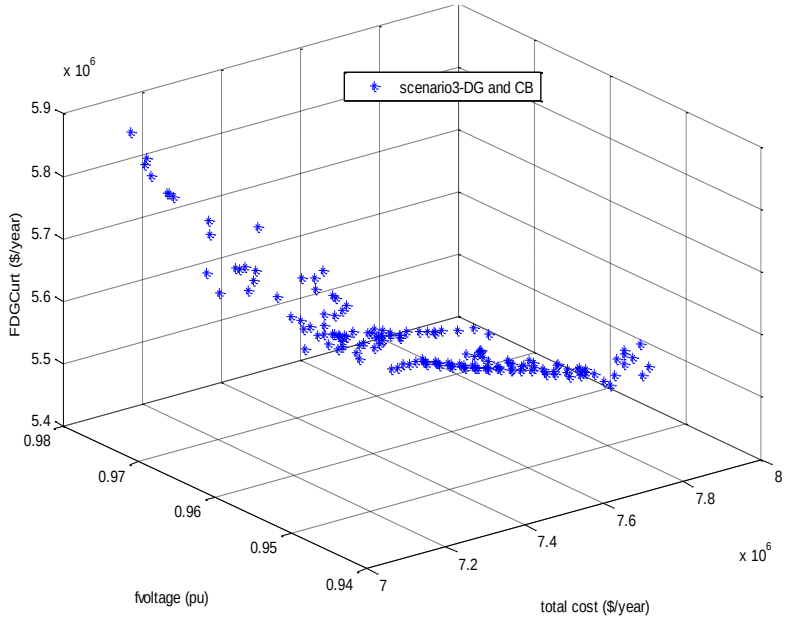

Fig. 11. Pareto fronts of three-objective solutions in the third scenario.

Compared to reference [26], this paper proposed a new multi-objective method for simultaneous optimization of DG and CBs placement under uncertainty. In [26], loss reduction and voltage profile enhancement are the objective functions. In this paper, voltage profile improvement, investment and operation costs reduction, and renewable energy curtailment reduction are the objective functions. The renewable energy

curtailment reduction is rarely discussed in the literature. Moreover, this paper used two-stage stochastic fuzzy modeling compared to [26]. The results proved the higher efficiency and accuracy of the proposed method by considering the uncertainty.

Table 6. The results of the fuzzy method for selecting the best solution among the three-objective solutions for the third scenario.

Parameter	Value
Location of DG1	Bus 12
Capacity of DG1 (MW)	0.7415
Location of DG2	Bus 24
Capacity of DG2 (MW)	0.7383
Location of DG3	Bus 30
Capacity of DG3 (MW)	0.7422
Location of CB1	Bus 12
Capacity of CB1 (MVar)	0.3450
Location of CB2	Bus 25
Capacity of CB2 (MVar)	0.2615
Location of CB3	Bus 30
Capacity of CB3 (MVar)	0.4422
Investment cost of DGs ($/year×$10^5$)	7.0776
Operation cost of DGs($/year×$10^6$)	6.3428
Investment cost of CBs($/year×$10^3$)	4.644
Operation cost of CBs($/year×$10^3$)	3.919
Reliability cost($/year×$10^5$)	4.531
Total cost($/year×$10^6$)	7.512
Power curtailment cost($/year×$10^6$)	5.495

5. CONCLUSION

This paper proposed a novel method for the optimal allocation of DG resources and CBs. Reducing operation and investment costs, improving voltage profile and reliability, and reducing curtailment costs were considered objective functions. The multi-objective ϵ-constrained optimization method was used to solve the problem. The proposed method was implemented on an IEEE 33 bus test system in three scenarios. The proposed method improved the performance of the system in different terms, including voltage profile and reliability. Moreover, it was concluded that the voltage profile improvement could be achieved in the scenario of capacitor banks' allocation by lower investment costs compared to other cases. As a result of the use of DG and capacitor banks, less voltage deviation and lower curtailment costs were obtained. Also, the reliability of the network would be better due to equipping the network with DGs and capacitor banks, and ultimately more desirable goals could be achieved.

REFERENCES

[1] Abapour, S., Nojavan, S., & Abapour, M. (2018). Multi-objective short-term scheduling of active distribution networks for benefit maximization of DisCos and DG owners considering demand response programs and energy storage system. Journal of Modern Power Systems and Clean Energy, 6(1), 95-106.

[2] Das, C. K., Bass, O., Kothapalli, G., Mahmoud, T. S., & Habibi, D. (2018). Overview of energy storage systems in

distribution networks: Placement, sizing, operation, and power quality. Renewable and Sustainable Energy Reviews, 91, 1205-1230.

[3] Aman, M. M., Jasmon, G. B., Solangi, K. H., Bakar, A. H. A., & Mokhlis, H. (2013). Optimum simultaneous DG and capacitor placement on the basis of minimization of power losses. International Journal of Computer and Electrical Engineering, 5(5), 516.

[4] Mohagheghi, E., Gabash, A., Alramlawi, M., & Li, P. (2018). Real-time optimal power flow with reactive power dispatch of wind stations using a reconciliation algorithm. Renewable Energy, 126, 509-523.

[5] Bagheri, A., Bagheri, M., & Lorestani, A. (2021). Optimal reconfiguration and DG integration in distribution networks considering switching actions costs using tabu search algorithm. Journal of Ambient Intelligence and Humanized Computing, 12(7), 7837-7856.

[6] Khatib, T., & Sabri, L. (2021). Grid impact assessment of centralized and decentralized photovoltaic-based distribution generation: A case study of power distribution network with high renewable energy penetration. Mathematical Problems in Engineering, 2021.

[7] Islam, M. R., Lu, H., Hossain, M. J., & Li, L. (2019). Mitigating unbalance using distributed network reconfiguration techniques in distributed power generation grids with services for electric vehicles: A review. Journal of Cleaner Production, 239, 117932.

[8] Nguyen, T. P., Nguyen, T. A., Phan, T. V. H., & Vo, D. N. (2021). A comprehensive analysis for multi-objective distributed generations and capacitor banks placement in radial distribution networks using hybrid neural network algorithm. Knowledge-Based Systems, 231, 107387.

[9] Ganguly, S. (2020). Multi-objective distributed generation penetration planning with load model using particle swarm optimization. Decision Making: Applications in Management and Engineering, 3(1), 30-42.

[10] Zou, Y., Zhao, J., Ding, D., Miao, F., & Sobhani, B. (2021). Solving dynamic economic and emission dispatch in power system integrated electric vehicle and wind turbine using multi-objective virus colony search algorithm. Sustainable Cities and Society, 67, 102722.

[11] Vegunta, S. C., Watts, C. F. A., Djokic, S. Z., Milanović, J. V., & Higginson, M. J. (2019). Review of GB electricity distribution system's electricity security of supply, reliability and power quality in meeting UK industrial strategy requirements. IET Generation, Transmission & Distribution, 13(16), 3513-3523.

[12] Rajamand, S. (2020). Loss cost reduction and power quality improvement with applying robust optimization algorithm for optimum energy storage system placement and capacitor bank allocation. International Journal of Energy Research, 44(14), 11973-11984.

[13] Karimi-Arpanahi, S., Jooshaki, M.,

Moeini-Aghtaie, M., Abbaspour, A., & Fotuhi-Firuzabad, M. (2020). Incorporating flexibility requirements into distribution system expansion planning studies based on regulatory policies. International Journal of Electrical Power & Energy Systems, 118, 105769.

[14] Xie, S., Hu, Z., Yang, L., & Wang, J. (2020). Expansion planning of active distribution system considering multiple active network managements and the optimal load-shedding direction. International Journal of Electrical Power & Energy Systems, 115, 105451.

[15] Xie, S., Hu, Z., & Wang, J. (2020). Two-stage robust optimization for expansion planning of active distribution systems coupled with urban transportation networks. Applied Energy, 261, 114412.

[16] Mehrjerdi, H., & Hemmati, R. (2020). Wind-hydrogen storage in distribution network expansion planning considering investment deferral and uncertainty. Sustainable Energy Technologies and Assessments, 39, 100687.

[17] Gkaidatzis, P. A., Bouhouras, A. S., Doukas, D. I., Sgouras, K. I., & Labridis, D. P. (2017). Load variations impact on optimal DG placement problem concerning energy loss reduction. Electric Power Systems Research, 152, 36-47.

[18] Mousavi, M., Ranjbar, A. M., & Safdarian, A. (2017). Optimal DG placement and sizing based on MICP in radial distribution networks. In 2017 Smart Grid Conference (SGC) (pp. 1-6). IEEE.

[19] Murty, V. V., & Kumar, A. (2015). Optimal placement of DG in radial distribution systems based on new voltage stability index under load growth. International Journal of Electrical Power & Energy Systems, 69, 246-256.

[20] Kaveh, M. R., Hooshmand, R. A., & Madani, S. M. (2018). Simultaneous optimization of re-phasing, reconfiguration and DG placement in distribution networks using BF-SD algorithm. Applied Soft Computing, 62, 1044-1055.

[21] Sahu, S., Barisal, A. K., & Kaudi, A. (2017). Multi-objective optimal power flow with DG placement using TLBO and MIPSO: A comparative study. Energy Procedia, 117, 236-243.

[22] Tanwar, S. S., & Khatod, D. K. (2017). Techno-economic and environmental approach for optimal placement and sizing of renewable DGs in distribution system. Energy, 127, 52-67.

[23] Zishan,F, Akbari. E, Sheikholeslami A. Shafaghatian N. (2023). Optimization and Placement of DG Resources in the Network to Reduce Line Loading. International Journal of Industrial Electronics, Control and Optimization (IECO), 6(2) , 89-100.

[24] Sefidgar-dezfouli A. Joorabian M., Mashhour E., (2019), Microgrid optimal scheduling considering normal and emergency operation. International Journal of Industrial Electronics, Control and Optimization (IECO), 2(4), 279-288.

[25] Sanaz Ghanbari S., Abdi H., (2019), Investigating Reliability of Smart Electrical Grids Considering Self-healing in Presence of Distributed Generation Resources. International Journal of Industrial Electronics, Control and Optimization (IECO), 2(4), 343-354.

[26] Barato H., Shahsavari M., (2018), Simultaneous Optimal placement and sizing of distributed generation resources and shunt capacitors in radial distribution systems using Crow Search Algorithm. International Journal of Industrial Electronics, Control and Optimization (IECO), 1(1), 27-40.

[27] Pamuk N., Emre Uzun U.,(2024), Optimal Allocation of Distributed Generations and Capacitor Banks in Distribution Systems Using Arithmetic Optimization Algorithm. MDPI ,14 (2), 831

[28] Fettah Kh., Guia T. , salhi A ., Mouassa S., Bosisio A., Shirvani R., (2024), Optimal Allocation of Capacitor Banks and Distributed Generation: A Comparison of Recently Developed Metaheuristic Optimization Techniques on the Real Distribution Networks of ALG-AB-Hassi Sida, Algeria**.** MDPI**,** *16*(11), 4419.

[29] Mouwafi , M, El-Sehiemy, R, Abou El-Ela ,A.(2022), A two- stage method for optimal placement of distributed generation units and capacitors in distribution systems, Applied Energy , 307,118188.

[30] [Etemadi, A. H., & Fotuhi-Firuzabad, M. (2008). Distribution system reliability enhancement using optimal capacitor placement. IET Generation, Transmission & Distribution, 2(5), 621-631.

[31] Arulraj, R., & Kumarappan, N. (2019). Optimal economic-driven planning of multiple DG and capacitor in distribution network considering different compensation coefficients in feeder's failure rate evaluation. Engineering Science and Technology, an International Journal, 22(1), 67-77.

[32] Ahmidi, A., Guillaud, X., Besanger, Y., & Blanc, R. (2011). A multilevel approach for optimal participating of wind farms at reactive power balancing in transmission power system. IEEE Systems journal, 6(2), 260-269.

[33] Konopinski, R. J., Vijayan, P., & Ajjarapu, V. (2009). Extended reactive capability of DFIG wind parks for enhanced system performance. IEEE Transactions on Power Systems, 24(3), 1346-1355.

[34] Venkatesh, B., & Ranjan, R. (2003). Optimal radial distribution system reconfiguration using fuzzy adaptation of evolutionary programming. International journal of electrical power & energy systems, 25(10), 775-780.

[35] Allan, R. N., Billinton, R., Breipohl, A. M., & Grigg, C. H. (1994). Bibliography on the application of probability methods in power system reliability evaluation: 1987-1991. IEEE transactions on Power Systems, 9(1), 41-49.